Title

Spin and Lattice Dynamics, and Spin-phonon Interactions in Transition Metal Oxides

Author

Sun, Qiyang

Publication Date

2024

UNIVERSITY OF CALIFORNIA
RIVERSIDE

Spin and Lattice Dynamics, and Spin-phonon Interactions in Transition Metal Oxides

A Dissertation submitted in partial satisfaction
of the requirements for the degree of

Doctor of Philosophy

in

Mechanical Engineering

by

Qiyang Sun

June 2024

Dissertation Committee:

Prof. Chen Li, Chairperson
Prof. Richard Wilson
Prof. Jing Shi

The Dissertation of Qiyang Sun is approved:

Committee Chairperson

University of California, Riverside

Acknowledgments

I would like to express my deepest gratitude to my advisor, Prof. Chen Li, for taking me on as his Ph.D student. Prof. Li has provided me with invaluable guidance not only in my research but also in various aspects of my life. He has given me the opportunity to be involved in exciting research projects and to present my work at conferences, significantly advancing my knowledge and skills. I am truly grateful for his guidance, encouragement, and thoughtful feedback, which greatly enriched my research and scholarly pursuits.

I would like to express my sincere gratitude to Prof. Jie Ma at Shanghai Jiao Tong University for hosting me as a visiting scholar during the challenging times of the COVID-19 pandemic. Prof. Ma's warm welcome, mentorship, and support allow me to continue my research and professional development despite the disruptions caused by the global health crisis. I would also like to extend my sincere thanks to Prof. Richard Wilson, Prof. Jing Shi, Prof. Ran Cheng, Prof. Alex Greaney, and Dr. Bin Wei for their insightful discussions and suggestions, which have significantly contributed to the progress of my research. Additionally, I am thankful to my labmates, Dr. Qingan Cai, Dr. Songrui Hou, Dr. Yaokun Su, Dr. Shuonan Chen, and Yoel Lencina Wendt, for their constant support and collaboration.

I acknowledge the support of the National Science Foundation under Grant No. 1750786 and the U.S. Department of Energy, Office of Science, Office of Basic Energy Sciences under Award No. DE-SC0023874. This thesis used resources at the Spallation Neutron Source, a DOE Office of Science User Facility operated by the Oak Ridge National Laboratory. A part of this research was undertaken on the TAIPAN beamline at OPAL reactor, ANSTO.

First and foremost, I would like to express my deepest gratitude to my parents, Dr. Zhongli Wang and Mr. Gang Sun, for their unwavering support, both financially and emotionally, throughout my doctoral studies. Without their constant encouragement and belief in me, this journey would not have been possible. I am truly fortunate to have such loving and supportive parents. I would also like to thank my wife, Yue Zhou, for her unconditional love, patience, and understanding during the challenging times of my PhD program. Her presence by my side has been a source of strength and motivation, allowing me to focus on my research while knowing that I have an unswerving partner to share this experience with. Finally, I am deeply grateful to all my family and friends who have supported me throughout this journey. Their love and encouragement have been instrumental in helping me achieve this milestone.

ABSTRACT OF THE DISSERTATION

Spin and Lattice Dynamics, and Spin-phonon Interactions in Transition Metal Oxides

by

Qiyang Sun

Doctor of Philosophy, Graduate Program in Mechanical Engineering
University of California, Riverside, June 2024
Prof. Chen Li, Chairperson

The physics of mutual interaction of phonon quasiparticles with electronic spin degrees of freedom, leading to unusual transport phenomena of spin and heat, has been a subject of continuing interest for decades. Understanding the underlying mechanisms of spin-phonon interactions is pivotal for engineering spin and phonon transport and developing novel spintronic applications. By means of inelastic neutron scattering and first-principles calculations, spin-phonon dynamics in transition metal oxides are investigated. In the first part of the thesis, spin-phonon interactions and their effects on thermal transport were investigated in the exemplary collinear antiferromagnetic NiO. Anomalous scattering spectral intensity from acoustic phonons was identified, unveiling spin precession driven by phonon and strong spin-lattice correlations that renormalize the polarization of acoustic phonons. Time-domain thermoreflectance measurements of the thermal conductivity vs. temperature follow $T^{-1.5}$ in the antiferromagnetic phase. This temperature dependence cannot be explained by phonon-isotope and phonon-defect scattering or phonon softening. Instead, we attribute this to magnon-phonon scattering and spin-induced dynamic symmetry breaking.

Our results provide approaches to identify and quantify strong spin-phonon interactions, shedding light on engineering functional spintronic and spin-caloritronic materials through these interactions. In the second part of the thesis, temperature-dependent spin and phonon dynamics in Cr_2O_3 were characterized and analyzed. We unveiled the emergence of paramagnons above the T_N and at 280 K, closely below T_N. We demonstrated a significant softening of linear magnons upon heating in the antiferromagnetic state. Further analysis revealed that this softening primarily originated from four-magnon interactions, while thermal expansion played a subsidiary role. For phonon dynamics, while most phonon modes exhibit expected softening from 50 to 450 K, we observe significant stiffening in the longitudinal optical modes, which involve changing the distances between the nearest Cr^{3+} pairs. Instead of effects from thermal expansion, phonon anharmonicity, magnetostriction, or electron-phonon interactions, the anomalous stiffening can be attributed to the renormalization of electron states due to the change of spin order. Our results point to a purely static magnetoelectric-coupling origin for the observed phonon stiffening, suggest the high-tunability of phonon energies in Cr_2O_3, and provide insights into controlling lattice dynamics in novel magnetoelectric spintronics.

Contents

List of Figures **x**

1 Introduction **1**
- 1.1 Research backgrounds and motivations 1
- 1.2 Materials of interest: NiO and Cr_2O_3 6
- 1.3 Inelastic neutron scattering 8
  - 1.3.1 Lattice dynamic structure factor calculation 10
  - 1.3.2 Magnetic dynamic structure factor calculation 11
  - 1.3.3 Conventional magneto-vibrational scattering cross section 11

2 Spin-phonon interactions in NiO **13**
- 2.1 Abstract 13
- 2.2 Introduction 13
- 2.3 Methods 16
  - 2.3.1 INS measurement 16
  - 2.3.2 First-principles calculations 17
- 2.4 Spin precession driven by phonon 19
- 2.5 Phonon eigenvector renormalization 25
- 2.6 Summary 32
- 2.7 Supplementary information 33
  - 2.7.1 Supplementary figures 33
  - 2.7.2 Supplementary Notes 42

3 Effect of spin-phonon interaction on thermal transport in NiO **45**
- 3.1 Abstract 45
- 3.2 Introduction 46
- 3.3 Methods 48
  - 3.3.1 INS measurements 48
  - 3.3.2 TDTR experiments 49
  - 3.3.3 INS data folding 51
  - 3.3.4 First-principles calculations and thermal conductivity simulations 51
- 3.4 Magnon and phonon thermal conductivity 53

3.5 Effect of spin-phonon interactions on thermal conductivity 61
3.6 Summary 68
3.7 Supplementary information 69
  3.7.1 Supplementary figures 69

4 Temperature-dependent spin dynamics in Cr_2O_3 80
4.1 Abstract 80
4.2 Introduction 81
4.3 Observation of paramagnons below T_N 82
4.4 Temperature-dependent spin dynamics 87
  4.4.1 Effect of thermal expansion on magnon energies 88
  4.4.2 Magnon softening by four-magnon scattering processes 90
4.5 Summary 94
4.6 Supplementary information 95
  4.6.1 Supplementary figures 95

5 Magnetoelectric coupling induced selected phonon stiffening in Cr_2O_3 99
5.1 Abstract 99
5.2 Introduction 100
5.3 Methods 102
  5.3.1 INS measurements 102
  5.3.2 First-principles calculations 103
5.4 Stiffening of ALO modes 105
5.5 Effect of magnetoelectric coupling on lattice dynamics 111
5.6 Dynamic spin-phonon interactions 115
5.7 Summary 117
5.8 Supplementary information 118
  5.8.1 Supplementary figures 118

6 Conclusions 125

Bibliography 129

List of Figures

2.1 The measured and calculated dynamic structure factor, S(**Q**,E), of NiO at 10 K. 20
2.2 Anomalous temperature dependence of phonon INS intensity reveals strong coupling between acoustic phonon modes and spin. 22
2.3 **Q**-dependence of TA and LA phonon INS intensity at 10 K and the temperature-dependent TA and LA phonon energies at BZ boundary. 24
2.4 The measured and calculated dynamic structure factor S(Q,E) of NiO at 10 K. 33
2.5 Q-dependence of measured dynamic structure factor at BZ boundaries . . . 34
2.6 The difference of the measured INS intensity of powder sample 35
2.7 The measured and calculated dynamic structure factor S(Q,E) 36
2.8 The measured and calculated 1-D dynamic structure factor S(Q,E) 37
2.9 LSDA+U frozen phonon calculations. 38
2.10 Comparisons between measured and calculated S(Q,E) 39
2.11 The measured dynamic structure factor below TN with and without external magnetic field. 40
2.12 The measured dynamic structure factor below TN with and without external magnetic field. 41

3.1 Folded spectrums of the experimental and calculated INS dynamic structure factor S(**Q**,E). 53
3.2 Temperature dependence of magnon energy at $\mathbf{Q}_1$ = (0.5,0.5,3) and $\mathbf{Q}_2$ = (1.75,1.75,1.75). 55
3.3 Temperature-dependent experimental and calculated thermal properties of NiO. 57
3.4 Temperature-dependent phonon energy variations from INS experiments. . 60
3.5 Sketch of the phonon scattering rate in the MPS process. 63
3.6 Temperature-dependent neutron-weighted phonon density of states 69
3.7 Calculated phonon scattering rates 70
3.8 Measured INS dynamic structure factor 71
3.9 Comparison between SMRT and LBTE 72
3.10 Heat capacity of NiO. 72
3.11 Comparison of thermal conductivity. 73

3.12 Thermal conductivity of nonmagnetic materials. 74
3.13 A sketch of phonon eigenvector renormalization. 75
3.14 Comparison between calculated FM and AFM phonon properties. 76
3.15 Normalized T-dependent phonon energies. 77
3.16 Thermal conductivity of the other NiO sample. 78
3.17 The calculated phonon scattering phase space. 79

4.1 The temperature-dependent measured and calculated dynamic structure factor of Cr_2O_3. 83
4.2 Evidence of paramagnons and short-range correlation near and above T_N. . 85
4.3 Temperature-dependent magnon energy shifts from experiments and theories. 89
4.4 Magnetic Bragg Peak intensity variations. 95
4.5 Polycrystalline INS data. 97
4.6 Evidence of magnon broadening. 98

5.1 The measured and stiffening of ALO modes 106
5.2 Temperature-dependent phonon energies. 110
5.3 Electron density difference and frozen phonon potentials of different spin configurations. 112
5.4 Temperature-dependent INS spectra. 118
5.5 Experimental and calculational scattering intensities. 119
5.6 Temperature-dependent lattice constants from literature. 121
5.7 Phonon softening predicted by DFT. 122
5.8 Comparison of frozen phonon potentials and phonon energies between FM and AFM. 123

Chapter 1

Introduction

1.1 Research backgrounds and motivations

Novel spintronic and spin-caloritronic applications leverage the spin and lattice degrees of freedom to develop novel electronic and energy conversion devices. Spintronics relies on efficiently generating, manipulating, and detecting spin-polarized currents or spin waves. The spin dynamics need to be well understood and controlled to optimize device performance. Spin-caloritronic devices utilize the coupling between spin and lattice dynamics. The lattice dynamics impact the heat transport and thermal management in these devices. Tailoring the spin-phonon coupling is essential for enhancing the efficiency of spin-caloritronic energy conversion and thermal management. For example, the spin Seebeck effect devices can be used for waste heat harvesting and thermal sensors, and the underlying mechanisms involve both spin and lattice dynamics and the interaction between spin and lattice. Understanding the spin and lattice dynamics, and spin-phonon interactions is crucial for engineering functional spintronic and spin-caloritronic devices.

Lattice dynamics describes the collective vibrational modes of the atoms in a solid material. Phonons are quantized vibrations of the crystal lattice and carry energy and momentum. Lattice vibrations are governed by the interatomic forces and the crystal structure, which determine the phonon dispersion and the thermal properties of the material. Lattice anharmonicity leads to phonon-phonon scattering, the primary mechanism for thermal transport in most materials. The lattice dynamics, including phonon propagation, scattering, and energy transport, play a crucial role in various physical phenomena, such as thermal conduction, heat capacity, and phase transitions [1].

Spin dynamics describes the behavior and evolution of the spin degree of freedom of electrons (or other magnetic moments) in a material. Spin dynamics are governed by the exchange interactions, spin-orbit coupling, and magnetic anisotropy in the material. Spin dynamics involve the collective excitations of spins, known as magnons or spin waves, which can propagate through the material. Magnon energy shifting is an essential signature of strong spin fluctuations and correlations, especially near magnetic phase transitions. Paramagnons, the short-lived fluctuating magnetic moments above the ordering temperature, play a crucial role in spin relaxations and contribute to thermal capacity. Spin dynamics are critical for various spintronic and spin-caloritronic applications, as they enable the control and manipulation of spin-based phenomena for device functionalities.

Spin-phonon interaction refers to the coupling between the spin degrees of freedom of electrons and phonons in materials. Spin-phonon interaction enables spin manipulation and control by allowing for the direct manipulation of spin degrees of freedom via lattice vibrations, facilitates thermal management and spin-caloritronic effects by playing a central role in the coupling between spin and thermal transport, influences magnetic ordering and phase transitions in materials, determines spin-lattice relaxation and spin dynamics, and allows for the design and functionalization of materials with targeted spin-based properties. Qualifying, quantifying, and predicting the effect of spin-phonon interactions on spin and heat transport properties are essential for the rational development and optimization of advanced spintronic and spin-caloritronic devices.

The spin-phonon interaction can involve various coupling mechanisms, such as spin-orbit coupling, exchange interactions, and magnetoelastic effects, which can be highly complex and material-dependent. Disentangling and quantifying the contributions of different coupling mechanisms is still an active area of research. Many aspects of spin-phonon interaction remain elusive in the current research field. The following aspects are discussed in the thesis.

First, the current research on spin-phonon interaction highlights several unusual phenomena that suggest a strong coupling between spin and phonon transport. These include phonon pumping of spin current [2, 3, 4, 5, 6] and the pumping of phonons by magnetization dynamics [7, 8]. These observations have made the spin-phonon driving effect an active area of research. However, some fundamental aspects of the interaction between the lattice and spin remain unclear. For example, the selection rules governing spin-phonon interactions, the underlying mechanisms of spin relaxation through the lattice, and the quantification of the spin-phonon coupling strength are not fully understood. In this thesis, we show qualifications and quantifications of the mutual spin-phonon driving effect through a combined experimental-theoretical analysis (see Chapter 2).

Second, in magnetic insulators, phonons typically carry the majority of the heat. However, magnons can also significantly influence thermal transport in these materials. At low temperatures, the amount of heat carried by magnons can be comparable to that carried by phonons in some insulating magnetic materials [9, 10, 11, 12, 13]. The spin-phonon interactions affect the energies and mean free paths of phonons, thereby impacting the overall phonon-driven thermal transport [14, 15]. While the theory of lattice anharmonicity can provide a good understanding of thermal conductivity governed by phonon-phonon scattering, the effects of magnons and spin-phonon interactions on thermal transport are less well understood. In this thesis, our results show that the interplay between phonons, magnons, and spin-phonon coupling plays a crucial role in determining the thermal transport properties (see Chapter 3).

Third, the lattice deformation is known to result in a non-trivial change in the exchange coupling constants [16]. Thermal expansion modifies the overlaps of electron orbitals and consequently changes the exchange coupling and the anisotropy energy. However, the contribution of thermal expansion to the magnon energy renormalization is seldomly compared to that of magnon interactions, e.g., magnon-phonon and magnon-magnon scattering processes. We shed light on these through experimental characterizations and theoretical modelings (see Chapter 4).

Lastly, the existing research has shown that phonon energies can be sensitive to the dynamic spin-phonon interaction [17, 18], where the atomic vibrations modify the exchange interactions and subsequently lead to a renormalization of the phonon energy. Many previous studies have typically relied on fitting the observed phonon stiffening (increase in phonon energy) to phenomenological models [19, 20, 21, 22, 23, 24, 25, 26]. However, quantitative analyses based on first-principles calculations are still relatively scarce. Despite the experimental observations of phonon stiffening due to spin-phonon coupling, the exact underlying origin of this phenomenon remains elusive. The detailed microscopic mechanisms responsible for the observed changes in phonon energies are not yet fully understood. In this thesis, we dismiss the dynamical origin of phonon stiffening through atomistic modeling. We propose a static magnetoelectric origin that explains non-linear thermal expansion and phonon stiffening in this material (see Chapter 5).

Studying phonon and spin dynamics, and the interactions between phonons and the spin degree of freedom in magnetic materials is central to the thesis. Methods for investigations into these topics, including inelastic neutron scattering to characterize dynamic properties, first-principles calculations, and atomistic simulations to predict material properties and dynamics, are discussed in the thesis.

1.2 Materials of interest: NiO and Cr_2O_3

Mott-Hubbard antiferromagnetic (AFM) insulators are promising for ultrafast spintronics [27, 28, 29, 30], memory devices [31], and spin-caloritronic applications [32, 33]. The use of antiferromagnetic materials in spintronic devices offers several unique advantages and privileges: First, AFMs have intrinsically higher magnetic resonance frequencies compared to ferromagnets. This allows for the development of high-speed spintronic devices that can operate at terahertz (THz) frequencies, enabling ultrafast data processing and communication. Second, AFMs exhibit inherent non-volatility, meaning their magnetic state can be retained without the need for a continuous power supply and is highly advantageous for the development of energy-efficient, non-volatile memory and logic devices. Third, AFMs typically require lower switching currents or voltages compared to ferromagnetic materials, leading to reduced power consumption in spintronic devices. Fourth, AFMs are inherently insensitive to external magnetic fields due to the compensated nature of their magnetic moments. Fifth, AFMs can be engineered at the nanoscale, allowing for the development of highly miniaturized spintronic devices. Last but not least, AFMs can be seamlessly integrated into various spintronic device architectures, such as magnetic random-access memory (MRAM), spin-orbit torque devices, and spin-transfer torque devices, enabling the exploration and development of a diverse range of spintronic applications.

In this thesis, the spin and lattice dynamics in nickel (II) oxide (NiO) and Chromia (Cr_2O_3) are investigated, and new physical insights are brought to these exemplary AFM systems. NiO is the first-known collinear antiferromagnetic material with a Néel temperature (T_N) of 523 K and is a promising candidate material for spintronic and spin-caloritronic applications at ambient temperature, thanks to its high efficiency in spin transport [34, 35, 36, 37]. It has a simple face center cubic (FCC) structure in the paramagnetic (PM) phase and takes on a slight rhombohedral 0.09° distortion (deviating from 60°) in the AFM phase at 5 K [38]. While the AFM spin order together with the asymmetry of Born effective charge on Ni^{2+} ion gives rise to the splitting of two transverse optical (TO) phonons [39, 40] that are degenerate in FCC crystal symmetry, their effects on acoustic phonon remains unexplored. Moreover, the increase of thermal conductivity beyond T_N in NiO [41] hints at the existence of strong spin-phonon interactions and motivates the current work.

Cr_2O_3 is the first-known magnetoelectric material and a promising antiferromagnetic (AFM) Mott-Hubbard insulator for ultrafast spintronics [27, 28, 29, 30], memory devices [31], and spin-caloritronic applications [32, 33]. It has a corundum crystal structure below the Néel temperature (T_N = 307 K) with lattice parameters a = b = 4.95 Åand c = 13.57 Å, and a space group 167 ($R\overline{3}C$) [42]. Cr_2O_3 is also the first known magnetoelectric material [43, 44, 45, 46, 47]. Applying an electric field results in Cr^{3+} atoms on one (the other) sublattice moving closer (away) to the single O^{2-} triangle and away (closer) from the double O^{2-} triangle. This breaks the equivalence of Cr^{3+} sublattices, thereby giving rise to the emergent magnetization [48]. The magnetoelectric coupling enables the tunability of magnon polarization using an electric field in Cr_2O_3 thin films and provides a new approach toward controlling spin current [49]. Lately, the formation of magnon-polaron when the magnon and phonon dispersions cross was found in Cr_2O_3 [50], suggesting the existence of sizable spin-phonon interactions and motivates the current work.

1.3 Inelastic neutron scattering

Neutron scattering has been extensively utilized in research studies involving transport phenomena at the nanoscale level, particularly with carriers such as phonons and magnons. Shortly after James Chadwick was awarded the Nobel Prize in Physics in 1932 for his discovery of the neutron, Enrico Fermi investigated the cross-sections of slow and thermal neutrons for atomic scattering and absorption, which led to him receiving the Nobel Prize in Physics in 1938. In 1955, the first measurements of phonons using a prototype triple-axis spectrometer constructed by Bertram N. Brockhouse provided experimental confirmation of the quantum theory of solids. Over the past five decades, a vast amount of research has been conducted to gain a comprehensive understanding of the neutron scattering process, enabling scientists to leverage it as a powerful investigative tool for exploring various nanoscale phenomena.

Neutron scattering provides complementary information to other diffraction and spectroscopy techniques due to the unique physical properties of neutrons. The critical difference between neutron scattering and other experimental methods lies in the type of interaction being studied. For instance, in inelastic X-ray scattering, photons primarily interact with electrons, and the process is related to the electronic properties of the materials. In contrast, neutrons, being charge-neutral, interact with the nuclei in materials via strong nuclear forces, which have a very short range. As a result, neutrons have good penetration depth and can probe bulk material properties. Additionally, the neutron scattering cross-section is isotope-dependent, allowing for elemental contrast through isotopic substitution without significantly altering the chemical properties of the materials. Furthermore, due to their magnetic moment, neutrons can interact with magnetic moments, enabling the measurement of both magnetic structures and magnetic excitations (spin waves) in materials. This underscores neutron scattering's unparalleled ability to unravel the intricate interplay between spin and phonon excitations in magnetic materials.

Inelastic neutron scattering experiments are conducted using specialized instruments, such as triple-axis spectrometers or time-of-flight spectrometers. The scattered neutron intensity is measured as a function of energy transfer and momentum transfer. The raw experimental data undergoes various corrections and normalization procedures to account for factors such as detector efficiency, background scattering, and sample absorption. For magnon and phonon measurements, the energy transfer and momentum transfer data are plotted to obtain phonon dispersion relations, which show the relationship between phonon energy and momentum. These dispersion curves are compared with theoretical calculations based on lattice dynamics and spin dynamics models to investigate their properties. In addition to the measured dispersion, the neutron scattering data can provide information about the lifetime and linewidth of excitations, which are related to their interactions and decay mechanisms. The neutron scattering intensities can also be used to calculate the phonon and magnon density of states, which provide insights into the distribution of vibrational and magnetic excitation modes.

From another perspective, tons of scientific insights could have been buried in the scattering intensity and easily neglected without a rigorous simulation of scattering cross-sections. Conducting instrumental simulations for neutron scattering intensities improves the understanding of experimental data. As will be demonstrated in Chapter 2, by performing scattering intensity simulations, the anomalous intensity at small neutron momentum transfer is identified in nickel oxide, suggesting the presence of a mutual spin-phonon-driven effect. While detailed scattering theory can be found in the book [51], in the following, brief discussions regarding scattering intensity simulation are presented.

1.3.1 Lattice dynamic structure factor calculation

Lattice scattering intensity can be calculated based on phonon eigenvectors and eigenvalues obtained from the first-principle calculations using Phonopy [52]. The double differential lattice scattering cross section for coherent one phonon creation reads [51],

$$\begin{aligned} S_{lat}(\mathbf{Q},\omega) = \quad & \frac{\mathbf{k}'(2\pi)^3}{2\mathbf{k}v_0}\sum_s\sum_{\boldsymbol{\tau}}\frac{1}{\omega_s}|\sum_d\frac{\overline{b_d}}{\sqrt{M_d}}e^{i\mathbf{Q}\cdot\mathbf{d}-W_d}(\mathbf{Q}\cdot\mathbf{e}_{ds})|^2 \\ & \times\langle n_s+1\rangle\delta(\omega-\omega_s)\delta(\mathbf{Q}-\mathbf{q}-\boldsymbol{\tau}) \end{aligned} \tag{1.1}$$

where $\mathbf{k}$ and $\mathbf{k}^{'}$ are incident and scattered neutron wavevectors; $\mathbf{Q}=\mathbf{k}^{'}-\mathbf{k}$ denotes the momentum transfer to the sample; ω is the energy transfer to the sample; v_0 is the volume of the unit cell; s is the index of phonon branch; $\mathbf{q}$ is phonon wave vector; $\boldsymbol{\tau}$ is any reciprocal lattice vector; d refers to the position index of atom in the unit cell; $\overline{b_d}$ and M_d are coherent scattering length and mass for atom d; W_d is Debye-Waller factor, i.e., $W_d=\frac{1}{2}|\mathbf{Q}|^2\langle u_d^2(T)\rangle$, where $u_d(T)$ is the root-mean-squared displacement for atom d; n_s is Boltzmann factor; ω_s is the phonon energy for branch s at wave vector $\mathbf{q}$ and $\mathbf{e}_{ds}$ is phonon eigenvector of atom d for branch s at wave vector $\mathbf{q}$.

1.3.2 Magnetic dynamic structure factor calculation

Magnetic scattering intensity is calculated based on the Heisenberg Hamiltonian using SpinW [53]. The double differential magnetic scattering cross section for magnon reads [51],

$$S(\mathbf{Q},\omega)_{mag} = \frac{\mathbf{k}^{'}}{\mathbf{k}} r_0^2 |\frac{g\gamma}{2} F(\mathbf{Q})|^2 e^{-2W} \sum_{\alpha\beta} (\delta_{\alpha\beta} - \hat{Q}_\alpha \hat{Q}_\beta) S^{\alpha\beta}(\mathbf{Q},\omega) \tag{1.2}$$

$$S^{\alpha\beta}(\mathbf{Q},\omega) = \frac{1}{2\pi\hbar} \int dt e^{-i\omega t} \sum_{ll'} e^{i\mathbf{q}(r_l - r_{l'})} \langle \mathbf{S}_l^\alpha(0) \mathbf{S}_{l'}^\beta(t) \rangle \tag{1.3}$$

where γ=1.913, r_0 is classical electron radius; g_d, $F_d(\mathbf{Q})$ are Landé g-factor and magnetic form factor; $(\delta_{\alpha\beta} - \hat{Q}_\alpha \hat{Q}_\beta)$ is the polarization term; $S^{\alpha\beta}(\mathbf{Q},\omega)$ is the dynamic spin-spin correlation function. The scattering coefficients $k^{'}/k$ and e^{-2W} were set to unity. All dynamic structure factor calculations presented in this thesis are convoluted with instrument resolution, as implemented in SpinW.

1.3.3 Conventional magneto-vibrational scattering cross section

In the unpolarized neutron scattering cross-section, the nuclear-magnetic interference (NMI) term vanishes [51]. The total inelastic structure factor for unpolarized incident neutron reads:

$$S_{unpol} = S^L_{coh} + S^L_{inc} + S^M \tag{1.4}$$

where S^L_{coh} and S^L_{inc} are structure factors for coherent and incoherent lattice INS, and S^M is the magnetic INS structure factor. Under the assumption that the motion of ions is uncorrelated with either its spin or magnitude, magnetic scattering is comprised of four terms:

elastic magnetic scattering, inelastic magnetic scattering, magneto-vibrational scattering (MVS), and scattering which is inelastic in both the spin and the phonon systems. The term of interest here is MVS, which is elastic in the spin system and inelastic in the phonon system. The lattice + MVS scattering cross-section related to the coherent one phonon creation process could then be written as [51]:

$$\begin{aligned} S_{lat+mvs}(\mathbf{Q},\omega) = \quad & \frac{\mathbf{k}'(2\pi)^3}{2\mathbf{k}v_0}\sum_s\sum_{\boldsymbol{\tau}}\frac{1}{\omega_s}\sum_d\frac{\sigma_{tot}}{M_d}|e^{i\mathbf{Q}\cdot\mathbf{d}-W_d}(\mathbf{Q}\cdot\mathbf{e}_{ds})|^2 \\ & \times\langle n_s+1\rangle\delta(\omega-\omega_s)\delta(\mathbf{Q}-\mathbf{q}-\boldsymbol{\tau}) \end{aligned} \tag{1.5}$$

For a lattice with the spins aligned to the $\hat{z}$ direction, the σ_{tot} can be expressed as

$$\sigma_{tot} = \sigma^N_{coh} + \sigma^M = (\overline{b_d}^2 + \frac{1}{2}|\gamma r_0 g_d F_d(\mathbf{Q}) S^z_d sin(\theta)|^2) \tag{1.6}$$

where g_d, $F_d(\mathbf{Q})$ are Landé g-factor and magnetic form factor for atom d, and θ is the angle between momentum transfer $\mathbf{Q}$ and the ordered magnetic moment direction $\hat{z}$.

Chapter 2

Spin-phonon interactions in NiO

2.1 Abstract

Nickel (II) oxide is a prominent candidate of antiferromagnetic spintronic devices, largely thanks to its high Néel temperature. We present scattering signatures of mutual driving interactions through strong spin-lattice coupling and acoustic phonon eigenvector renormalization in this important material for the first time. Our results provide a new approach to identify and quantify strong spin-phonon interactions, shedding lights on engineering functional spintronic and spin-caloritronic materials through these interactions.

2.2 Introduction

Unusual spin and phonon transport phenomena, including phonon pumping of spin current [2, 3, 4, 5, 6] and pumping of phonon by magnetization dynamics [7, 8], suggest phonon propagation can greatly affect the transport of spin and vice versa, and have made spin-phonon dynamics an active field of research. However, some aspects of the interaction between lattice and spin degrees of freedom are still unclear, e.g., the selection rule for spin-phonon interactions, the underlying mechanism of spin dissipation through lattice, and the quantification of spin-phonon coupling strength. In contrast to optical phonons, acoustic phonons with large group velocities play an important role in the transport process. Resolving acoustic phonon characteristics in magnetic insulators will help understand spin-phonon interactions and engineer functional spintronic [31] and spin-caloritronic [32, 33] devices.

The most well-known spin-phonon coupling process is the modulation process, which refers to the dynamic modulation of exchange coupling between magnetic ions induced by phonons. While the spin-phonon coupling is known to result in modifications on magnon dispersions by the modulation process [54, 55], the effect on the phonon system is less well understood. For example, the spin-driven renormalization of phonon energy is only phenomenologically characterized by spin-phonon coupling coefficients in many magnetic systems [19, 24, 25]. The interaction of magnons and acoustic phonons has been extensively studied in various magnetic systems [56, 57, 58, 59, 60, 61], revealing the formation of hybrid magneto-acoustic modes, which manipulate the acoustic phonon dispersion and pass angular momentum to acoustic phonons [62]. However, existing observations are constrained to the vicinity of crossing points of magnon-phonon dispersions and do not provide the effects of such interactions on whole dispersion branches. Previous inelastic neutron scattering (INS) experiments reveal that phonon INS intensity can be modified with spin-phonon coupling and "magneto-vibrational" modes, which do not follow the wavevector ($\mathbf{Q}$) and temperature dependences of phonons, are formed [63, 64, 65, 66]. Therefore, a theoretical simulation of the phonon dynamic structure factor will shed light on identifying such modes and their scattering origin in a system with strong spin-phonon coupling.

Here, we report INS experiments and atomistic simulations that demonstrate the existence of mutual spin-phonon driving effects and the renormalization of acoustic phonon eigenvectors in bulk NiO. A strong INS intensity that follows acoustic phonon dispersions is observed at low **Q** region, where the lattice INS cross section is small, suggesting its magnetic origin. The unusual temperature dependence of such intensity is associated with the temperature dependence of magnetic order, suggestive of a strong coupling between phonon and spin. The observed intensity at low **Q** is successfully reproduced by magneto-vibrational scattering cross section based on a strong magneto-elastic correlated picture, indicating the presence of spin precession driven by phonon. More strikingly, strong INS intensity from "geometry-forbidden" transverse acoustic (TA) phonons is observed at high **Q** and shown to originate from lattice INS, indicating the renormalizations of acoustic phonon eigenvectors. The renormalization process can be related to the coupling between phonon and local magnetization and suggestive of spin-driven effects on lattice vibration.

Time-of-flight INS measurement are performed on both single crystal and polycrystalline NiO (see Methods) to measure the dynamic structure factor S(**Q**,E). The simulation of dynamic structure factor (see Methods) based on first-principles phonon calculations (see Methods) has a good agreement with measured phonon dispersions, as shown in Figure 2.1 a,b and Figure 2.4 a-d in Section 2.7.1.

2.3 Methods

2.3.1 INS measurement

Time-of-flight INS measurements were performed on single crystal NiO with the Wide Angular Range Chopper Spectrometer (ARCS) at the Spallation Neutron Source (SNS). The sample was placed on an Al holder and mounted in low-background electrical resistance vacuum furnace. Four-dimensional dynamic structure factors S($\mathbf{Q}$,E) were obtained at T = 10, 300, 540, and 640 K using incident energy of 150 meV, which covered multiple BZs and measured magnon and phonon simultaneously. Two extra measurements at 10, 300K were done with a 5T magnetic field applied along [1,1,0] direction perpendicular to the scattering plane. Data reduction was done with MANTID [67]. The data was normalized by the proton current on target and corrected for detector efficiency. Since no detectable difference can be found in binning experimental data (10, 300K) with distorted rhombohedral or FCC lattice coordinates, the slight structure distortion in the AFM phase was neglected, and the FCC crystal structure was used for data analysis. The data was sliced along high symmetry $\mathbf{Q}$-directions in reciprocal space to produce two-dimensional energy-momentum views of dispersions.

Time-of-flight INS measurements were also performed on polycrystalline NiO. The sample was loaded in an Al sample can and mounted in a low-background electrical resistance vacuum furnace. Two-dimensional dynamic structure factors S($|Q|$,E) were obtained at using incident energy of 50 meV and 150 meV. INS measurements on an empty Al can were performed at the same temperatures, and the measured intensity, as the INS background induced by the sample holder, was subtracted from the polycrystalline data.

INS data folding. Data folding was used to increase counting statistics and remove the neutron scattering form factor in the dynamic structure factors S(**Q**,E). The data folding was done by summing up the S(**Q**,E) data from over 100 BZs into an irreducible wedge in the first Brillouin zone. Offsets of the q grid were corrected by fitting the measured Bragg diffractions. This folding technique has been used in the previous study [68] and proved to be reliable.

2.3.2 First-principles calculations

The ab initio density functional theory (DFT) calculations were performed with the VASP (Vienna Ab initio Simulation Package) [69, 70] on a plane-wave basis set, using the projector augmented wave (PAW) pseudopotentials [71, 72] with local spin density approximation (LSDA) exchange-correlation functionals [73] and the Hubbard-U model [74]. U = 5 eV was chosen to obtain the best match with experimental phonon dispersion, although it underestimated the electron band gap [75]. An energy cutoff of 550 eV was used for all calculations. LSDA+U ionic relaxation was done based on a primitive cell containing 2 nickel and 2 oxygen atoms with collinear antiferromagnetic (AFM) spin order. A Gamma-centered k-point grid of 13×13×13 was used in LSDA+U ionic relaxation. The relaxed cell has a slight contraction along [1,1,1] direction. The calculated distortion angle of 0.15 Å, which deviates from 60° in the FCC primitive cell, is larger than the experiment value in Ref [38]. The relaxed rhombohedral cell (space group 166) with a lattice constant of 4.95 Å and an angle of 33.66° (from an undistorted value of 33.55°) was used in phonon dispersion calculations. The static dielectric tensor and Born effective charges were obtained to calculate non-analytical terms in phonon calculations. The second-order interatomic force constants were obtained from a 2×2×2 supercell of 32 atoms with a Monkhorst-Pack k-point grid of 6×6×6 using the density functional perturbation theory (DFPT). Phonon eigenvalues and eigenvectors were obtained by diagonalizing the dynamical matrix as implemented in the Phonopy [52]. The atomic mean squared displacements at various temperatures, and the projected phonon density of state were obtained based on the calculated phonon dispersion with a q-point sampling mesh of 30×30×30.

Phonon dispersion calculations based on quasi-harmonic approximation (QHA) were carried out to estimate phonon energy change induced by lattice thermal expansion. The collinear AFM spin order was applied to all QHA calculations. The QHA calculations were based on measured thermal expansion at 10, 300, 540, 640 K. Specifically, the LSDA+U relaxed lattice constant was used as the value at 0 K, and the lattice constants at other temperatures were determined by thermal expansion measurements from Ref.[76]. The QHA calculations followed the same configurations discussed above.

To simulate modulations of the magnetic moment and the frozen phonon potential associated with TA and LA modes under different spin configurations, LSDA+U calculations were performed with atoms in the supercell displaced according to the eigenvectors of TA and LA modes at the BZ boundary along [1,1,1]. Atomic displacements were set to be smaller than the calculated atomic root mean squared displacements at T = 500 K. Three types of spin configurations, standard collinear spin order (STD), non-collinear spin order with spin-orbit coupling (NCL), and non-spin-polarized (NSP) configurations, were considered. Under NCL spin configuration, the spin and orbit quantization axis were set to [1,1,-2] based on previous experiment results [77, 78]. For the original cell without atomic displacements, the obtained ratio between orbit and spin moment on the nickel ion was 0.1, smaller than the experiment value 0.34 [79]. Modulations of the on-site magnetic moment and frozen phonon potentials were obtained by varying displacement magnitudes under different spin configurations with a Gamma-centered k-point grid of 13×13×13.

2.4 Spin precession driven by phonon

Anomalously large INS intensity that follows acoustic phonon dispersion is observed at low **Q** and has magnetic origin. In Figure 2.1 a, pronounced spectral intensity below 45 meV is observed in the first BZ ($0 < L < 1$) along [0,0,1] in the AFM phase. Such intensity follows the dispersion of acoustic phonons, but it does not follow the $\mathbf{Q}^2$ dependence of coherent one-phonon INS process, as shown by the simulation in Figure 2.1 b. Instead, strong intensity is shown at $0 < L < 1$, with the mode weakening at $1 < L < 3$ and strengthening again at $L > 3$. Such trend is visualized by constant **Q** cuts at various equivalent reciprocal points, as presented in Figure 2.1 d,e. This is highly unusual because the phonon INS cross section is expected to be smaller at low **Q**. The anomalously strong intensity and its **Q** dependence suggest that it cannot arise solely from lattice scattering. On the other hand, the magnetic INS cross-section, which is subject to the Ni^{2+} magnetic form factor, is expected to decrease with **Q**. Therefore, the intensity of these modes at $L < 4$ can be understood as a combined contribution from magnetic and lattice scattering processes, where magnetic scattering gives diminishing intensity at higher **Q** while lattice scattering increases with **Q**. These observations also suggest that the acoustic-phonon-like intensity in the first BZ ($L < 2$) may predominantly originate from magnetic scattering.

For simplicity, such modes will still be referred to as phonon modes.

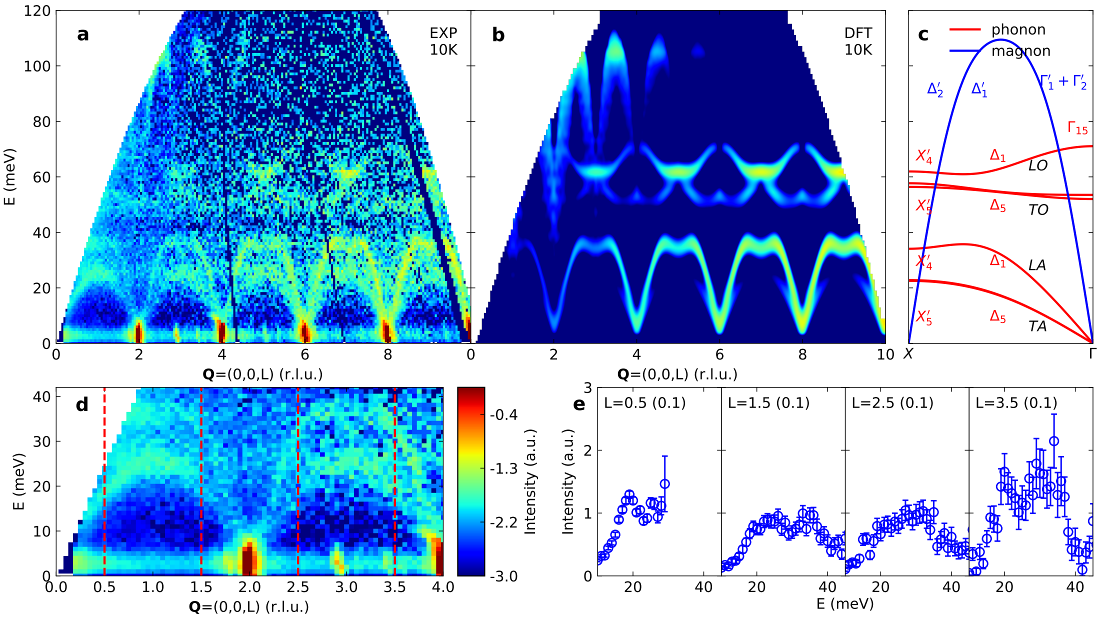

Figure 2.1: (a, d) The dynamic structure factor of NiO measured by INS along the [0,0,1] direction in the reciprocal space. The intensity is integrated over ±0.1 (r.l.u) along perpendicular axes and scaled by multiplying E. (b) Simulation of phonons and magnons with the same **Q** integration ranges and instrument resolution function. Both experimental data and theoretical calculations are plotted on a logarithmic scale. (c) Calculated phonon and magnon dispersion along $\Gamma - X$ with BSW notation [80] for phonon and magnon [81]. Phonon branches that contribute to the scattering intensity are shown. (e) Constant **Q** cuts at various equivalent **Q** points, labeled by red dashed lines in (d).

Interestingly, strong spectral intensities from acoustic phonon modes are also observed in the first BZ along [-1,1,1] and [-1,1,0], as shown in Section 2.7.1 (Figure 2.4, Figure 2.5), indicating such behavior was not limited to [0,0,1] direction. To elucidate the appearance of anomalous phonon INS intensity in small **Q** regime, volumetric views of simulated (one-phonon) and measured dynamic structure factors at 10 K are shown in Figure 2.2 a,c. The LA, TO, and LO phonon branches are well captured by the lattice dynamic structure factor calculation. At 10 K in the vicinity of (0,0,2) and (-2,2,0), the calculated intensity of LA modes is 2 orders of magnitude stronger than that in the measurement, further indicating that such intensity in low **Q** regime cannot be solely from one-phonon coherent scattering and hinting the magnetic origin of these modes.

Temperature dependence of such spectral intensity at low **Q** is also consistent with the proposed magnetic origin. At elevated temperature, both static and dynamic correlations of magnetism are weakened by increased thermal fluctuations. Indeed, the magnetic INS cross-section is directly related to the thermal average of spin correlations (see 1.3.2). Hence, it is natural to expect such anomalous intensities to weaken with increasing temperature if they have a magnetic origin. On the other hand, INS spectral intensities from phonon lattice scattering are supposed to be stronger at high temperatures because, at low **Q** regime, the Debye-Waller factor contribution is trivial (see Section 2.7.1 Figure 2.12) and the temperature-dependent lattice scattering cross section is only subject to the Bose-Einstein statistics (see 1.3.1). As shown in Figure 2.2 a,b by the cropped slice, the measured INS spectrum in lower order BZs reveals dramatic weakening at elevated temperature. Such a trend can also be observed in powder INS measurement (Figure 2.6).

This trend is clearly illustrated by integrated mode intensities extracted from Lorentzian fitting of S(E) cuts at equivalent BZ boundaries. As shown in Figure 2.2 d1,e1, both TA and LA intensities decrease with increasing temperature at **Q**=(0,0,1). Again, this is unexpected because such a descending trend cannot be explained by phonon scattering. More importantly, the spectral intensities of acoustic modes at (0,0,1) are stronger in the AF phase, and the intensities drastically decrease from 300 to 540 K through the phase transition temperature. This further suggests the anomaly is related to the magnetic order.

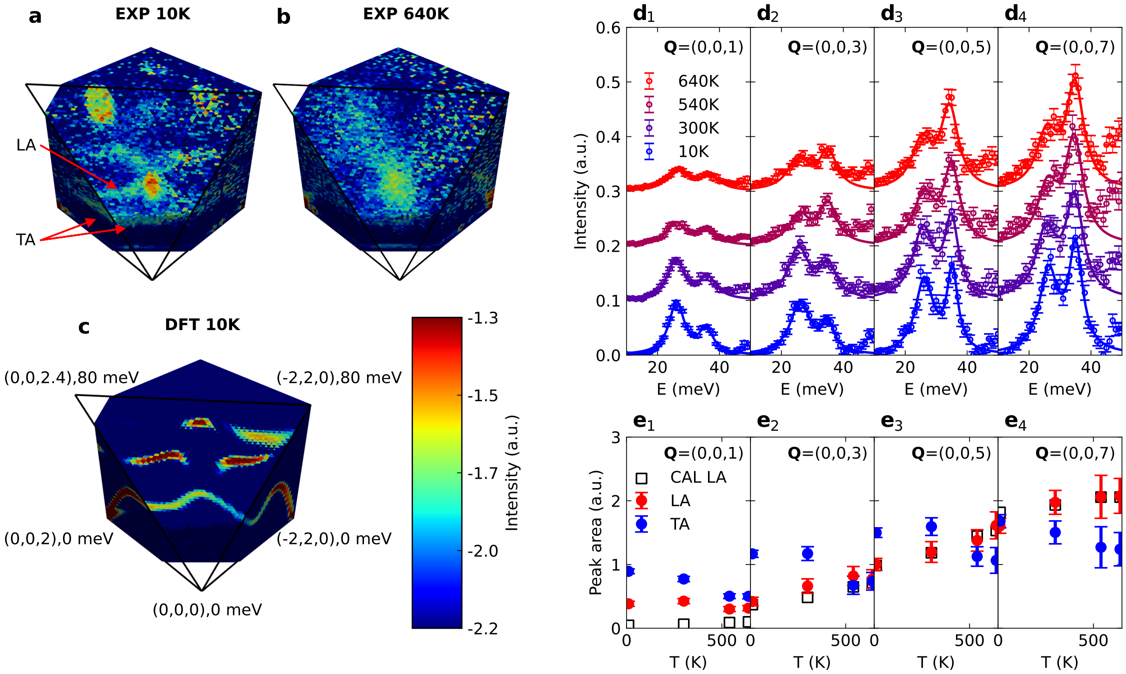

Figure 2.2: Volumetric view of the measured (a) (10 K), (b) (640 K), and calculated (c) (10 K) lattice scattering spectral intensity of coherent one phonon scattering in the (110) plane near **Q**=(0,0,0). Black lines indicate the limits of the cropped cross-section. The intensity is in arbitrary units. The spectral intensity of experiment data and calculation has been rescaled by multiplying E. (d1-d4) 1D spectral cuts at $L = 1, 3, 5, 7$ (r.l.u.) with **Q** integration ranges of ±0.2 on perpendicular directions. Symbols and colored curves represent experimental data, and Lorentzian fits at 10, 300, 540, and 640 K. (e1-e4) Temperature dependence of mode intensity from Lorentzian fits of phonon modes at equivalent BZ boundaries along [0,0,1]. There is no magnetic Bragg peak along this direction, so the spectral weights from magnons are negligible comparing to that of phonons in the experiment data below 40 meV, and the peak areas represent the intensities of TA and LA, as are denoted by blue and red dots, respectively. Black squares represent the mode intensity from simulated dynamic structure factor with the same **Q** integration configurations for LA. Error bars indicate fitting errors.

Although the appearance of phonon INS intensity at small **Q** is reminiscent of magneto-vibrational scattering (MVS), it cannot be modeled by MVS cross section. As part of magnetic INS, the MVS is elastic in the spin system, inelastic in phonon system, and proposed based on the assumption of no correlation between lattice and spin [51]. While the MVS cross-section has the same $\mathbf{Q}^2$ dependence as coherent one phonon scattering, it also contains a term related to the magnetic form factor $|F(\mathbf{Q})|^2$, giving weaker intensity at small $\mathbf{Q}$ (see 1.3.3). A detailed comparison of phonon spectral intensities between the experiment and MVS models is shown in Figure 2.3 a,b. Clearly, the calculated lattice + MVS (see 1.3.3) still fails for lower-order BZs, suggesting the MVS model cannot satisfyingly explain the observations. On the other hand, the appearance of low-$\mathbf{Q}$ anomalous intensity cannot originate from neutrons scattered by phonon orbital magnetic moments [82, 83, 84], because they are only on the order of nuclear magneton [83], and the corresponding magnetic cross-section will be 6 orders of magnitude smaller than that of typical magnetic INS by electronic dipoles. Therefore, anomalous intensity in the low-$\mathbf{Q}$ region may still originate from magnetic INS by electronic dipoles through a modified MVS process, in which lattice and spin are strongly correlated.

A magnetoelastic-correlated picture, in which the atomic displacements induced by phonon modulate the magnitude of magnetic moment (spin precession driven by phonon), explains the phonon INS intensity anomalies at small $\mathbf{Q}$. Following the methodology discussed in Ref. [64], a modified MVS (mMVS) model, which contains an extra term related to the driving coefficient, was derived (see 2.7.2). By fitting the driving coefficient ξ_{LA} to the experimental data, the obtained calculated lattice + mMVS intensity can reproduce the experimental LA intensity at lower order BZs (Figure 2.3 a). This indicates that the observed anomaly can be attributed to the effect of spin precession driven by phonons and reveals strong dynamic correlations between magnetic moment and phonon-induced lattice displacements. Meanwhile, one may expect such an effect to apply to TA phonons even though they are “forbidden” by the scattering geometry. This is because the mMVS model

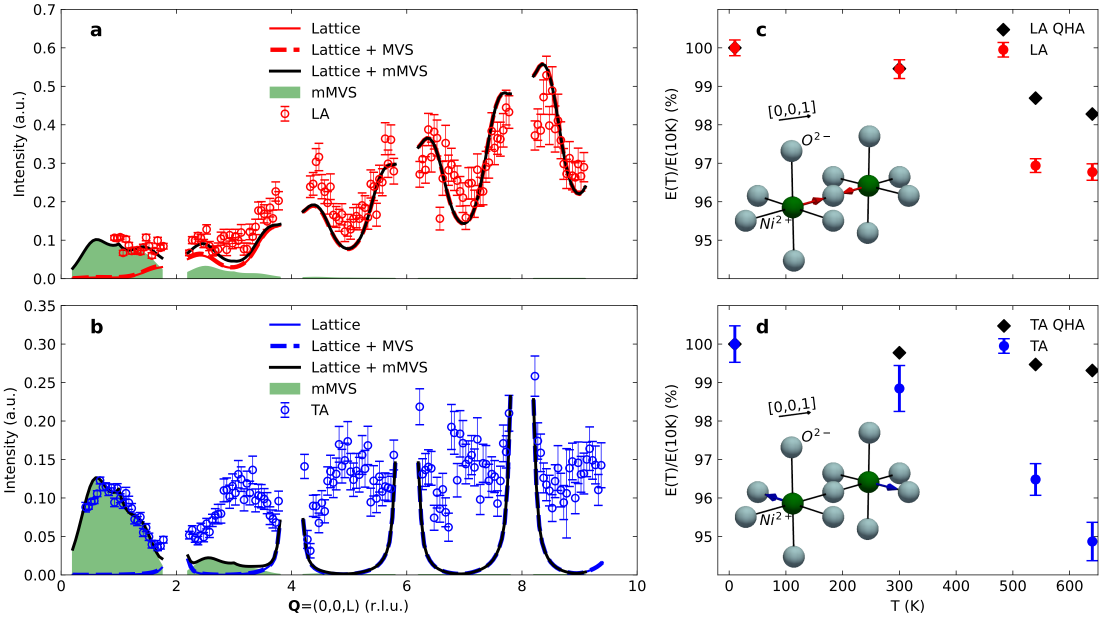

Figure 2.3: (a,b) The **Q**-dependent spectral intensity comparisons between measurement and simulated S(**Q**,E) of LA and TA modes along [0,0,1] are presented. The mode spectral intensities are obtained by subtracting a background and integrating a width of 13 meV following the calculated phonon dispersion. The red (Blue) circles represent experimental spectral intensities for LA (TA) modes. Data near Bragg points is masked. (c,d) The temperature-dependent acoustic phonon energy at the BZ boundary is plotted with quasi-harmonic approximation (QHA) calculations. Phonon energies are obtained from Gaussian fitting of the "folded" experiment data. Red and blue dots denote relative LA and TA phonon energy E(T)/E(10K) at temperature T. The error bars denote fitting errors. Atomic motion corresponding to TA and LA modes at the BZ boundary are sketched in the insets, where the red (blue) arrow indicates the phonon eigenvectors of LA (TA), and the black arrow indicates the phonon propagation direction in the real space.

is non-zero under a non-trivial driving coefficient even when $|\mathbf{Q}\cdot\mathbf{e}|^2 = 0$ [64]. Moreover, the driving coefficient of TA and LA modes can be similar in magnitude. This can be deduced from the non-collinear frozen phonon calculations (presented in Figure 2.9), which reveal the similar driving effects of TA and LA phonon-induced atomic displacements to the magnitude of magnetic moment (Section 2.7.1 Figure 2.9 a). This effect is analogous to the typical magnetoelastic coupling through dynamic modulation of exchange coupling strengths, which are of similar scales among various phonon branches by DFT calculation in NiO [85]. The driving coefficient for TA modes, ξ_{TA}, is obtained by fitting the experiment data, and its magnitude ($\xi_{TA} \approx 0.7\xi_{LA}$) reasonably agrees with the frozen phonon calculations (Section 2.7.1 Figure 2.9 a). As shown in Figure 2.3 b, the calculated lattice + mMVS intensity successfully reproduces the TA intensity at small **Q**. Henceforth, the anomalously strong TA intensity at small **Q** originates from the effects of spin precession driven by phonons like LA.

2.5 Phonon eigenvector renormalization

More strikingly, the pronounced intensity from TA mode, which is "forbidden" by the scattering geometry, is observed below 30 meV at 10 K (Figure 2.1 a, Figure 2.2 a, Figure 2.4, Figure 2.7, Figure 2.8) in a broad range of **Q**. This feature is unexpected because the momentum transfer **Q** is perpendicular to the TA phonon eigenvectors **e** ($|\mathbf{Q}\cdot\mathbf{e}|^2 = 0$) for this orientation, making the lattice INS cross section zero for these modes (see 1.3.1), except near Bragg points (Figure 2.1 b), where some intensity is expected due to finite integration width along other perpendicular **Q** directions. The observed intensity is not a result of the AFM-striction-induced lattice distortion, which has been included in our scattering simulation. One plausible explanation is the formation of magnon polarons [56, 57, 60], which emerge from magnon-phonon hybridization and possess characteristics of both magnon and phonon. Because the magnon group velocity is much larger than that of phonon, the intersections of magnon and acoustic phonon dispersion in this system only exist in a small range of **Q** in the vicinity of the lattice BZ boundaries (magnetic BZ centers). Because the "forbidden" intensity is found not only around BZ boundaries but also elsewhere in reciprocal space without magnon-phonon crossings, the intensity cannot be solely from the magnon-phonon hybridization. Moreover, ignoring the small rhombohedral lattice distortion in AFM phase, the symmetry of all phonons at long wavelength limit has an irreducible representation of Γ_{15} in Bouckaert-Smoluchowski-Wigner (BSW) notation [80]. Following the compatibility relations, the representation Γ_{15} splits into $\Delta_1 \otimes \Delta_5$ along [0,0,1] direction. In comparison, the magnon symmetry is of $\Delta_1^{'} \otimes \Delta_2^{'}$ [81], none of which are compatible with that of the phonon modes, as shown in Figure 2.1 c. As a result, magnons are not expected to hybridize with acoustic modes in NiO, and the anomalous spectral intensity from acoustic branches cannot be attributed to magnon-phonon hybridization.

Also surprising is that at higher order BZs, the temperature dependence of INS intensity from TA modes still shows a descending trend, suggesting its correlation to the magnetic order. As shown in Figure 2.2 d2-d4,e2-e4, at equivalent BZ boundaries of higher $\mathbf{Q}$ at $L > 2$,TA modes behave similarly to that in the first BZ and its intensity decreases with temperature, whereas LA intensity increases monotonically. This suggests that, at higher $\mathbf{Q}$, the weakening of “forbidden” TA modes with temperature still shows their relation to the magnetic order. On the other hand, the temperature dependence of LA intensity at $L = 3, 5, 7$ agrees well with the phonon INS simulation, showing normal phonon behavior (Figure 2.2 e2-e4).

However, at large $\mathbf{Q}$, the appearance of the “forbidden” TA intensity cannot be modeled by mMVS. This is because the mMVS cross section is subject to $|F(\mathbf{Q})|^2$, and will approach zero at large $\mathbf{Q}$ ($L > 4$) (Figure 2.3 a,b). In fact, similar “forbidden” phonon modes have been observed in $Fe_{65}Ni_{35}$ [63, 64] by INS. Despite the success of the mMVS model in explaining the "forbidden" TA modes in $Fe_{65}Ni_{35}$, the observed **Q**-dependence is completely different in NiO. While in $Fe_{65}Ni_{35}$ such mode shows a decrease in intensity at higher **Q**, our measurement presents an ascending trend, as can be seen in Figure 2.3 b. Clearly, the lattice + mMVS model still fails for TA modes at large **Q** ($L > 4$). In contrast, the experimental intensity from LA modes at $L > 4$ was successfully reproduced by the lattice scattering simulation, indicating that the LA intensity at larger **Q** is predominantly from lattice INS by phonons and is consistent with temperature-dependent analysis above. The gigantic discrepancy between experimental intensity from TA modes and lattice scattering simulation indicates that the appearance of such "forbidden" TA modes is related to the spin-phonon coupling, which is beyond the scope of mMVS model. Indeed, the effect of spin precession driven by phonon can only be reflected by magnetic neutron scattering at low **Q**, thus it cannot explain those neutron scattering signatures of phonon eigenvector renormalizations shown at high **Q**.

In the case of NiO, the "forbidden" TA intensity at $L > 4$ must predominantly result from lattice scattering instead of magnetic scattering and is suggestive of phonon eigenvector renormalization. The lattice INS origin is because magnetic INS intensity is always weaker at large **Q**, following the magnetic form factor. From the experiment data shown in Figure 2.1 a, magnon spectral intensity decreases with the increase of **Q** and vanishes at $L > 4$. It should be noted that the lattice counterpart of MVS (neutrons create or annihilate magnetic excitations via lattice scattering) can be safely ignored because the hyperfine coupling between the nuclear and electronic moments is weak [51]. The scattering intensity of this mode may have a similar scattering origin as the "forbidden" intensity observed in iron chalcogenides [66]. For iron chalcogenides, the "forbidden" intensity vanishes under the spin-flip channel by spin polarized INS measurements, indicating it primarily originates from lattice INS by phonons. Therefore, the "forbidden" TA phonon INS intensity at high **Q** must predominantly originate from lattice INS by phonons. It is worthwhile mentioning that, such intensity cannot result from the instrument resolution or **Q** integration (Section 2.7.1 Figure 2.10). If such INS intensity has a pure lattice origin, a renormalization of the phonon eigenvector is necessary to explain the observed "forbidden" modes.

Renormalization of phonon eigenvector is usually associated with the change of phonon eigen-energy, which majorly comes from lattice thermal expansion, phonon-phonon, and spin-phonon couplings in magnetic insulators. To estimate the phonon energy renormalization from spin-phonon coupling, calculations based on quasi-harmonic approximation (QHA) are carried out to evaluate energy change contributed by lattice thermal expansion in the AFM spin configuration (see Methods). Comparing experimental acoustic phonon energy at the BZ boundary with QHA calculations, the phonon energy of TA (LA) shows a 4%-5% (1%-2%) softening at 640 K (Figure 2.3 c,d). Moreover, the TA phonon energy dramatically decreases above T_N, showing a coincidence with the intensity change of the "forbidden" TA modes across T_N. This suggests both phonon energy and polarization are renormalized by the spin-phonon coupling.

The renormalization effect may originate from a direct coupling between phonons and the local magnetization of ions. Although such renormalization process is related to the symmetry breaking because phonon eigenvectors follow the symmetry of the lattice, it's worthwhile emphasizing that, the static distortion induced by the AFM-striction cannot explain the observed "forbidden" TA modes, henceforth the symmetry breaking needs to be dynamic, as was pointed out in [66]. An early work suggested that the "forbidden" INS intensity in $\mathrm{Fe}_{65}\mathrm{Ni}_{35}$ [64, 63] may result from slow local orthorhombic distortions [86], which modulate the local magnetization of magnetic ions, then indirectly modify the dynamic matrix through magnetoelastic coupling, thereby cause the renormalization of eigenvectors. The modulation on local magnetization will result in an effective dynamical symmetry breaking of the phonon system, and the corresponding "forbidden" intensity may originate from spin-driven effects on lattice vibrations. In NiO, the orbital is not fully quenched (the ratio between orbital and spin moment $L/S = 0.34$) [79, 87], so the local magnetization includes both spin and orbit parts. In addition, previous INS studies reporting observations of "forbidden" phonons suggested that perturbations to orbital states can be critical in affecting phonon characteristics [65] and the renormalization effect may be related to the coupling between phonons and electron orbit degrees of freedom [66]. In the present case, the renormalization of phonon eigenvector can result from an effective dynamical symmetry breaking, which modifies the dynamic matrix through magnetoelastic coupling, and is driven by the coupling between the phonon and the spin and orbital states on the Ni2+ ions.

Importantly, this can be reflected by the in-zone intensity of TA modes (Figure 2.3 b), which is found to be maximal at BZ boundaries (L=1,3,5,7). The TA modes at the BZ boundary are non-propagating and share the same spatial periodicity as the ground state magnetic order. Therefore, the renormalization effect is expected to be the most prominent at BZ boundaries because the coupling between phonons and sublattice magnetization is in phase. The abrupt transition from long-range spin order to short-range spin order across T_N results in the weakening of spin-phonon coupling, and thus dramatically weakens the anomalous intensity in the PM phase. However, the renormalization effect is not absent above T_N because the short-range magnetic order still exists. Similar to the observed coherent scattering intensity of magnon at 540, 640K (Figure 2.6 c3-c4), the "forbidden" intensities of TA modes exist above T_N.

Magnetic order induced anharmonicity of the phonon potential, magnon-phonon hybridization, electronic excitation-phonon couplings, and the presence of magnetic domains, are ruled out as possible origins of the phonon renormalization. Firstly, while the renormalization of eigenvectors can be closely related to the anharmonicity of the phonon potentials [88], frozen phonon calculations show that the phonon potentials of both TA and LA modes are quite harmonic regardless of their spin configuration (Section 2.7.1 Figure 2.9 b). Secondly, renormalizations of phonon eigenvectors have been found to be related to the interaction between phonons and magnetic excitations (magnons) in bulk YIG [89] and YbB_{12} [65, 90]. In YbB_{12}, the anomalous temperature-dependent phonon INS intensity was successfully explained by the symmetry compatibility between phonons and magnons, the latter of which were assumed to be of the same symmetry as crystal field excitations. However, this is not the case for NiO, in which the symmetries of phonon and magnon are not compatible, and thereby preventing hybridizations of magnon and phonon modes, as mentioned previously. Finally, even though the symmetry of TA phonons (Δ_5) and the first crystal field excitation state ($\Gamma_{25}^{'}$) are compatible, the first crystal field excitation state (around 1 eV) cannot be excited thermally in the studied temperature range, henceforth phonons are not expected to couple with the crystal field excitations. Further, the presence of magnetic domains should not affect the observed anomaly in the scattering intensity, as shown in Figure 2.11. Due to the instrument energy resolution limitation, magnon gaps and their correlation to the observed anomalies cannot be characterized.

2.6 Summary

In summary, our measurement and simulations reveal the INS signature of mutual driving effects through strong spin-phonon coupling and acoustic phonon eigenvector renormalization in NiO for the first time. In particular, the measured anomalous INS intensity that follows the dispersion of acoustic phonon first weakens, then strengthens with increasing **Q**, suggesting a combination of magnetic and lattice scattering. The intensity at low **Q** is described by the mMVS model, unveiling the presence of spin precession driven by phonon. A spin-phonon driving coefficient determined by fitting the experiment data is used to quantify spin-phonon interaction strength. Additionally, the renormalization of phonon eigenvectors indicated by "forbidden" intensity at high **Q** is related to the magnetic order by its anomalous temperature dependence. Such renormalization may result from the coupling between phonon and local magnetization via spin-driven effects on lattice vibration. Our study sheds light on the controlling of spin and lattice dynamics through spin-phonon couplings in antiferromagnetic spintronic materials. The mutual spin-phonon driving effects and the renormalization of phonon eigenvector may deserve investigation in other magnetic insulators, particularly those with strong spin-phonon coupling.

2.7 Supplementary information

2.7.1 Supplementary figures

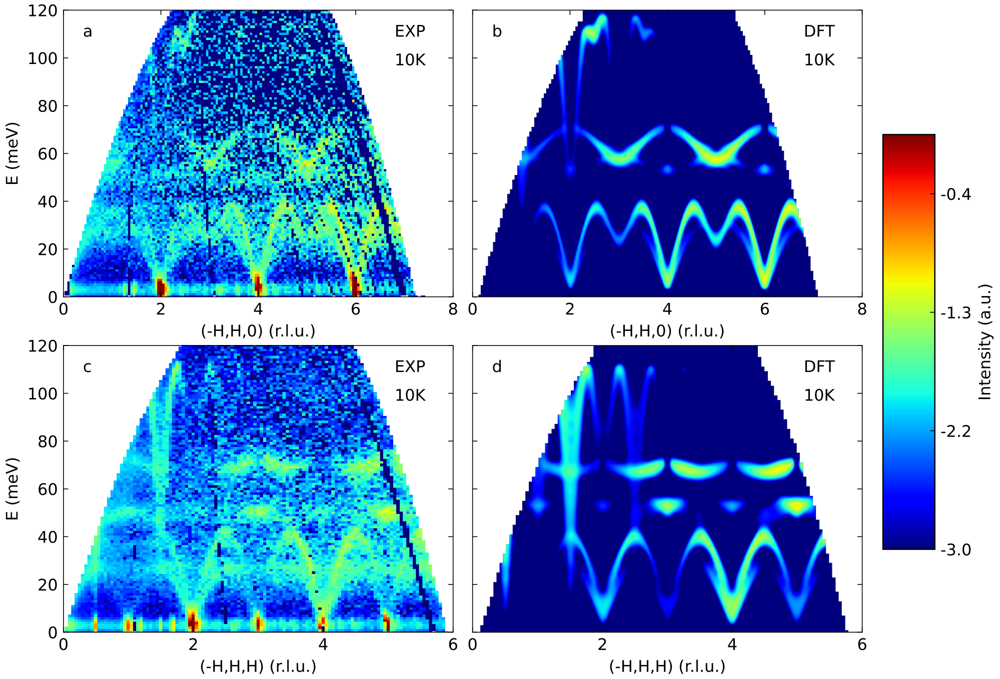

Figure 2.4: (a, c) The dynamic structure factor of NiO measured by INS on ARCS at T = 10 K along the [-1,1,1] and [-1,1,0] directions in the reciprocal space. Experimental data is integrated in a Q range of ±0.1 (r.l.u) along other perpendicular axes and renormalized by multiplying E. (b, d) Instrument resolution convoluted phonons and magnons simulation at T = 10 K with the same Q integration. Kinematic limits have been applied according to the experiment setup and the ARCS geometry. All panels are plotted on logarithmic scale.

As shown in Figure 2.4, the neutron measurement and the DFT calculation show excellent agreements in the phonon and magnon dynamic structure factor along the [-1,1,1] and [-1,1,0] directions, except for certain acoustic phonon branches as discussed in the main text. The results indicate that the observed anomalous intensities show up along all directions in the reciprocal space.

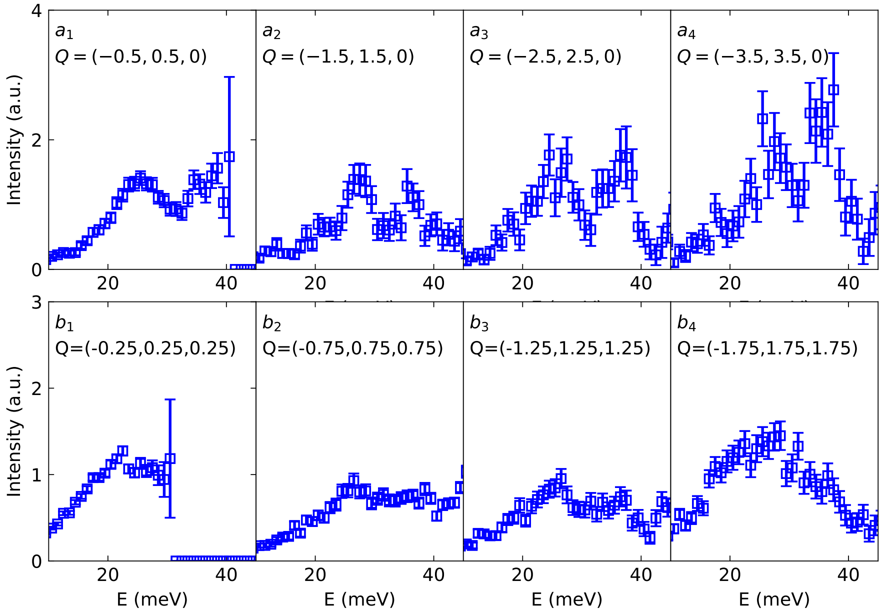

Figure 2.5: (a, b) Q-dependence of measured dynamic structure factor at BZ boundaries along [-1,1,0] and [-1,1,1]. All these constant Q cuts were taken with Q integration range of ±0.1 r.l.u. and error bars indicate statistical uncertainties.

As can be seen in Figure 2.5 a1-a4, the measured dynamic structure factors at Brillouin zone centering at (0,0,0) are anomalously large for [-1,1,0] direction, and clearly fails to follow Q^2 monotonic increasing trend for pure lattice scattering. The same conclusion can be reached for [-1,1,1] direction by comparing b1 and b4, where the measured intensity has similar magnitude and do not follow expected Q^2 relation for pure lattice scattering. Therefore, the anomalous intensity is expected to present in all three high symmetry directions.

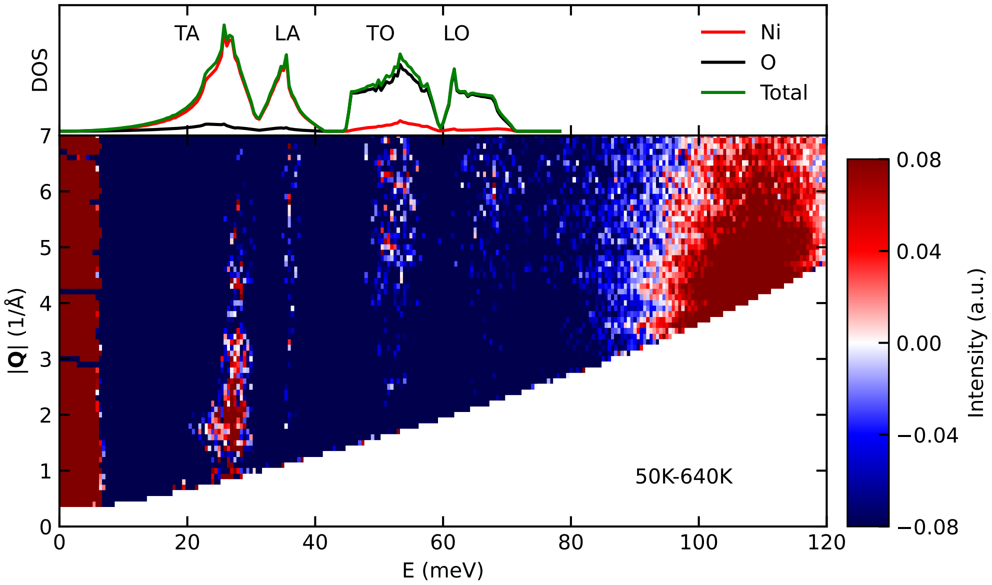

Figure 2.6: The difference of the measured INS intensity of powder sample between 50 and 640 K (lower panel). Thermal occupation factor was not removed. The intensity is in arbitrary units. The calculated phonon density of state (upper panel) indicates the energy ranges of different phonon branches. The green, red, and black curves represent calculated total, and projected density of state contributed by nickel and oxygen ions, respectively.

As can be seen in Figure 2.6, the intensity of TA phonon is stronger at 50 K for $Q < 4$ Å^{-1}. This result is unexpected for the one-phonon coherent scattering process, suggesting such an anomaly may result from magnetic scattering. The neutron scattering kinematic limit confines the coverage of scattering intensity of LA modes at low Q region ($Q < 3$ Å^{-1}). The INS intensity from LA modes is much weaker than TA modes at low Q. Hence, the temperature dependence of INS intensity from LA modes is not prominent. Nevertheless, the temperature dependence of LA at low Q region can be clearly seen by single crystal INS measurements shown in Figure 2.2 a,b,d1,e1.

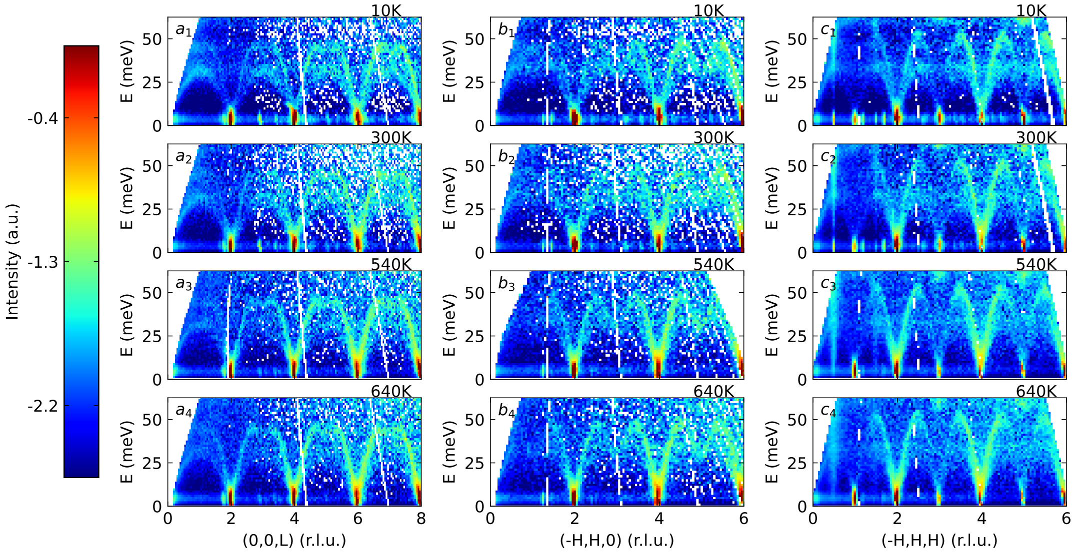

Figure 2.7: The measured and calculated dynamic structure factor S(Q,E) of NiO at 10, 300, 540 and 640 K. (a), (b), (c) show the dynamic structure factor along [0,0,1], [-1,1,0] and [-1,1,1] directions in the reciprocal space, respectively. Experimental data is integrated in a Q range of ±0.1 (r.l.u) along other perpendicular axes and renormalized by multiplying E.

In Figure 2.7, one may observe both the scattering intensity of "forbidden" TA phonon and magneto-vibrational scattering intensity at small Q weakens with temperature. The measured dynamic structure factor at 640K become analogous to normal lattice scattering patterns presented in Fig.1 b and Fig.S1 b,d.

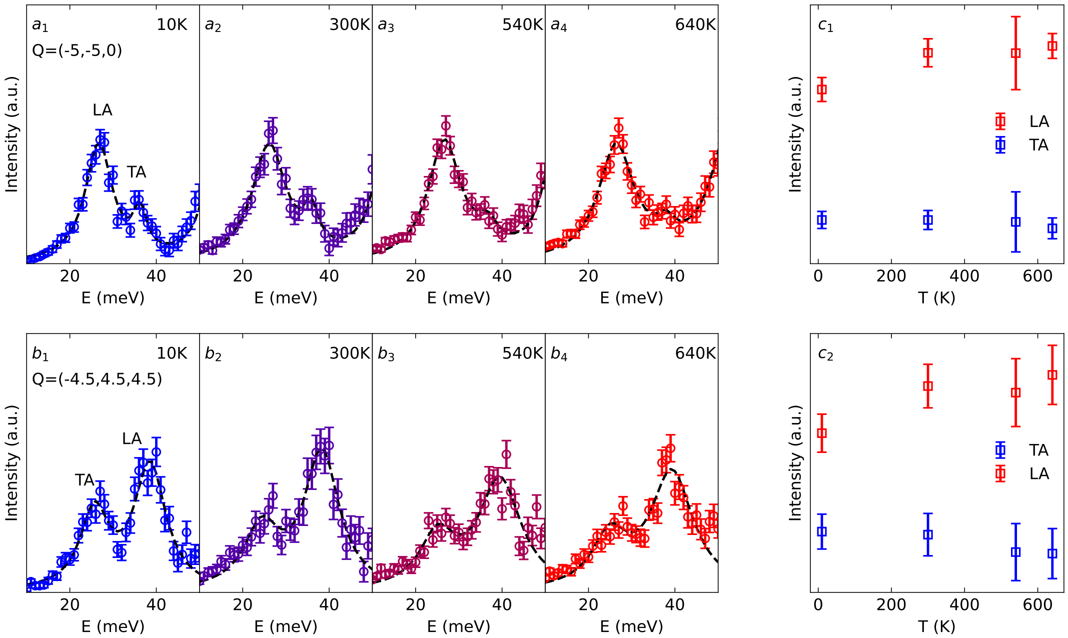

Figure 2.8: Temperature dependence of mode intensity from Lorentzian fits of phonon modes at BZ boundaries at Q=(-5,5,0) and Q=(-4.5,4.5,4.5). (a, b) Experiment data at Q=(-5,5,0) and Q=(-4.5,4.5,4.5) with a Q integration range of ±0.2 (r.l.u). (c) Temperature dependence of mode intensity from Lorentzian fits of phonon modes at equivalent BZ boundaries at Q=(-5,5,0) and Q=(-4.5,4.5,4.5). The peak areas represent the intensities of TA and LA, as denoted by blue and red dots, respectively.

As can be seen in Figure 2.8, the INS intensity of TA phonon weakens with temperature, while that of LA strengthens with temperature, showing normal lattice scattering behaviors. This indicates the effect of phonon eigenvector renormalization is not unidirectional.

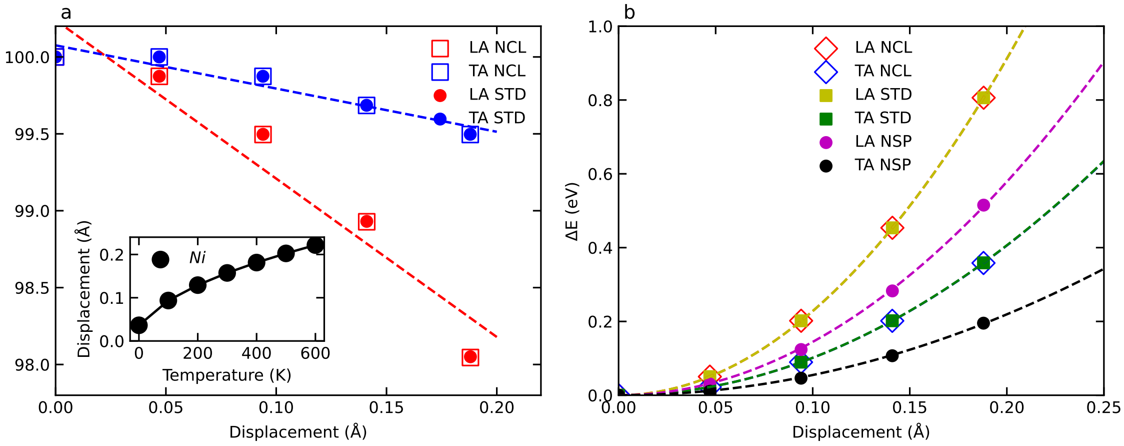

Figure 2.9: Three types of spin configurations were considered, including standard collinear spin order (STD), non-collinear spin order with spin-orbit coupling (NCL) and non-spin-polarized (NSP). (a) Change of electron magnetic moment. The inset shows temperature dependent atomic root-mean-squared displacements. (b) Frozen phonon potential at various displacements with quadratic fitting.

The modulation of magnetic moment induced by the LA mode is larger than that by the TA mode (Figure 2.9 a). The frozen phonon potential can be well fitted by quadratic functions under various spin configurations (NCL, STD, NSP), indicating the potentials are quite harmonic regardless of the underlying spin order (Figure 2.9 b).

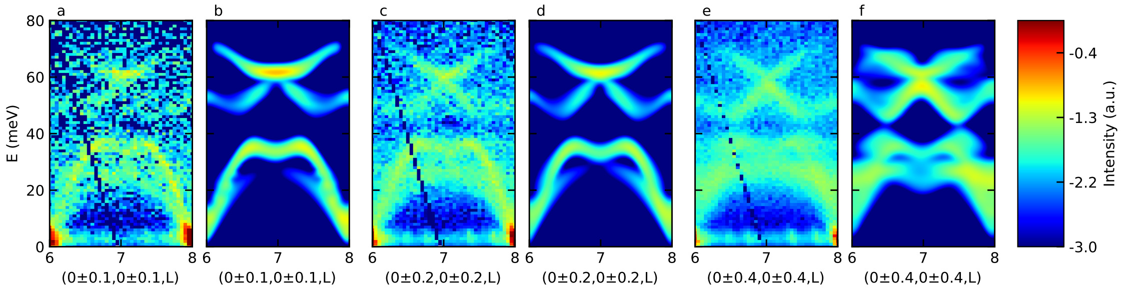

Figure 2.10: Comparisons between measured and calculated S(Q,E) with different Q integration ranges of ±0.1 (a,b), ±0.2 (c,d), ±0.4 (e,f) r.l.u. along [0,0,1] direction. The unit of Q is in reduced lattice unit. The intensity is plotted in logarithmic scale.

As shown in Figure 2.10, TA modes are not predicted by the calculated S(Q,E) under Q integration ranges of ±0.1 and ±0.2. The results confirm that the anomalous TA phonon intensity cannot result from data integration or instrument resolution, the latter of which is narrower than our integration range.

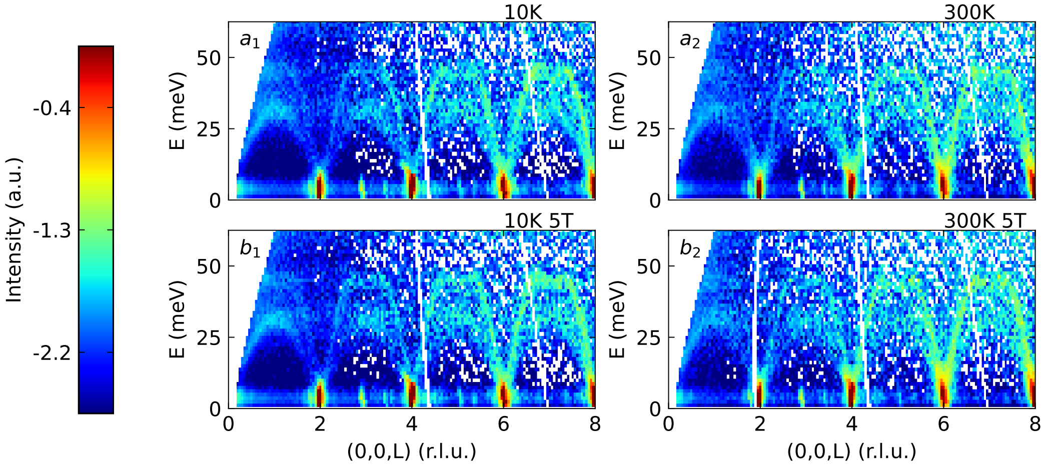

Figure 2.11: The measured dynamic structure factor below TN with and without external magnetic field. (a1, a2) shows the data at 10, 300 K without external magnetic field. (b1, b2) show the experiment data with magnetic field of 5 T applied vertically to the scattering plane. Experimental data is integrated in a Q range of ±0.1 (r.l.u) along other perpendicular axes and renormalized by multiplying E.

Experimentally, we found that the presence of magnetic domains does not affect observed anomalies in the scattering intensity. Two time-of-flight inelastic neutron scattering measurements at 10, 300K were done with a 5T magnetic field applied along [1,1,0] direction perpendicular to the scattering plane. It was indicated that the magnetic moment would be locked in the (1,1,0) plane by the field [91, 92], and only a pair of domains remain. Comparing these measurements to the data with no external magnetic field, no noticeable difference (MVS intensity or intensity of TA in higher order zones) was observed, as shown in Fig.S8. All magnetic scattering intensities were calculated based on one single domain with spin aligned along $[1, 1, \overline{2}]$ direction. Because neutron scattering only "sees" magnetic moment components that are perpendicular to the direction of neutron momentum transfer, the magnetic scattering intensity would merely be rescaled by a factor with multiple domains considered instead of changing qualitatively by an extra Q dependence. Therefore, it won't affect the ratio between ξ_{TA} and ξ_{LA}, or the results presented in Fig. 1 b; Fig. S1 b, d; Fig. 3 a,b.

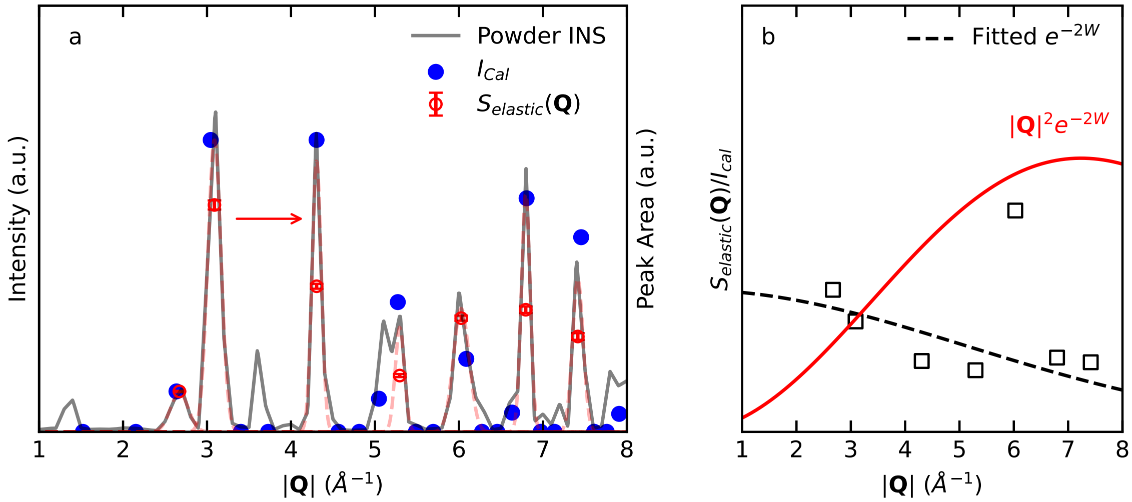

Figure 2.12: (a) Elastic profile (grey curves) from powder INS measurement at 50 K with incident neutron energy of 50meV and energy integration range of ±2 meV. Experimental intensity (red circles) is extracted from Gaussian areas of measured elastic peaks and error bars indicate fitting errors. The calculated intensity (blue dots) shows good agreement with experimental. (b) The ratios between experimental and calculated elastic peaks ($S_{elastic}(Q)/I_{Cal}$) are shown in black squares. The Debye-Waller factor fitted from $S_{elastic}(Q)/I_{Cal}$ is shown as black dashed lines. Based on that, $|Q|^2 exp(-2W)$ is evaluated and shown in red curve.

The measured elastic neutron scattering cross-section can be used to obtain the Debye-Waller factor from static and dynamic components of the atomic mean-square displacements. The coherent powder diffraction intensity (excluding the Debye-Waller factor),

$$I_{Cal} = \sum_{d,G} |\overline{b_d} exp(i\boldsymbol{\tau}\cdot\mathbf{d})|^2 \delta(\mathbf{Q}-\boldsymbol{\tau})$$

determined by neutron scattering length ($\overline{b_d}$), phase factor $exp(i\boldsymbol{\tau}\cdot\mathbf{d})$ and momentum conservation $\delta(\mathbf{Q}-\boldsymbol{\tau})$ is evaluated based on undistorted face-center-cubic structure in paramagnetic phase. By assuming nickel and oxygen atom have the same magnitude of static and dynamic displacements, the Debye-Waller factor can be extracted by comparing elastic INS intensity $S_{elastic}(Q)$with I_{Cal},

$$exp(-2W) = S_{elastic}(Q)/I_{Cal}$$

The atomic displacement $\sqrt{\langle u^2 \rangle}$ obtained from powder INS measurements at 50 K is of 0.14 Å, which includes contributions from both static and dynamic parts. As can be clearly seen in panel e, the $|Q|^2 exp(-2W)$ increases as a whole for $|Q| < 6$ Å^{-1}, which covers the first two Brillouin Zones at [0,0,L] direction ($L < 4$ r.l.u.). Therefore, it's safe to rule out the possibility that the decrease and increase of INS intensity (Fig.1 e) at small Q originates from the Debye-Waller factor.

2.7.2 Supplementary Notes

Modified magneto-vibrational scattering (mMVS) cross section

For acoustic branches corresponding to the motion of Ni^{2+} ions, a good approximation can be made by neglecting the intensity contributions from the vibration of O^{2-} ions because the eigenvectors $\mathbf{e}_{ds}$ associated with these phonon modes are small (see Figure 2.6). The lattice + MVS scattering cross section for acoustic branches can be written as:

$$S_{lat+mvs}(\mathbf{Q}, \omega) = (1 + \frac{\sigma^M}{\sigma^N_{coh}})S_{lat} \tag{2.1}$$

If the lattice and spin were strongly correlated, the conventional MVS model is not applicable to the system. We use a modified MVS (mMVS) model [64] based on the assumption that the local magnetic moment was driven by atomic displacements from phonons,

$$S_i = S_{i0}(1 - x\sum_j \epsilon_{ij}[\delta R_i - \delta R_j]) \tag{2.2}$$

where S_i (S_{i0}) is the perturbed (unperturbed) magnetic moment associate to magnetic ion i; ϵ_{ij} is the strain between next-nearest-neighbor (NNN) atoms, which dominates the AFM super-exchange coupling between Ni^{2+} ions; x is a constant describing linear dependency of phonon driving effect to the magnitude of magnetic moment of ion i; δR_i is the phonon induced displacement of magnetic ion i from its equilibrium position. Following Ref.[64], the modified MVS cross section from coherent one phonon creation process could be expressed as:

$$\begin{aligned} S_{mmvs}(\mathbf{Q},\omega) = \quad & \frac{k^{'}(2\pi)^3}{2\mathbf{k}v_0}\sum_s\sum_{\boldsymbol{\tau}}\frac{1}{\omega_s}\sum_d\frac{\sigma^M}{M_d}|e^{i\mathbf{Q}\cdot\mathbf{d}-W_d}((\mathbf{Q}+\xi q\hat{\mathbf{r}})\cdot\mathbf{e}_{ds})|^2 \\ & \times\langle n_s+1\rangle\delta(\omega-\omega_s)\delta(\mathbf{Q}-\mathbf{q}-\boldsymbol{\tau}) \end{aligned} \tag{2.3}$$

where $\hat{\mathbf{r}}$ are unit vectors connecting NNN magnetic ions, $\xi = x/|\mathbf{r}|^2$ is the normalized driving coefficient; $W_d^{'} = \frac{1}{2}|\mathbf{Q}+\xi q\hat{\mathbf{r}}|^2\langle u_d^2(T)\rangle$ is the modified Debye-Waller factor of mMVS for the atom d; q is the value of the in-zone wave vector and is maximal at BZ boundaries. From the equation above, the Q-dependence of scattering intensity depends on three factors:

1. The magnetic form factor, which makes the mMVS cross section decays at larger momentum transfer. This should not be omitted because mMVS is still a magnetic scattering process.

2. The modified Debye-Waller factor, $W_d^{'}$, which is small at low temperature due to the small mean square displacements u_d.

3. The modified term, $(\mathbf{Q}+\xi q\hat{\mathbf{r}})\cdot\mathbf{e}_{ds}$, which leads to spectral intensity even if the momen-

tum transfer from neutrons to the lattice is perpendicular with phonon eigenvectors under non-trivial driving coefficient ξ.

In our simulation of the mMVS cross section, the spectral intensity from O^{2-} ions was ignored as discussed in the previous section (see Figure 2.6), and the Debye-Waller factor W_d' was assumed to be unchanged. All phonon eigenvectors in the following calculation are from the phonon calculations discussed in Methods. For LA modes, the modified MVS can be expressed as:

$$S_{mmvs}^{LA}(\mathbf{Q},\omega) = \frac{\sigma^M|(\mathbf{Q}+\xi_{LA}q\hat{\mathbf{r}})\cdot\mathbf{e}_{LA})|^2}{(\sigma_{coh}^N|\mathbf{Q}\cdot\mathbf{e}_{LA}|^2)} S_{lat}(\mathbf{Q},\omega) \tag{2.4}$$

Because the eigenvectors of TA modes are perpendicular to $\mathbf{Q}$ $(\mathbf{Q}\cdot\mathbf{e}_{LA}|^2)=0)$, Eq.2.4 cannot be used to evaluate the mMVS cross section for TA modes. Instead, the mMVS cross section for TA modes can be estimated as following,

$$S_{mmvs}^{TA}(\mathbf{Q},\omega) = \frac{2|(\xi_{LA}q\hat{\mathbf{r}})\cdot\mathbf{e}_{TA})|^2\omega_{LA,Q}}{|\mathbf{Q}+\xi_{LA}q\hat{\mathbf{r}})\cdot\mathbf{e}_{TA}|^2\omega_{TA,Q}} S_{mmvs}^{LA}(\mathbf{Q},\omega) \tag{2.5}$$

The driving coefficients $\xi_{LA} = 9$, $\xi_{TA} = 6.5$ was obtained by fitting the experimental data at Q=(0,0,1).

Chapter 3

Effect of spin-phonon interaction on thermal transport in NiO

3.1 Abstract

Nickel (II) oxide is a prominent candidate for spintronic and spin-caloritronic applications operating at room temperature. Although there are extensive studies on nickel oxide, the roles of magnon- and spin-phonon interactions on thermal transport are not well understood. In the present work, the relationship between spin-phonon interactions and thermal transport is investigated by performing inelastic neutron scattering, time-domain thermoreflectance thermal conductivity measurements, and atomistic thermal transport calculations. Inelastic neutron scattering measurements of the magnon lifetime imply that magnon thermal conductivity is trivial, and so heat is conducted only by phonons. Time-domain thermoreflectance measurements of the thermal conductivity vs. temperature follow

$T^{-1.5}$ in the antiferromagnetic phase. This temperature dependence cannot be explained by phonon-isotope and phonon-defect scattering or phonon softening. Instead, we attribute this to magnon-phonon scattering and spin-induced dynamic symmetry breaking. The spin-phonon interactions are saturated in the paramagnetic phase and lead to a weaker temperature dependence of $T^{-1.0}$ at 550-700 K. These results reveal the importance of spin-phonon interactions on lattice thermal transport, shedding light on the engineering of functional antiferromagnetic spintronic and spin-caloritronic materials through these interactions.

3.2 Introduction

Thermal transports in magnetic insulators are predominantly governed by lattice dynamics, spin dynamics, and mutual interactions between them. Phonons and magnons are quantized energy carriers that correspond to lattice and spin degrees of freedom. Their contributions to thermal conductivity vary in different systems. Phonons usually carry most of the heat in magnetic insulators. Magnons also affect the thermal transport of magnetic insulators through two mechanisms. First, in some insulators, the amount of heat carried by magnons is comparable to that of phonons at low temperatures [9, 10, 11, 12, 13]. Second, spin-phonon interactions affect phonon energies and mean free paths, thus the transport of phonons [14, 15]. Although thermal conductivity governed by phonon-phonon scattering can be understood by the theory of lattice anharmonicity [1], the effects of magnon and spin-phonon interactions are less well understood [93]. The majority of existing work focused on tuning thermal conductivity by an external magnetic field at low temperatures, where thermal transport is not dominated by phonons. It was observed that with increasing external magnetic field, the magnon-phonon interaction is weakened and the thermal conductivity is enhanced in ferromagnetic, ferrimagnetic, and magnetic frustrated materials [94, 95, 96]. These observations suggest that spin-phonon interactions suppress thermal transport. However, the thermal conductivity in antiferromagnetic materials has a much weaker field dependence [14], thus the effects from spin-phonon interactions are not extensively explored. There is great potential in engineering thermal transport through such interactions.

While there are extensive experimental and theoretical studies on thermal transport in single crystal NiO [97, 98, 41, 99, 100, 101], there are no conclusive experimental thermal conductivity data or atomistic models for magnon and phonon transport in the context of spin-phonon interactions. The most cited experimental work was done by F. B. Lewis et al [41]. Although the thermal conductivity was reported to increase with temperature in the paramagnetic (PM) phase, suggesting strong spin-phonon interactions, the measurement was not conclusive because of possible radiational heat loss [41]. The increase of thermal conductivity in the PM phase is contrary to later measurements done by M. Massot et al [100], who measured the thermal conductivity only in the vicinity of T_N. Previous Raman experiments only focused on the temperature dependence of the phonon energy at the zone center [24]. The lack of accurate measurements of thermal conductivity in a wide temperature range, characterizations of temperature-dependent magnon and phonon dynamics off zone centers, and atomistic models for magnon and phonon transport hindered further investigations of thermal transports in this important material. The present work sheds light on these points.

In the current work, we performed inelastic neutron scattering (INS) experiments to characterize magnon and phonon dynamics, time-domain thermoreflectance (TDTR) measurements to measure temperature-dependent thermal conductivity, and atomistic simulations to investigate phonon and magnon transport in the context of spin-phonon interactions in NiO. INS measurements of magnon lifetimes indicate that the magnon thermal conductivity is negligible at all temperatures. TDTR measurements reveal that the thermal conductivity of NiO decreases from 55 W/(m·K) at 200 K to 13 W/(m·K) at 500 K. First principles calculations show that this temperature dependence is greater than can be explained with phonon-phonon and phonon-defect scattering (from 53 to 20 W/(m·K) in the same temperature range). INS measurements of temperature-induced phonon energy softening cannot also explain the observed temperature dependence of thermal conductivity. We attribute the difference to spin-phonon interactions.

3.3 Methods

3.3.1 INS measurements

Time-of-flight INS measurements were performed on single-crystal NiO with the Wide Angular-Range Chopper Spectrometer (ARCS) at the Spallation Neutron Source at Oak Ridge National Laboratory. Incident energy of 150 meV was used for measurements under 10, 300, 540 and 640 K. The sample was loaded with Al foil and placed in a low-background electrical resistance vacuum furnace with (H,H,0) plane horizontal. Data reduction was performed with MANTID [67]. The INS data were normalized by the proton current on the target and corrected for detector efficiency using a vanadium scan. Since no detectable difference can be found in binning experimental data (10, 300 K) with distorted rhombohedral or FCC lattice coordinates, the slight structure distortion of the AFM phase was neglected, and the FCC crystal structure was used for data analysis. The data was sliced along high symmetry **Q**-directions in reciprocal space to produce two-dimensional energy-momentum views of dispersions.

Time-of-flight INS measurements were also performed on polycrystalline NiO. The sample was loaded in an Al sample can and mounted in a low-background electrical resistance vacuum furnace. The two-dimensional dynamic structure factors S($|Q|$,E) were obtained at T = 50, 280, 450, 540 and 640 K using an incident energy of 50 and 150 meV. INS measurements on an empty Al can were performed at the same temperatures and neutron incident energy. The measured intensity, as the INS background induced by the sample holder, was subtracted from the polycrystalline data. The data have been corrected by multiphonon scattering and thermal occupation using GETDOS [102].

Triple-axis INS measurements were performed on the same single-crystal with triple-axis spectrometer TAIPAN at OPAL reactor at ANSTO to map phonon dispersion near the zone center. Constant **Q** scans near zone centers at (1,1,1), (0,2,2) and (0,0,2), and constant energy scans at 10, 15, and 20 meV along [1,1,1] were performed at 300, 450, and 650 K.

3.3.2 TDTR experiments

We performed TDTR measurements on two single-crystal NiO samples between 125 and 675 K. TDTR is a well-established pump probe technique for the characterization of thermal properties [103]. Details of our TDTR setup can be found in Ref. [104]. We mounted the samples in a heater stage (Microptik MHCS600) for temperatures above 300 K and in a cryostat (Janis ST-300MS) below 300 K. We pumped the sample chamber down to ~10-5 torr during the experiments. We coated the NiO samples with a ~80 nm Al film. The Al film serves as both a heat absorber and a thermometer. In TDTR measurements, a train of 783-nm-wavelength laser pulses emitted from a mode-locked Ti:sapphire oscillator is split into a pump beam and a probe beam. The pump beam heats the sample at a modulation frequency of 10.7 MHz. The probe beam monitors the temperature decay at the sample surface via temperature-induced changes in the reflectance of the Al film. The reflected probe beam from the Al film is collected by a silicon photodiode detector. A lock-in amplifier reads the microvolt change in voltage output by the detector due to changes in reflected probe beam intensity. The amplifier outputs the in-phase signal V_{in} and the out-of-phase signal V_{out} at the 10.7 MHz modulation frequency. The size of the laser spot in $1/e^2$ radius $w_0 = 6.5\ \mu$m and is measured by the beam offset method [11]. We controlled the steady-state temperature rise in NiO to be less than 5 K considering its phase transition at 523 K. The steady-state temperature increase in the TDTR measurements is [103]

$$\Delta T_s = \frac{P_i(1-R)}{2\sqrt{\pi}w_0\kappa}$$

where P_i is the incident laser power, R is the optical reflectivity of Al, and κ is the thermal conductivity of NiO. We make sure $\Delta T_s < 5$ K by controlling the incident pump and probe power. We analyzed the collected ratio, $-V_{in}/V_{out}$, using a heat diffusion model to extract the thermal conductivity of NiO [103]. The model needs several input parameters, such as laser spot size, modulation frequency, and thermal properties of each layer. We measured the thickness of the Al film by picosecond acoustics [105]. We used experimental results from literature for the heat capacity of Al and NiO at different temperatures [41, 106, 107]. For the heat capacity of NiO above 630 K, there is no experimental data. Thus, we extrapolate the experimental results in Ref. [41].

3.3.3 INS data folding

Data folding was used to increase the counting statistics and remove the neutron scattering form factor in the dynamic structure factors S($\mathbf{Q}$,E). Data folding was done by summing up the S($\mathbf{Q}$,E) data from over 100 BZs into an irreducible wedge in the first Brillouin zone. The offsets of the q grids were corrected by fitting the measured Bragg diffractions. This folding technique has been used in a previous study [68] and has been demonstrated to be reliable.

3.3.4 First-principles calculations and thermal conductivity simulations

The ab initio density functional theory calculations regarding obtaining second order interatomic force constants, phonon eigenvalues, and eigenvectors can be found in Section 2.3.2. Third-order force constants were also calculated using a 2×2×2 supercell, corresponding to 32 atoms with 6×6×6 reciprocal mesh sampling and an energy cutoff of 550 meV. The third-order force constants were calculated from 226 inequivalent displacements based on the supercell mentioned forehead without a pair-cutoff distance. Second-order and third-order force constants are symmetrized to minimize drift force constants as implemented in Phono3py [108]. Phonon lifetimes were obtained from the imaginary part of the calculated phonon self-energy, which was evaluated by the lowest-order many-body perturbation theory as implemented in Phono3py. The lattice thermal conductivity accounting for 3-phonon scattering was calculated by solving the linearized phonon Boltzmann equation (LBTE) using the single mode relaxation-time method [108, 109] with Phono3py. The lattice thermal conductivity using the direct solution of LBTE is also calculated with Phono3py. Phonon lifetimes and lattice thermal conductivity converged in 20×20×20 q mesh. The isotope scattering due to the mass variance of isotope distributions was performed as implemented in Phono3py. The thermal conductivity by phonon-phonon, phonon-isotope and phonon-defect scattering is estimated by $\kappa_{pd} = \frac{1}{N}\sum_{qj} c_{qj} v_{qj}^2 \tau_{p,qj}$. According to Matthiessen's rule, the single-mode phonon relaxation time at specific q and branch j follows $\frac{1}{\tau_{p,qj}} = \frac{1}{\tau_{pp,qj}} + \frac{1}{\tau_{pi,qj}} + \frac{1}{\tau_{pd,qj}}$, where $\tau_{pp,qj}$, $\tau_{pi,qj}$ and $\tau_{pd,qj}$ stand for relaxation time by phonon-phonon, phonon-isotope and phonon-defect scattering. It is assumed that the relaxation time of the scattering of phonon defects due to point defects is assumed to follow $\tau_{pd,qj}^{-1}(\omega_{qj}) = A(\frac{\omega_{qj}}{\omega_{max}})^4$, where A is a scaling factor; $\omega_q j$ and $\omega_m ax$ are the phonon energy and cutoff phonon energy at point q for branch j, respectively. A is obtained by fitting the measured thermal conductivity of NiO (I) below 200 K.

The phonon properties with collinear ferromagnetic (FM) spin order were calculated based on the same relaxed cell mentioned forehead. The second order force constants, the static dielectric tensor and Born effective charges were obtained in the same procedures. By changing from AFM to FM spin order, the phonon maximum energy increase 5.6%. The phonon Grüneisen parameters with FM and AFM spin order were calculated from three separate phonon band structure calculations with lattice constants of -0.3%, 0% and +0.3%, as implemented in Phonopy.

3.4 Magnon and phonon thermal conductivity

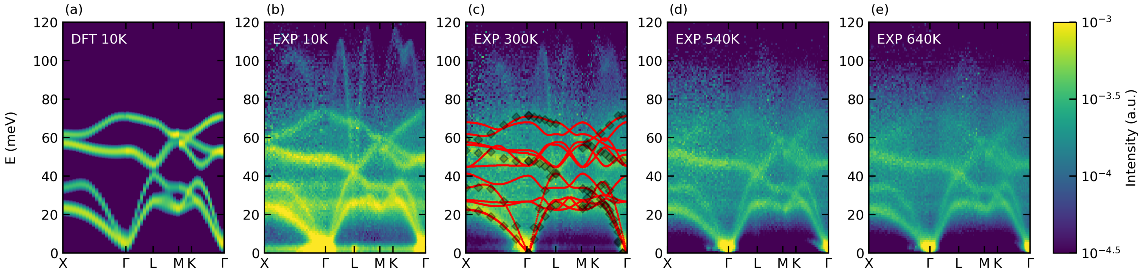

Figure 3.1: Data folding was done by integrating the intensity of INS over 100 slices, which have data coverages greater than 70%, into an irreducible wedge. (a) Folded coherent one-phonon scattering S(**Q**,E) simulation at 10 K with the same **Q** integration configurations as experimental ones. (b-e) Experimental S(**Q**,E) at 10, 300, 540, and 640 K. Previous phonon dispersion measurements at 300 K [110] and calculated phonon dispersions are plotted in (c) as black dots and red curves, respectively. Thermal occupation corrections were applied to both the calculated and experimental data.

Time-of-flight INS measurements were performed on single-crystal NiO with ARCS spectrometer at the Spallation Neutron Source (see 3.3.1). The four-dimensional dynamic structure factors, S(**Q**,E), were mapped at 10, 300, 540 and 640 K and folded into an irreducible wedge in one Brillouin zone (see 3.3.3). In Figure 3.1, the folded S(**Q**,E) shows phonon and magnon dispersions. The spectral intensity of the magnons is weaker than that of the phonons. In Figure 3.1 c, the measured phonon dispersion shown in the folded S(**Q**,E) is consistent with previous measurements at 300 K [110]. The S(**Q**,E) calculated by the coherent lattice INS (see Section 1.3.1) at 10 K shows excellent agreement with the measurements (Figure 3.1 a, b). Our DFT calculation predicts the longitudinal optic mode energy of 71.2 meV at the zone center (Γ), matching well with our measurement and previous Raman measurement at 300 K [24]. Two branches of nondispersive INS intensities around 23 and 35 meV overlay with low-lying optical modes (Figure 3.1 b, c). These intensities arise from incoherent INS by nickel atoms, which have a non-trivial incoherent scattering cross section of 5.2 barn. This is confirmed by the coherent one-phonon scattering dynamic structure factor simulation in Figure 3.1 a. Similar incoherent scattering intensities have been observed in CoO [111]. Our INS measurements provide detailed characterizations of magnon and phonon properties and shed light on the calculation of thermal conductivity, as discussed below.

The total thermal conductivity (κ) in NiO can be represented as $\kappa = \kappa_m + \kappa_p$, where κ_m and κ_p are the thermal conductivity by magnon and phonon transports, respectively. In this system, the intrinsic linewidth broadenings of magnons were much smaller than the magnon energy. Magnons would be well defined and can be treated as propagating quasiparticles. In this case, the kinetic theory of thermal transport can be applied to calculate the magnon thermal conductivity [112]. The thermal conductivity along [1,0,0] can be calculated with

$$\kappa_m = \sum_q c_q v_q^2 \tau_q$$

, where c_q,v_q,τ_q are the mode volumetric specific heat (energy density per unit volume), projected group velocity along the [1,0,0] direction, and the mode relaxation time of magnon at the grid point q, respectively. The c_q takes the form,

$$c_q = \frac{1}{NV} \frac{\partial}{\partial T} \frac{\omega_q}{exp(\omega_q)/(k_B T)) - 1}, \tag{3.1}$$

where N is the total grid points in the reciprocal space; V is the volume of the unit cell; ω_q is magnon frequency at grid point q, k_B is the Boltzmann constant, and T is the temperature. ω_q,c_q,v_q are obtained from the calculated magnon dispersions (see Section 1.3.2), which show great agreement with experimental data at 10K (Section 3.7 Figure 3.8).

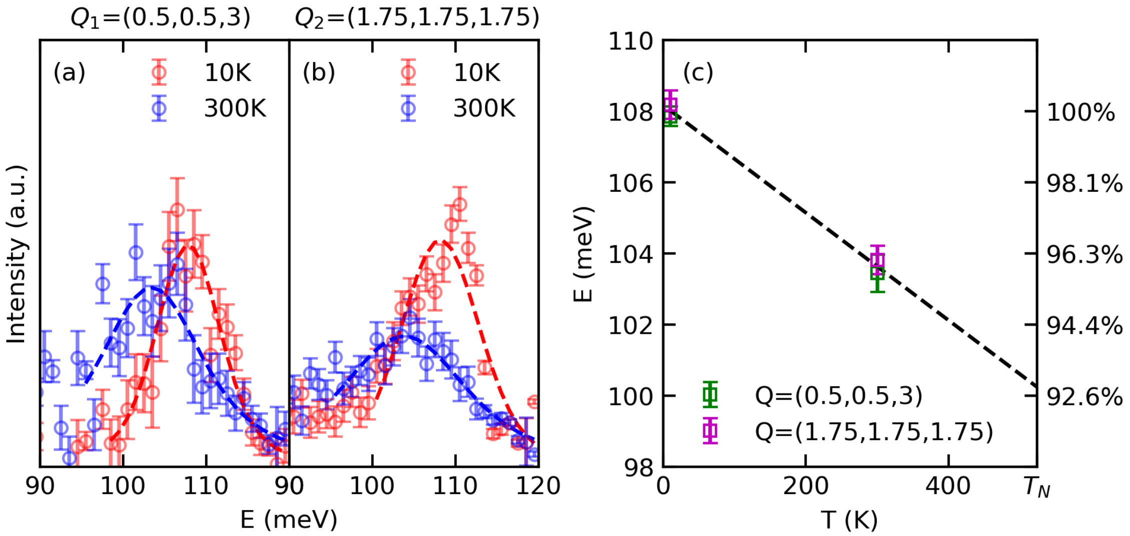

Figure 3.2: (a, b) Fitting of the experimental data at $\mathbf{Q}_1$ and $\mathbf{Q}_2$ with a $\mathbf{Q}$ integration range of ±0.1 (r.l.u.). Red and blue circles are experimental data at 10, 300 K, respectively. Error bars denote statistical errors. Dashed lines are the fitting results (see text) by the Voigt function with fixed Gaussian linewidth obtained from the fitting magnon S($\mathbf{Q}$,E) calculation at 10, 300 K, respectively. The energy of the magnon decreases with temperature. The green and purple squares are centers of the fitted peaks at $\mathbf{Q}_1$ and $\mathbf{Q}_2$, and the error bars denote the fitting errors.

The magnon thermal conductivity was obtained based on the lifetime calculated from the magnon linewidth. The magnon linewidths were obtained by fitting experimental and calculated one-dimensional dynamic structure factor S(E) slices at $\mathbf{Q}_1$ = (0.5,0.5,3) and $\mathbf{Q}_2$ = (1.75,1.75,1.75). The experimental data were fitted with a convolution of the resolution and the intrinsic lifetime broadening. The resolution function is Gaussian and its linewidth, γ_G, includes contributions from the instrument energy and $\mathbf{Q}$ resolution. A Lorentzian function with its half-width half-maximum (HWHM), γ_L, is used for the intrinsic lifetime broadening. For 10 K, the fitted γ_L are 1.9±0.5 and 1.7±0.8 meV and magnon intrinsic lifetime, $\tau = 1/(2\gamma_L)$, are 172 and 191 fs at $\mathbf{Q}_1$ and $\mathbf{Q}_2$, respectively. The results on magnon lifetimes are comparable with previous measurements on ultrathin ferromagnetic films using spin-polarized high-resolution electron energy loss spectroscopy [113]. As suggested by Wu et al. [112], magnon lifetimes τ_q scale with ω_q^{-1} in the presence of spin-phonon interactions, hence, τ_q can be approximated by $\tau_q = \tau_0\omega_0/\omega_q$, in which τ_0 and ω_0 are the magnon energy and lifetime at the top of the dispersion. Although NiO has two magnon eigenmodes, they degenerate in a wide span of reciprocal space. The degeneracy is broken only in the vicinity of the magnetic zone center with magnon gaps of 4.3 and 0.6 meV [114, 115]. In this case, the effect of the magnon gap on magnon transport was not considered. With specific heat, the projected group velocity and the lifetime obtained at 10 K, κ_m along [1,0,0] direction is calculated to be 0.2, 0.9, 1.3 W/(m·K) at 100, 300, 500 K respectively, as shown in Figure 3.3 d. It should be noted that the temperature dependences of magnon τ_q and ω_q are not considered in the present calculation and the κ_m should be treated as an upper limit because both τ_q and ω_q decrease with temperature (Figure 3.2). At 300 K, the magnon intrinsic linewidth γ_L are 5.7±1.0 and 6.4±0.8 meV and magnon intrinsic lifetime, are 58 and 51 fs at $\mathbf{Q}_1$ and $\mathbf{Q}_2$, respectively (Figure 3.2 a,b). At 300 K, the calculated magnon thermal conductivity is around 0.3 W/(m·K) and much less than the upper limit. We estimated the κ_m between 10 to 500 K using temperature-dependent magnon energies and lifetimes, which are obtained from linear fittings of the experimental data at 10 and 300 K. As shown in Figure 3.3 d, the estimated κ_m first increases from 10 to 320 K and gradually decrease above 320 K.

The phonon thermal conductivity (κ_p) was calculated based on 3-phonon scattering with the single mode relaxation time (SMRT) approximation [108, 109] (see 3.3.4). Phonon-isotope scattering due to the mass variance of isotope distributions was also considered (see

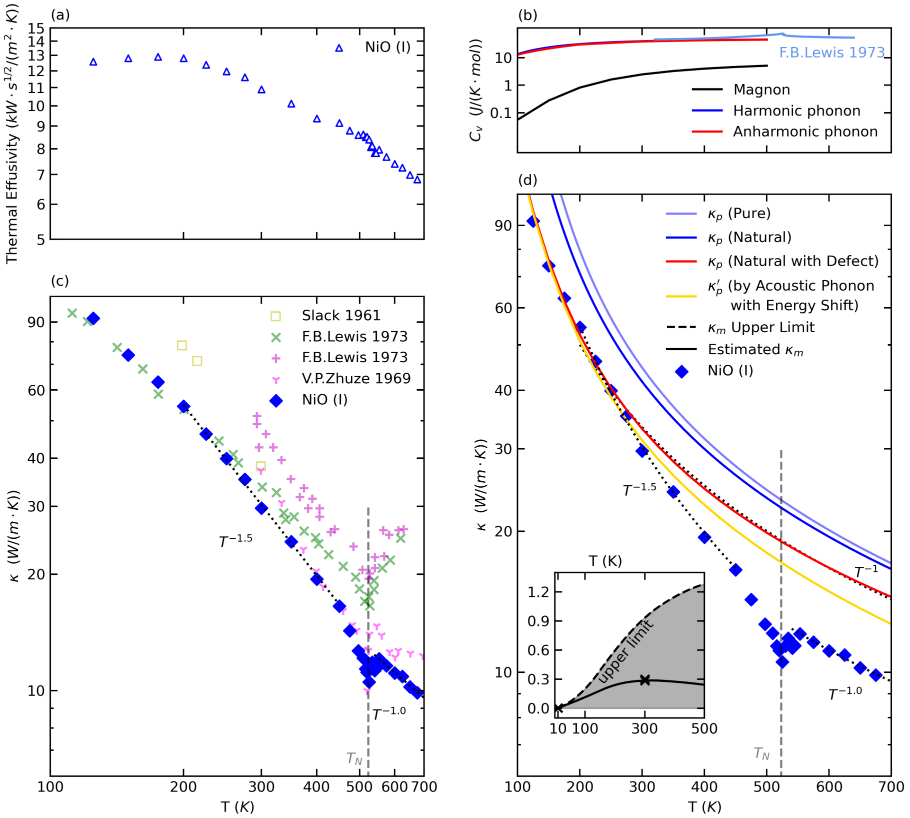

Figure 3.3: (a)Thermal effusivity of NiO (I) measured by TDTR. (b) Calculated specific heat of magnons and phonons. The blue (red) curves indicate the calculated specific heat of the harmonic (anharmonic) phonons. The calculated specific heat agrees well with previously measured data around 400 K [41]. The black curve indicates the calculated specific heat of the magnon. (c,d) Experimental and calculated thermal conductivity. The blue squares show the thermal conductivity results for NiO (I) from the TDTR measurement. In panel (c), purple, green, yellow and pink labels show previous thermal conductivity measurements on NiO [41, 98, 97]. In panel (d), the blue (light blue) lines indicate the calculated thermal conductivity of phonon κ_p based on 3-phonon scattering of natural (pure) compounds. The κ_p of natural compounds includes the effect from phonon-isotope scattering due to the mass variance of natural isotope distributions. The red line shows the estimation of the κ_p by phonon-phonon, phonon-isotope, and phonon-defect scattering. The yellow line shows the κ_p' by acoustic phonon modes considering phonon energy shifts with temperature (see text). Data points are fitted using different temperature dependences as indicated by the black dotted lines (see text).In the inset, the black dashed curve indicates the calculated upper limit of κ_m and the solid curve shows the estimated κ_m from temperature-dependent magnon energies and lifetimes. The black cross labels indicate κ_m calculated at 10 K and 300 K.

3.3.4). Phonon-defect scattering due to point defects was estimated by fitting TDTR data below 200 K (see 3.3.4). The calculated κ_p using SMRT approximation and direct solution of the linearized Boltzmann transport equation (LBTE) shows little difference (Section 3.7 Figure 3.9). It should be mentioned that other calculational results of κ_p obtained by direct solution of LBTE with considered phonon-phonon and phonon-isotope scattering have recently been reported [101]. The reported κ_p is around 25 W/(m·K) at 300 K, much lower than our calculation (natural with defect, 31 W/(m·K)) and our measurement (30 W/(m·K)) shown in Figure 3.3 d. The difference may arise from the different exchange-correlation functionals that were used (LDA in the present work, hybrid-PBE in ref.[101]) and the difference in phonon dispersion (~7% in the total energy scale). Above 200 K, the calculated κ_p follows T^{-1} (Figure 3.3 d), which is typical for nonmetallic materials in high-temperature regimes due to phonon-phonon interactions [116].

The calculated thermal conductivity of the phonons is much larger than that of the magnons in the AFM phase (Figure 3.3 d). The total thermal conductivity is determined mainly by phonon transport. The huge difference between κ_p and κ_m mainly results from the difference in cumulative specific heat, where the specific heat of magnons is about two orders of magnitude lower than that of phonons at 100 K (Figure 3.3 b). Near and above T_N, magnon lifetimes are expected to decrease drastically due to the loss of long-range spin order, and the thermal conductivity by magnon is also expected to be small.

TDTR measurements were performed on two NiO single crystals labelled NiO (I) and NiO (II) (see 3.3.4). TDTR is a transient method for thermal transport measurements whose experimental signals are proportional to thermal effusivity ($\sqrt{\kappa C}$). The NiO (I) crystal has a flat thermal effusivity below 200 K. Above 200 K, the thermal effusivity decreases with temperature, and a small dip was observed at 523 K. Using values from the literature for the heat capacity versus temperature of NiO [41, 107] (see Section 3.7 Figure 3.10), we estimate the thermal conductivity versus temperature from the experimentally measured thermal effusivities.

The thermal conductivity of NiO (I) in the AFM phase depends strongly on temperature between 200-450 K. κ decreases from 55 W/(m·K) at 200 K to 17 W/(m·K) at 450 K. This corresponds to a temperature dependence of $T^{-1.5}$ (Figure 3.3c). At temperatures greater than 550 K in the PM phase, the temperature dependence of the thermal conductivity is weaker. The thermal conductivity decreases with $T^{-1.0}$ above 550 K. The NiO (II) crystal has lower thermal conductivity with weaker temperature dependence (Section 3.7 Figure 3.16) because of a higher defect concentration than NiO (I). κ of NiO (I) in Figure 3.3c is more representative of the intrinsic transport properties of NiO.

We now compare our results to prior measurements of κ of NiO. Our data show a trend similar to previous results measured by Zhuze et al. using a pulse technique [98], see Figure 3.3c. Both measurements show an overall decreasing thermal conductivity with temperature, with a dip around T_N.

Although our data are consistent with the results by Lewis et al. [41] below 200 K, the measured thermal conductivity is lower and shows a stronger temperature dependence from 200 to 450 K (Figure 3.3 c). The discrepancy may be related to radiation heat loss in the steady-state longitudinal method used [41, 117], see Section 3.7 Figure 3.11. Errors in thermal conductivity caused by heat loss from radiation are known to follow the T^3

dependence [117]. We calculate the difference between our measurements and the steady-state results ($\Delta\kappa$) at 200-500 K and find it to be proportional to T^3 (see Figure 3.11).

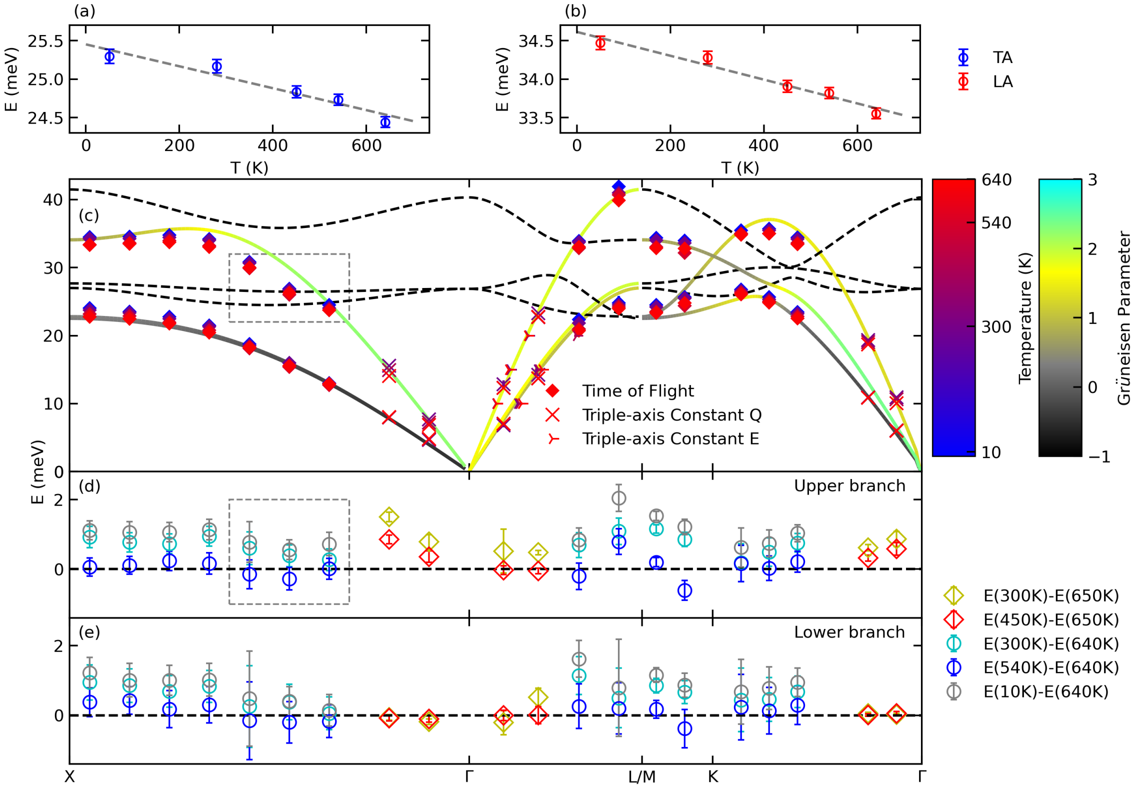

Figure 3.4: (a,b) Phonon energies from the phonon density of state INS measurements with incident neutron energy of 50 meV at 50, 280, 450, 540 and 640 K. The experimental data have been corrected for by multiphonon scattering and thermal occupation. There are two distinct peaks around 25 and 34 meV, corresponding to the (a) TA and (b) LA phonon modes. (c) Measured and calculated phonon energies for LA and TA modes along high-symmetry directions. Squares and cross markers represent phonon energies from the time-of-flight (measured at 10, 300, 540 and 640 K) and triple-axis (measured at 300, 450 and 650 K) INS measurements, and the corresponding colors denote temperatures. The q-resolved mode Grüneisen parameters are calculated based on quasi-harmonic approximation and indicated by the colored lines. Zone-folding modes that cannot be seen from INS experiments are shown in dashed lines. The fitting errors are smaller than the marker size. (d,e) Difference of the phonon energy from low to high temperature of the upper branch (d) and the lower branch (e). All phonon energies were extracted from Lorentzian fittings of the measured data, and error bars indicate fitting errors. The incoherent INS scattering signals around 26 meV can cause slightly biased phonon energies, as denoted by grey boxes.

In Figure 3.3d, we compare our experimental and theoretical predictions for the thermal conductivity. While the calculated κ_p (natural with defect) and the measured κ are in good agreement for $T < 300$ K, they diverge for T above room temperature. Experimental κ decreases more rapidly with T than theory can explain. The discrepancy between theory and experiment increases as T increases from 300 to $T_N = 523$ K. Then, at temperatures above T_N, the difference between experimental and theoretical κ stays roughly constant at ~ 25 %. In addition to disagreeing with our theoretical predictions for NiO, we note that a $T^{-1.5}$ dependence for κ is different from other non-magnetic insulators with face-center-cubic crystal structure and similar phonon properties. For example, crystals such as MgO have a κ that is proportional to T^{-1} (Section 3.7 Figure 3.12) in the same temperature range. Therefore, we conclude that simple phonon-phonon scattering, or phonon-isotope and phonon-defect scattering, cannot explain the observed temperature dependence of NiO at 200-450 K (Figure 3.3 d). We conclude that there is another temperature-dependent scattering term that affects transport at temperatures above 300 K.

3.5 Effect of spin-phonon interactions on thermal conductivity

In kinetic theory, temperature effects on phonon transport can be reflected in two parts: changes in phonon energy and lifetime. On one hand, the shift in phonon energy affects thermal capacity (unless the temperature is well above Debye temperature) and group velocity, and thus thermal conductivity. From our INS measurements on polycrystalline NiO, the measured phonon energies monotonically decrease with temperature for both TA and LA modes (Figure 3.4 a, b), and for optical modes (Section 3.7 Figure 3.6). The softening of acoustic phonon energy with temperature was also observed via INS measurements on single crystal NiO, as shown in Figure 3.4 c-e. With the assumption of isotropic and uniform softening of the phonon modes on heating, the phonon energy for the specific phonon mode i at temperature T can be approximated by $\omega_i(T) = \omega_{0i}(1 - \eta T)$, where ω_{0i} is the phonon energy at 0 K, η is a positive coefficient representing softening of the acoustic phonon mode i and is obtained from linear fittings $\omega = \omega_0(1 - \eta T)$ on the measured phonon energy (Figure 3.4 a, b). The obtained η_{TA} and η_{LA} are 5.6×10^{-5} and 4.5×10^{-5} K^{-1} meV^{-1}, respectively. In the long wavelength limit, the group velocity for mode i can be expressed as $v_i = v_{0i}(1 - \eta T)$. The effect of phonon softening on mode thermal conductivity can be shown by $\zeta_i(T) = \dfrac{c_i(T)v_i(T)^2}{(c_i(T)v_i(T)^2)|_{\eta=0}}$, where $c_i(T) = \dfrac{1}{V}\dfrac{\partial}{\partial T}\dfrac{\omega_{0i}(1-\eta T)}{exp((\omega_{0i}(1-\eta T))/(k_bT)) - 1}$.

Assuming that the phonon lifetime does not change, the thermal conductivity with temperature-induced acoustic phonon energy shifts was calculated as

$$\kappa_p^{'}(T) = \sum_{qj} \kappa_{p,qj}\zeta_{qj}(\eta, T) = \sum_{qj} c_{p,qj}v_{p,qj}^2|_{\eta=0}\zeta_{qj}(\eta, T)\tau_{p,qj},$$

in which $\kappa_{p,qj}$ represents the calculated mode thermal conductivity for specific phonon mode at point q for branch j, and the softening coefficient η was set to be η_{TA} for all acoustic phonon modes. The group velocities (Figure 3.1) and lifetimes (Section 3.7 Figure 3.7 a) of the acoustic phonon modes are much larger than those of the optical modes, and the acoustic phonon modes contribute more than 90% of the total thermal conductivity at 300-700 K (Section 3.7 Figure 3.7 b). In this case, the $\kappa_p^{'}$ can be approximated by considering only acoustic phonons. As shown in Figure 3.3 d, the $\kappa_p^{'}$ is not sufficient to explain the $T^{-1.5}$

temperature dependence, although it was underestimated due to the exclusion of optical phonon transport, the approximation of group velocities in long wavelength limit, and the use of a large softening coefficient η for all acoustic modes.

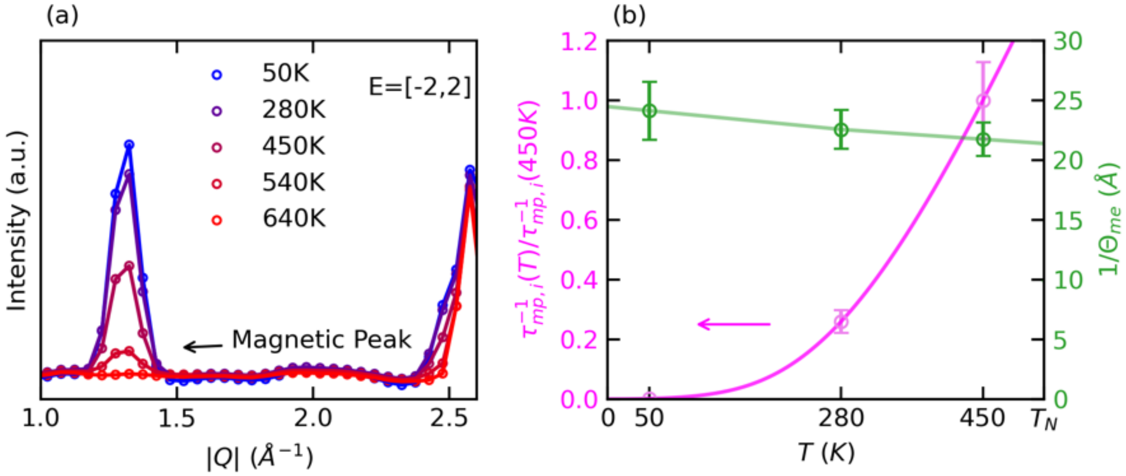

Figure 3.5: (a) One-dimensional $S(|\mathbf{Q}|)$ by INS powder measurements at 50-640 K with energy integration of ±2 meV. The elastic magnetic peaks show around 1.3 Å^{-1} and their intensities weaken on heating significantly, whereas elastic lattice peaks retain the same. (b) The inverse of the HWHM of the magnetic elastic Bragg peak $1/\theta_{me}(T)$ (green labels) and normalized phonon scattering rate $\tau_i^{-1}(T)/\tau_i^{-1}$ (450 K) (purple labels). Colored lines are guides for the eye.

In our discussion above, we have ruled out phonon-isotope scattering, phonon-defect scattering, and phonon softening as explanations for the κ vs. T dependence of NiO. We now turn our attention to spin-phonon interactions that affect phonon lifetime. In magnetic insulators, magnon-phonon scattering (MPS) can also affect phonon transport. According to Matthiessen's rules, the scattering rate for the specific phonon mode i is expressed by $\tau_(p,i)^{-1} = \tau_{pp,i}^{-1} + \tau_{pi,i}^{-1} + \tau_{pd,i}^{-1} + \tau_{mp,i}^{-1}$, where $\tau_{pp,i}^{-1}$, $\tau_{pi,i}^{-1}$, $\tau_{pd,i}^{-1}$, $\tau_{mp,i}^{-1}$ correspond to the scattering rate for phonon-phonon, phonon-isotope, phonon-defect, and magnon-phonon scattering processes.

Spin-phonon interactions will have two effects on thermal transport. First, MPS ($\tau_{mp,i}^{-1}$) will reduce the phonon lifetimes. The single-mode acoustic phonon scattering rate can be expressed by $\tau_{mp,i}^{-1} = nv_s\sigma$, where n is the density of scatters, v_s is the speed of sound, σ is the scattering cross section [118]. In this simplified MPS model, the temperature dependences of σ can be described by$\sigma = \pi(\lambda(T)/2)^2$ [96], where $\lambda(T)$ is the magnetic correlation length. We approximate the correlation length from the HWHM ($\theta_{me}(T)$) of magnetic elastic Bragg peak (Figure 3.5 a) by $\lambda(T) = 1/\theta_{me}(T)$. Noting that the $\lambda(T)$ is underestimated due to the instrument resolution in $\mathbf{Q}$ ($\sim$ 0.04 Å). For phonons scattered by magnon mode, $n = \int n_{BE}(E,T)g_m(E)dE$, where n_{BE} is Bose-Einstein statistics, E is magnon energy and g_m(E) is the magnon density of state. With a fixed v_s, the normalized single phonon scattering rates $\tau_{mp,i}^{-1}(T)/\tau_{mp,i}^{-1}$ (450 K) first increases slowly then dramatically from 0 to 450 K (Figure 3.5 b). The $\tau_{mp,i}^{-1}$ at 200 K is only 8% of the $\tau_{mp,i}^{-1}$ at 450 K, hence, the magnon-phonon scattering is less important at low temperatures. At 200-450 K, $\tau_{mp,i}^{-1}$ is of a higher order of T and can lead to the observed strong temperature dependence of thermal conductivity. We note that fully quantifying the contribution of MPS to thermal conductivity requires a detailed calculation of the phase space and interaction strength (collision matrix) of MPS. This is beyond the scope of the current work.

Second, spin-phonon interactions break the symmetry of the phonon system dynamically, leading to increases in the phonon-phonon scattering strength ($\tau_{pp,i}^{-1}$). Recently, we reported neutron scattering signatures of acoustic phonon eigenvector renormalizations in NiO [119]. The eigenvectors of transverse acoustic phonons are renormalized to a lower symmetry (as shown in Section 3.7 Figure 3.13), resulting in INS intensities ‘forbidden by symmetry'. The renormalizations are not caused by magnetostriction-induced static lattice distortion. Instead, they originate from spin-phonon interactions, which dynamically break the symmetry of the phonons. Because the selection rules for phonon-phonon scattering depend on the symmetry of phonon eigenvectors [120], eigenvector renormalizations could affect phonon transport. Generally, higher symmetry imposes more restrictions (additional selection rules) on the phonon-phonon scattering process, resulting in weaker phonon-phonon interaction strength and therefore higher thermal conductivity [120]. On the contrary, dynamic symmetry breaking of the phonon system leads to a stronger phonon-phonon interaction strength, and thus lower thermal conductivity in NiO. This effect is not included in the calculated κ_p due to its dynamic nature.

Near T_N (450-550 K), the kink in the heat capacity is a measure of the entropy in the lattice and spin system due to the phase transition. Because the measured thermal effusivity shows no kink there, the increase in heat capacity (caused by an increase in disorder through the phase transition) is compensated by a corresponding decrease in thermal conductivity. This suggests that the average phonon lifetime is inversely proportional to the disorder in the spin system. The dip in thermal conductivity is attributed to critical magnetic fluctuation-phonon scattering [121].

The measured thermal conductivity shows a weaker temperature dependence of T¬-1.0 above T_N. It has been shown that the slight structural distortion from magnetostriction hardly affects the thermal conductivity by phonon transport in NiO [101]. The measured κ is still lower than the calculated κ_p (natural isotope with defects) at 550-700 K, suggesting that the effects from spin-phonon interactions may still be significant above

T_N. This is expected because paramagnons (Section 3.7 Figure 3.8) and phonon eigenvector renormalizations [119] are observed in this temperature range. As a result, the effects from magnon-phonon scattering and spin-induced dynamic symmetry breaking do not vanish. Although there is no long-range spin order in this state, a short-range spin order exists and may give rise to the spin-phonon interaction. Suppression of thermal conductivity by spin-phonon interactions was also found previously in other materials in the PM state [94, 122].

Generally, one would expect the melting of antiferromagnetic order to do one of two things to magnon-phonon scattering rates above the T_N. Either magnon-phonon scattering rates would saturate, i.e. stop increasing with temperature because the entropy in the spin system has been maximized. Or, magnon-phonon scattering would vanish due to the lack of antiferromagnetic order. If the magnon-phonon scattering rates saturate, i.e., $\tau_{mp,i}^{-1}$ became temperature independent above T_N, then the above expression for thermal conductivity predicts a T^{-n} dependence with $n < 1$, like is observed in insulating crystals with significant crystalline disorder. Alternatively, if magnon-phonon scattering vanishes due to the lack of spin order, then the thermal conductivity should recover. These seem to contradict the observed temperature dependence. In the present case, we observed the existence of paramagnons above T_N below 640 K (Section 3.7 Figure 3.8). This indicates that magnetic entropy is not yet maximized in this temperature range, and strong short-range spin correlations give rise to coherent paramagnons. The paramagnon-phonon scattering may contribute to the suppression of thermal conductivity above T_N.

Another possible mechanism for the observed temperature dependence above T_N is that changes in the antiferromagnetic order lead to changes in phonon-phonon scattering rates. This could occur for several reasons. One possibility is spin-disorder effects bonding [123], which could lead to an increase in anharmonicity. To explore the effect of spin order on phonon anharmonicity, we calculated the phonon properties with ferromagnetic (FM) spin order to understand the effects of magnetic order (see 3.3.4). The obtained phonon mode Grüneisen parameters (Section 3.7 Figure 3.14) as well as temperature-dependent mode energies (Section 3.7 Figure 3.15) show only minor changes compared with those in the AFM state. However, we note that the temperature dependence of the INS measured phonon frequencies is higher near the T_N than what our calculations for NiO in the AFM or FM state predict. Thus, the spin-phonon interaction on the phonon thermal conductivity can be indirect: melting of the spin order causes changes in phonon anharmonicity, which leads to larger phonon-phonon scattering rates in the PM vs. AFM phase.

The TA, LA, TO, LO decrease in energy of 3%, 3%, 5%, 4% from 50 to 640 K, respectively (Figure 3.4 a,b & Section 3.7 Figure 3.6 c,d). We calculated the 3-phonon scattering phase space at 0 and 640 K and found that the phonon-phonon scattering phase space changes little (see Section 3.7 Figure 3.17). Therefore, temperature-dependent DFT, such as molecular dynamics calculations shall not change the results significantly.

3.6 Summary

In summary, by performing INS and TDTR thermal conductivity measurements and atomistic thermal conductivity calculations, spin-phonon interactions are identified as the origin of the strong temperature dependence of thermal conductivity in the AFM phase. Using the extrapolated magnon lifetime from INS measurements, the magnon thermal conductivity is estimated to be more than one order of magnitude smaller than its phonon counterpart in the temperature range studied. In the AFM phase, the measured thermal conductivity at 200~450 K shows a strong temperature dependence of $T^{-1.5}$. We ruled out phonon-isotope scattering, phonon-defect scattering, and phonon softening as the source of the anomalous temperature dependence. The stronger temperature dependence is attributed to magnon-phonon scattering and spin-induced dynamic symmetry breaking. Our results provide a detailed study of thermal transport in this important material, highlighting the pivotal role of spin-phonon interactions in lattice thermal transport. Similar interactions and their effects may play significant roles in thermal transport in other materials where spin and lattice degrees of freedom are strongly coupled. The results shed light on controlling thermal transport through spin-phonon interactions and engineering functional antiferromagnetic spintronics materials through these interactions.

3.7 Supplementary information

3.7.1 Supplementary figures

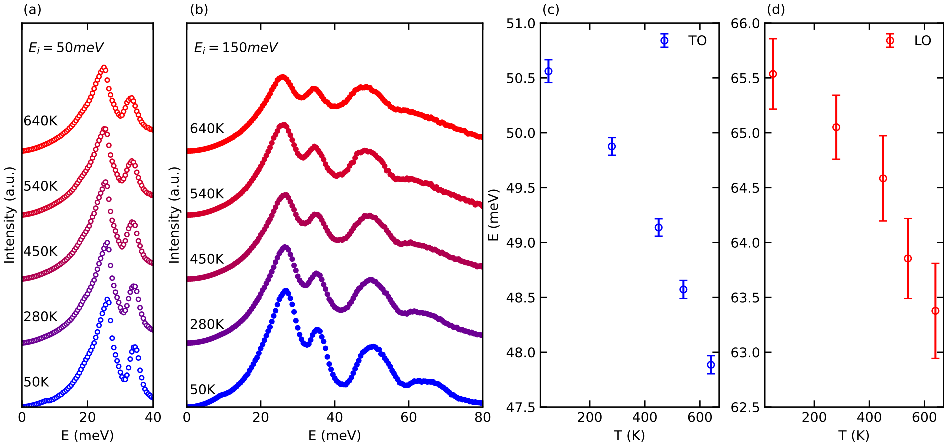

Figure 3.6: Temperature-dependent neutron-weighted phonon density of states and temperature-dependent optical phonon energies. (a, b) Neutron-weighted phonon density of state measured with an incident have of E=50 meV (empty circles) and E=150 meV (dots) at 50,280,450,540 and 640 K. Experimental data has been corrected for multiphonon scattering and thermal occupation. (c, d) TO, LO phonon energies are extracted from Lorentzian fitting of the measured data, and error bars indicate fitting errors.

In Figure 3.6 c,d, the energies of the transverse optical (TO) and longitudinal optical (LO) phonons decrease with temperature.

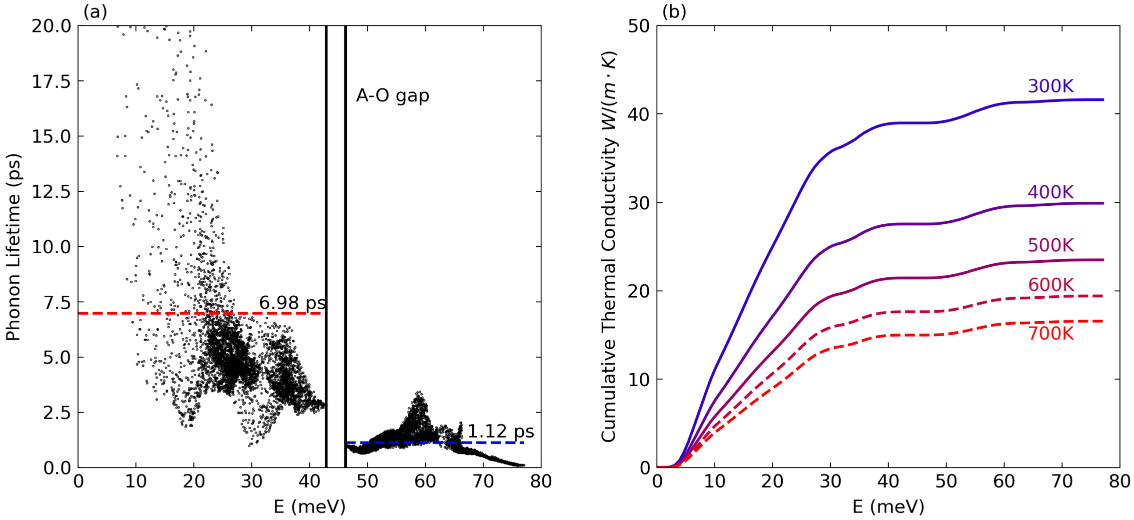

Figure 3.7: (a) Calculated phonon lifetimes of NiO at 300K at a 20×20×20 q-mesh. Averaged phonon lifetimes for acoustic (optical) phonons are denoted by red (blue) dashed lines. The black lines represent the acoustic-optic (A-O) gap. (b) Cumulative thermal conductivity of the phonon system at various temperatures. The thermal conductivity is dominated by acoustic phonon modes below 30 meV at all temperatures.

As shown in Figure 3.7 a, the calculated average phonon lifetime of acoustic phonon modes (6.98 ps) is longer than that of optical modes (1.12 ps), suggesting that acoustic modes dominate lattice thermal transport. This can be clearly seen in Figure 3.7 b. The calculated phonon dispersions show an acoustic-optic gap at around 45 meV. Acoustic phonon modes below 45 meV contribute more than 90% of the total thermal conductivity at 300-700K. The phonon lifetimes cannot be resolved in our INS measurements due to the instrument energy resolution. The calculated average phonon lifetimes of the acoustic modes and optical modes are 7.0 and 1.1 ps at 300 K, respectively. The corresponding phonon linewidths are around 0.05 and 0.29 meV (HWHM), well below the instrument energy resolution of 1-2.5 meV (HWHM, below 120 meV in neutron energy transfer for Ei = 150 meV).

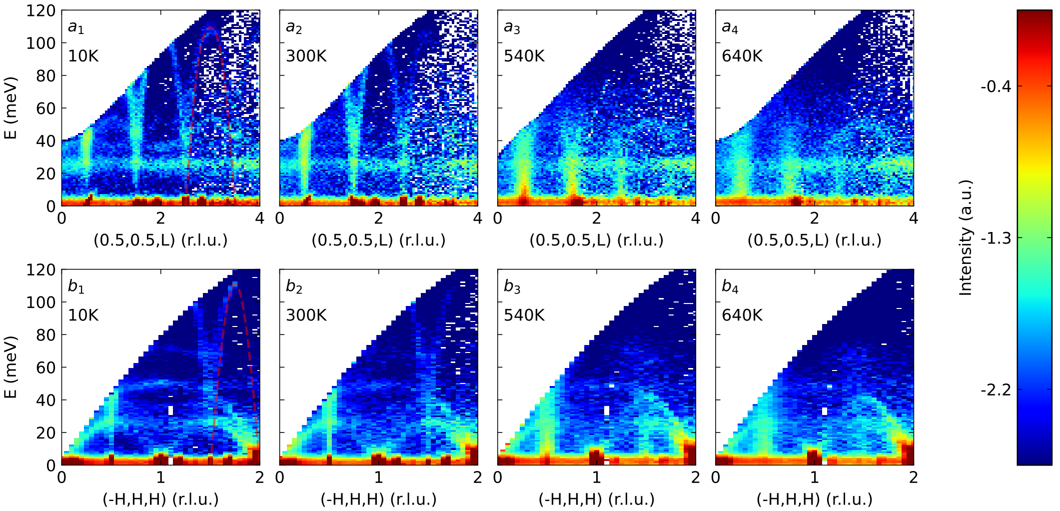

Figure 3.8: Measured INS dynamic structure factor S(Q,E) at 10, 300, 540 and 650 K in small Q region for [0,0,1] (a1-4) and [-1,1,1] (b1-4). Measured S (Q, E) is integrated over ±0.1 (r.l.u) along the perpendicular axes and plotted on the logarithmic color scale. The calculated magnon dispersions are overplotted with the measured S(Q,E) at 10 K in red dashed lines.

As can be seen in Figure 3.8 a1, b1, the calculated magnon dispersions show great agreement with the measurements. Clear magnon signals at (0.5,0.5,0.5), (0.5,0.5,1.5), and (-0.5,0.5,0.5) in the paramagnetic phase indicate the emergence of coherent paramagnons (Figure 3.8 a3, a4; b3, b4).

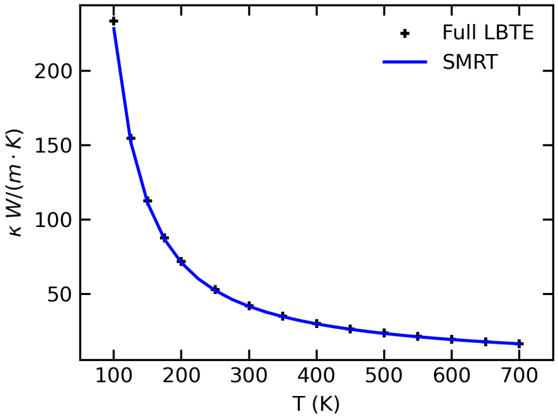

Figure 3.9: Comparison of the calculated phonon thermal conductivity κ_p (natural) using the direct solution of LBTE (black label) and the SMRT approximation (blue curve).

The calculated κ_p using SMRT approximation and direct solution of LBTE show little difference (smaller than 2.5% at 100-700 K).

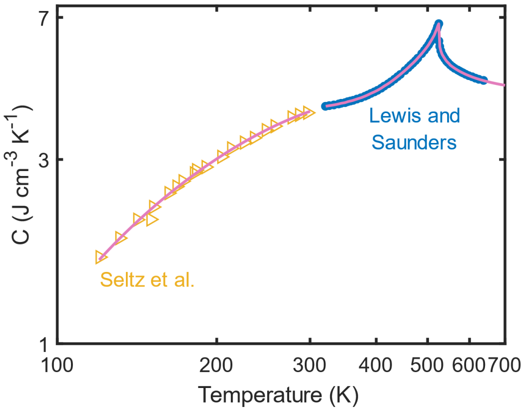

Figure 3.10: Heat capacity of NiO. Labels indicate previous measurements, and curves show the extrapolations.

We used experimental results from literature for the heat capacity of Al and NiO at different temperatures [41, 106, 107]. For the heat capacity of NiO above 630 K, there is no experimental data. Thus, we extrapolate the experimental results in Ref. [41].

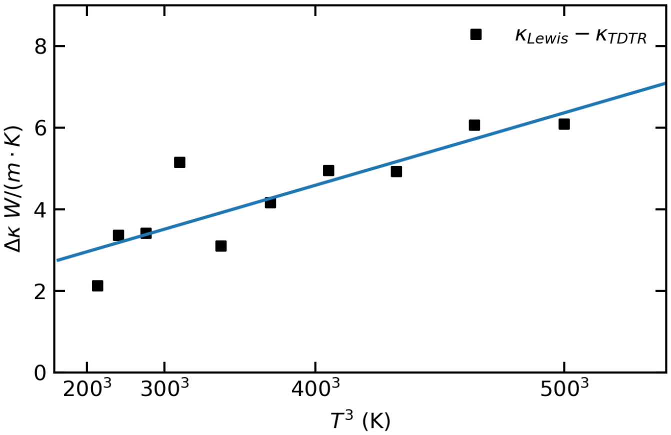

Figure 3.11: The difference between our measurements and the steady-state results [4] ($\Delta\kappa$) at 200-500 K. Black dots show the difference between NiO (I) and one set of data measured by Lewis. Blue line shows the T^3 relation fitting.

As can be seen in Figure 3.11, the $\Delta\kappa$ follows T^3 relation, suggesting that the $\Delta\kappa$ was due to radiational heat loss.

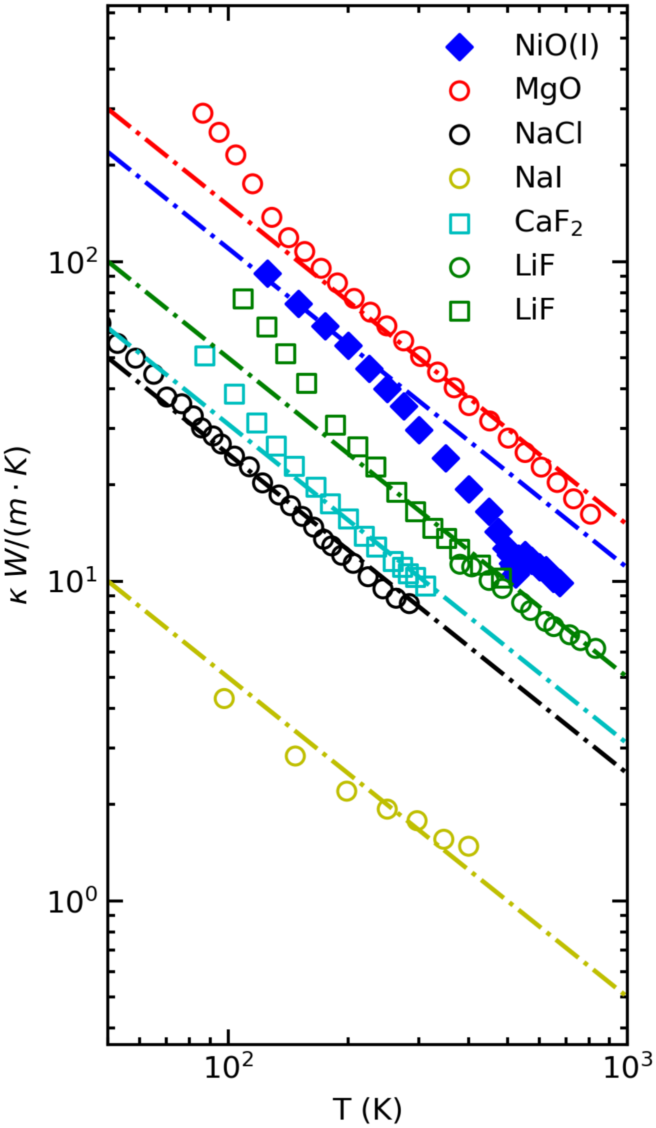

Figure 3.12: Thermal conductivity of nonmagnetic face-center-cubic insulators, including MgO [124], LiF [125, 126], CaF2 [127], NaCl [128], and NaI [129, 130]. Dashed lines show eye guides for T^{-1}

In Figure 3.12, in contrast to NiO, the measured thermal conductivity of nonmagnetic insulators with face center-cubic structure follows T^{-1}. This suggests that the strong temperature dependence in NiO may be related to the spin-phonon interaction.

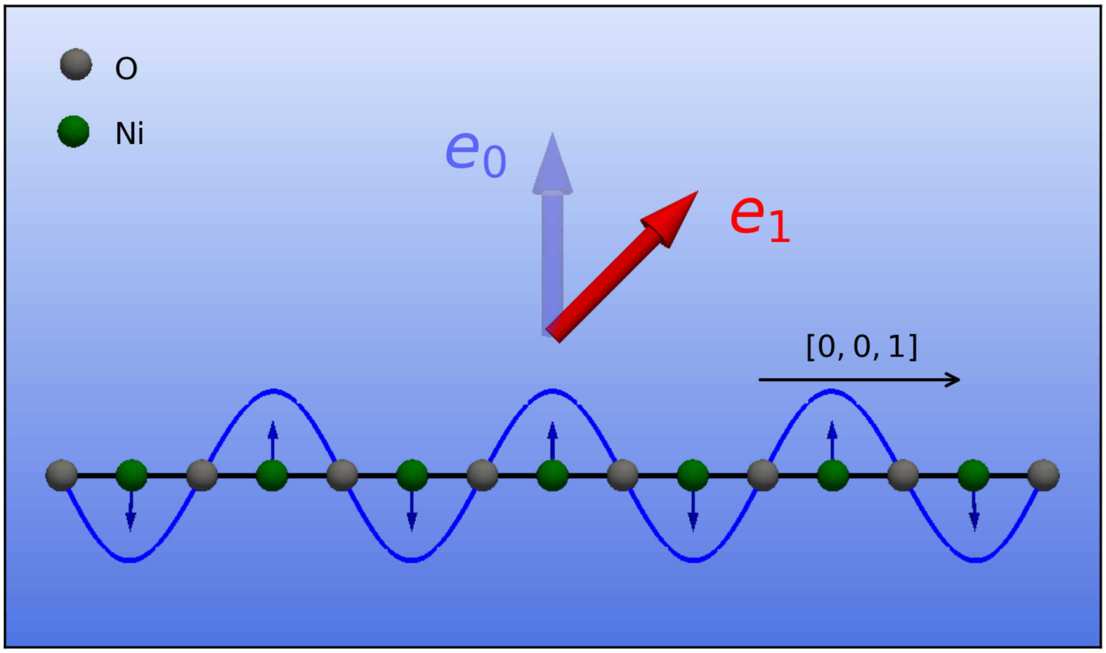

Figure 3.13: A schematic of phonon eigenvector renormalization. Blue arrows and curves illustrate the motions of nickel atoms for transverse acoustic phonon at Brillouin zone boundary. The black arrow indicates the phonon propagation direction. The light blue and red arrows indicate the original and renormalized phonon eigenvectors, respectively.

The "geometry-forbidden" INS intensities at large momentum transfer (Q) that follows the dispersion of transverse acoustic phonon were observed [119]. The INS intensities are from lattice INS and indicative of phonon eigenvector renormalization induced by spin-phonon interactions. A sketch of phonon eigenvector renormalization in Figure 3.13. e_0 shows the direction of eigenvector of nickel ions imposed by crystal symmetry. Due to spin-phonon interactions, the eigenvector is renormalized to e_1, which give rise to non-trivial $|Q \cdot e|$ (Q=(0,0,L); $L > 4$ r.l.u.), and thus the observed "geometry-forbidden" INS intensities [119]. In this case, the phonon system experienced a dynamic symmetry breaking induced by spin-phonon interactions.

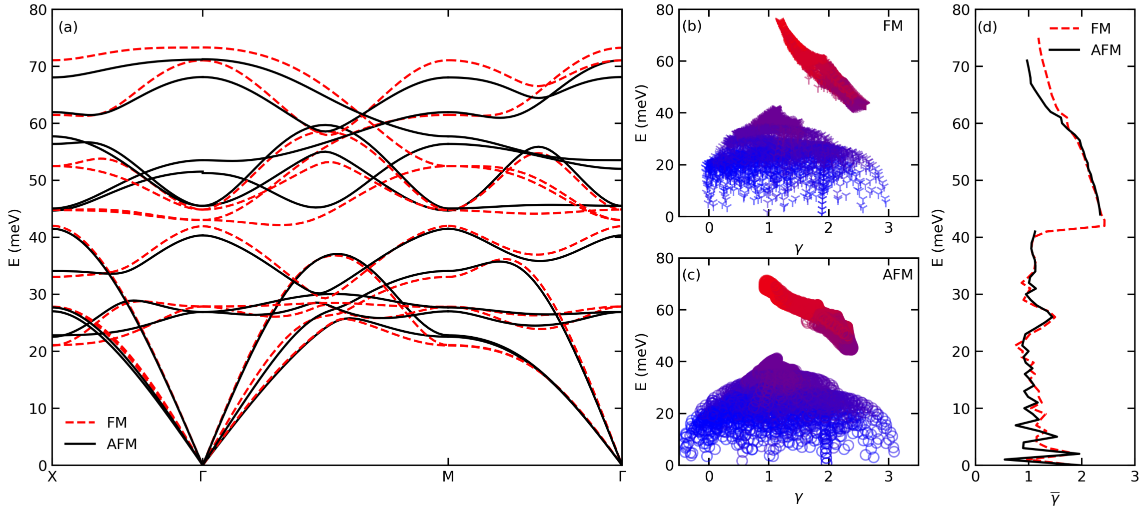

Figure 3.14: Comparison between calculated phonon properties with ferromagnetic (FM) and antiferromagnetic (AFM) spin order. (a) Phonon dispersion with FM (red) and AFM (black) spin order. (b,c) Phonon mode Grüneisen parameter (γ) with FM (b) and AFM (c) spin order. The colors denote different phonon branches. (d) Energy-dependent averaged γ with FM (red) and AFM (black) spin order.

To investigate how intrinsic phonon properties change in the AFM-PM phase transition, we calculated phonon dispersions and mode Grüneisen parameter with FM spin order as an approximation to those in PM state. As shown in Figure 3.14, changing the spin order from AFM to FM results in slight change in phonon mode energies and Grüneisen parameter. This suggests no abrupt change of phonon properties in the AFM-PM phase transition and is consistent with our INS data on polycrystalline sample.

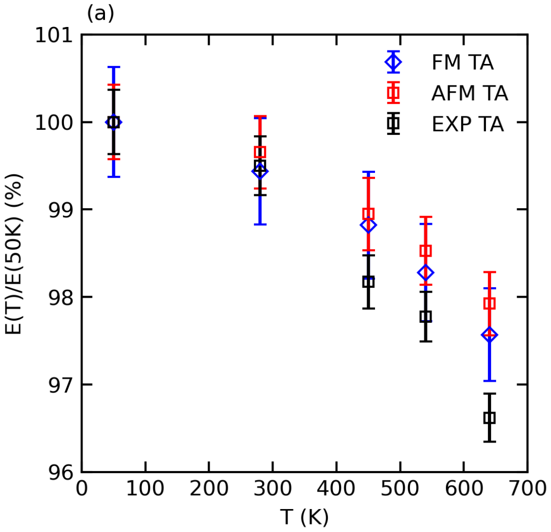

Figure 3.15: Normalized phonon energies with FM (blue) and AFM (red) spin order for TA (a) and LA (b) phonons at 50, 280, 450, 540 and 640 K. The phonon energies are obtained from Lorentzian fitting of the calculated temperature dependent phonon density-of-state (see text). The results are compared with the measured phonon energies by INS (black). Error bars indicate fitting errors.

The temperature-dependent phonon density of state can be expressed by

$$D(\omega,T)=\frac{1}{A}\sum_{q,j}\delta(\omega-\omega_{qj}(1-\gamma_{qj}\frac{\Delta V(T)}{V}),$$

where A is a normalization factor, ω_{qj} and γ_{qj} are the calculated phonon energy and mode Grüneisen parameter for branch j at reciprocal point q. $\Delta V(T)/V$ is the ratio of volume change, where $\Delta V(T)$ and V were obtained using literature value in Ref. [131]. The $D(\omega,T)$ was calculated numerically using a 20×20×20 q mesh. As shown in Figure 3.15, the difference of the obtained phonon energies between FM and AFM state is small.

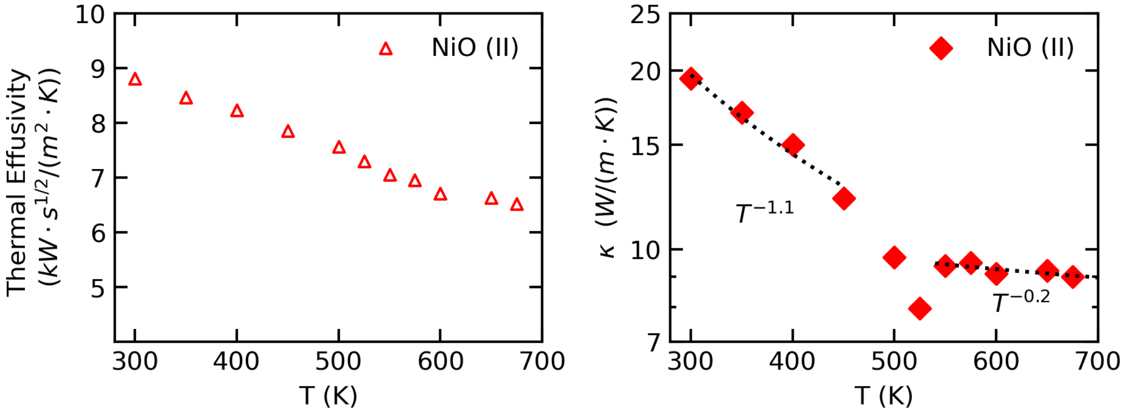

Figure 3.16: (a) Thermal effusivity of NiO measured by TDTR. (b) Thermal conductivity of NiO (II).

For NiO (II), we observe lower thermal effusivity than NiO (I) (Figure 3.3a). The thermal conductivity is lower and its temperature dependence is weaker than NiO (I) (Figure 3.3d). High-quality nonmetallic single crystals typically have a κ that is proportional to T^{-1} in the high temperature limit. However, defects can decrease the temperature dependence of κ [132]. Therefore, we believe that NiO (II) has a higher defect concentration than NiO (I), and that κ of NiO (I) in Figure 3.3 c is more representative of the intrinsic transport properties of NiO.

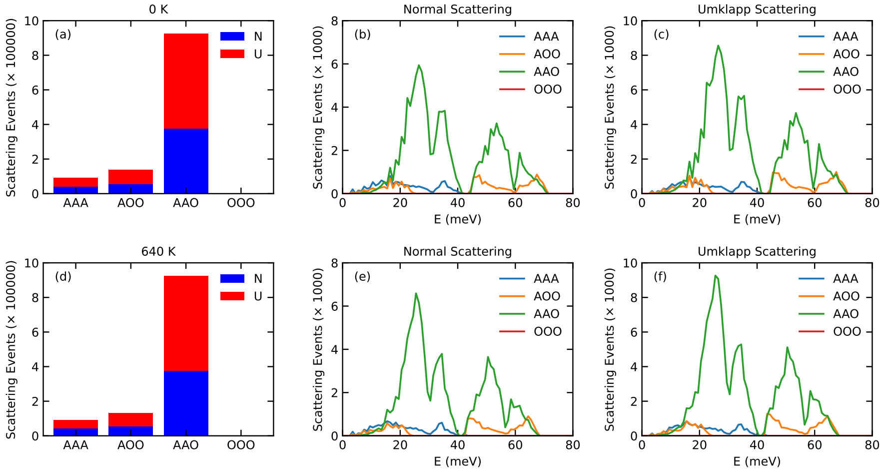

Figure 3.17: 3-phonon scattering phase space at 0 and 640 K. (a, d) Bar plots of scattering phase space categorized by AAA, AOO, AAO, OOO in normal and Umklapp processes at 0 (a) and 640 (d) K. (b, e) Energy-dependent scattering events of normal scattering. (c, f) Energy-dependent scattering events of Umklapp scattering.

We investigated the effect of phonon energy change in 3-phonon scattering phase space. This was done by calculating scattering events using the calculated phonon dispersions at 0 K (see Sect. 2.3.2) and phonon dispersions at 640 K obtained with experimental phonon softening (3% softening of acoustic phonons and 4.5% softening of optical phonons). The scattering phase spaces were calculated based on 20×20×20 q mesh, which is the same as the q mesh from which we obtain the thermal conductivity (see Sect. 2.3.2). The energy conservation of the 3-phonon scattering process was evaluated with an energy tolerance of 0.5 meV. The results were categorized into AAA, AAO, AOO, and OOO processes, in which A and O stand for acoustic and optical phonons. The total scattering space decreases 0.5% from 0 to 640 K (a, d). As can be seen in Figure 3.17 (b, c, e, f), the difference of energy-dependent scattering phase space between 0 and 640 K is little. Therefore, we conclude that the phonon-phonon scattering phase space varies little from 0 to 640 K.

Chapter 4

Temperature-dependent spin dynamics in Cr_2O_3

4.1 Abstract

Cr_2O_3 emerges as a prominent candidate material for spintronics and magnetoelectronic applications. However, a comprehensive understanding of its temperature-dependent spin dynamics remains elusive, impeding the engineering of novel spintronics based on this material. We delve into this through a combination of inelastic neutron scattering experiments and atomistic simulations. Our results unveiled the emergence of paramagnons above and below T_N. We demonstrated a significant softening of linear magnons upon heating in the antiferromagnetic state. Further analysis revealed that this softening primarily originated from four-magnon interactions, while thermal expansion played a minor role.

4.2 Introduction

Mott-Hubbard antiferromagnetic (AFM) insulators are promising for ultrafast spintronics [27, 28, 29, 30], memory devices [31], and spin-caloritronic applications [32, 33]. AFMs offer advantages over ferromagnets for spintronics, including robustness against external fields, negligible stray fields, ultrafast spin dynamics, and potential room-temperature operation. While spin transport in AFMs is an emerging field with challenges around efficient spin current generation, detection, and control of the antiferromagnetic order, overcoming these hurdles could enable novel high-performance spintronic devices leveraging AFMs. Characterizing and predicting temperature-dependent spin dynamics is central to the engineering of spin transport.

Chromia (Cr_2O_3) is of particular interest because it is also the prototypical magnetoelectric material that is promising for magnetic field sensors, voltage-tunable inductors, and mechanical magnetoelectric antennas. Below the Néel temperature ($T_N = 307$ K), it has a corundum-type crystal structure with lattice parameters of a = b = 4.95 Åand c = 13.57 Å, and belongs to space group 167 ($R\overline{3}C$) [42]. It has a collinear AFM spin ordering with easy-axis anisotropy along the c-axis, breaking both inversion and time reversal symmetries. In Cr_2O_3 thin films, the magnetoelectric coupling allows the manipulation of magnon polarization using an electric field [49]. A recent study highlights the formation of magnon-phonon polarons in Cr_2O_3 at low temperatures, demonstrating the potential to control spin transport via lattice excitation [60]. Previous neutron scattering experiments have provided detailed characterizations of the magnetic structure and spin dynamics, [133] but temperature-dependent spin dynamics remain unexplored.

In this work, we use inelastic neutron scattering (INS) experiments to characterize temperature-dependent spin dynamics. Atomistic calculations were performed to model INS intensities from linear magnons and separate those from damped magnetic excitations (DMEs), i.e., so-called paramagnons, at high temperatures. Theoretical quantifications of magnon energy renormalization by thermal expansion and magnon-magnon scattering are presented.

4.3 Observation of paramagnons below $\mathbf{T}_N$

Time-of-flight INS measurements were performed on single-crystal and polycrystalline Cr_2O_3 samples to investigate their dynamic properties. The experiments were carried out using the Wide Angular Range Chopper Spectrometer (ARCS) at the Spallation Neutron Source (SNS). The samples were mounted on aluminum holders inside a low-background electrical resistance vacuum furnace. For the single-crystal Cr_2O_3 sample, four-dimensional dynamic structure factors were obtained at temperatures of 50, 280, and 450 K, using an incident energy of 75 meV. Data reduction was performed using MANTID [67], with normalization by the proton current on the target and correction for detector efficiency. Two-dimensional energy-momentum ($\mathbf{Q}$-E) views of dispersions were obtained by slicing the data along high symmetry directions in reciprocal space.

For the polycrystalline Cr_2O_3 sample, two-dimensional dynamic structure factors were obtained at temperatures of 50, 150, 280, 350, and 450 K, using an incident energy of 100 meV. To account for the background from the sample holder, INS measurements were performed on an empty can at the same temperatures, and the measured intensity

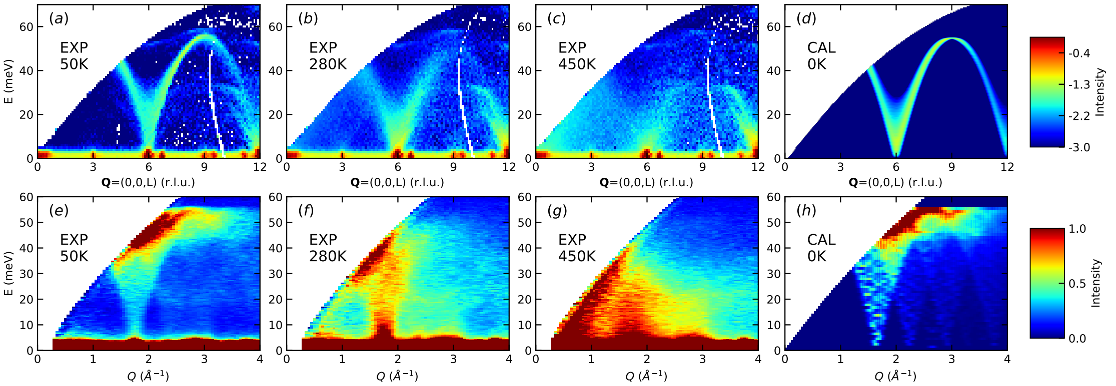

Figure 4.1: The temperature-dependent measured and calculated dynamic structure factor of Cr_2O_3. (a, b, c) The dynamic structure factor of single crystal Cr_2O_3 measured by INS on ARCS at 50, 280, and 450 K along the [0,0,L] direction in the reciprocal space. The intensity is integrated over ±0.2 (r.l.u) along the perpendicular axes and scaled by multiplying E. (d) Simulation of magnetic scattering $S(\mathbf{Q}, E)$ at 0 K with the same $\mathbf{Q}$ integration ranges. Both experimental data and theoretical calculations are plotted on a logarithmic scale. (e, f, g) The measured $S(E)$ function of polycrystalline samples at 50, 280, and 450 K at low $\mathbf{Q}$s. (h) The calculated $S(E)$ function at 0 K. In (d,h), both calculated S(E) and $S(\mathbf{Q}, E)$ is cropped by the neutron scattering kinetic limits and convoluted with instrument resolution function.

was subtracted from the polycrystalline data.

One-dimensional $S(\mathbf{Q}, E)$ slices at low neutron momentum transfer ($\mathbf{Q}$) along the [0,0,L] direction are shown in Figure. 4.1 (a-c). At 50 K, the magnon dispersion from L = 6 (r.l.u.) reaches its maximum energy ($\sim$ 55 meV) at L = 9. In Figure. 4.1 (e), polycrystalline INS data also show an energy cutoff of 55 meV at 50 K. From our calculations, we found $J_1 = -15$ meV, $J_2 = -6.8$ meV and $J_3 = -0.5$ meV, which align very well with the measurements, as can be seen by comparing Figure. 4.1 (a) to (d) and (h) to (e). These exchange parameters significantly differ from the results of a previous piezospectroscopic study for exchange-coupled Cr^{3+} in ruby ($J_1 = -28$ meV, $J_2 = -12$ meV, and $J_3 = -1.4$ meV) [134] and (nearly two times of) previous neutron scattering work on Cr_2O_3 ($J_1 = -7.4$ meV, $J_2 = -3.3$ meV and $J_3 = -0.2$ meV) [133]. The latter difference may arise from double counting of exchange neighbors in their analytical model, although the model also predicts the magnon dispersion well. On the other hand, the ratio, $J_2/J_1 = 0.45$, is in agreement with the neutron scattering work [133] while disagreeing with the theoretical predictions of $J_2/J_1 = 0.7$ [135]. In Figure. 4.1 (c), the strong scattering intensities near $L = 6$ indicate the existence of paramagnons at 450 K. For better illustration, constant-E slices were obtained by integrating $10 < E < 30$ meV to investigate Q and temperature dependence. As shown in Figure. 4.2 (a), the calculated lattice + magnetic scattering intensities (see 1.3.2 and 1.3.1) show excellent agreement with the measured intensity at 50 K, proving the reliability of the method. At 450 K, the measured intensities near $L = 6$ cannot be solely modelled by lattice scattering (see Figure. 4.2 (c)), and the sizable difference in intensities is from INS by paramagnons.

Compared to 50 K data, paramagnons above T_N have much lower energies and shorter lifetimes. The damped paramagnon intensities disappear above 35 meV and significantly broaden, as shown in Figure. 4.1 (c). The paramagnons have an energy range similar to that of longitudinal acoustic phonons (LA) near $L = 6$ and 12. The weak intensities from LA near $L = 6$ are unlikely from magneto-vibrational scattering as was observed in nickel oxide [119] because they are absent at 50 K.

In the context of this study, it is crucial to distinguish a magnon and a paramagnon. They are both collective quantum excitations. Magnons emerge in the ordered phase and arise from the alignment of neighboring spins. In contrast, paramagnons manifest in the paramagnetic (PM) phase at high temperatures, where thermal energy dominates, leading to a nonmagnetic average state. Instead of long-range spin correlation, the paramagnons

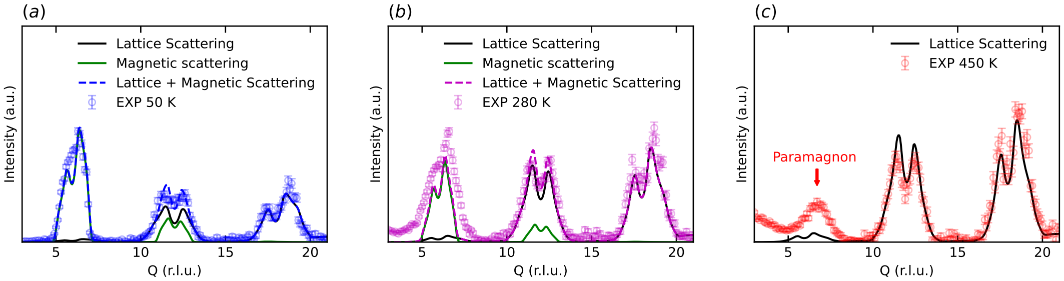

Figure 4.2: Evidence of paramagnons and short-range correlation near and above T$_N$. (a, b, c) The measured constant-E slices at 50, 280, and 450 K compared with the atomistic simulations. Colored dots represent the intensities obtained by integrating $10 < E < 30$ meV of the measured data along [0,0,L] with background subtraction. The error bars indicate uncertainties in the data. The simulation of magnetic (lattice) scattering intensity at the same temperature with the same integration range is shown by the green line (black line), and the magnetic + lattice scattering intensity is indicated by blue (50 K) and purple (280 K) dashed lines.

arise from coupling within or between short-range magnetic clusters in materials [136]. The intensity of magnetic Bragg reflection is subject to the spin-spin pair correlation function, which on a statistical average, is proportional to the sublattice magnetization and reflects the long-range spin order. We analyzed the intensity variation of magnetic Bragg reflection at $|\mathbf{Q}|$=1.72 Å^{-1} with temperature. As shown in Section 4.6 Figure 4.4, the magnetic Bragg peaks vanish above T$_N$, indicating long-range spin order is lost in the paramagnetic phase. The emergence of paramagnons is beyond the theory of linear magnon, which is based on small perturbations on the long-range spin correlations. Instead, they arise from short-range magnetic order and undergo diffuse transport, suggesting that the entropy of the spin degree of freedom is not yet maximized at 450 K.

At 280 K, scattering intensities near L = 6 cannot be solely modelled by magnetic INS by linear magnons, suggesting the presence of overdamped magnetic excitation. On the neutron energy loss side, the magnetic scattering cross section can be written as,

$$\frac{d\sigma^2}{d\Omega dE} = A|F(\mathbf{Q})|^2 e^{-2W} \frac{\chi^{''}(\mathbf{Q}, E)}{1 - e^{-E/k_B T}} \tag{4.1}$$

where A contains temperature-independent INS coefficients, $F(\mathbf{Q})$ is the magnetic form factor of Cr^{3+}, e^{-2W} is the Debye-Waller term, $\chi^{''}(\mathbf{Q}, E)$ is the generalized susceptibility. $1/(1 - e^{-E/k_B T})$ is the thermal occupation factor, where k_B is the Boltzmann constant, T is the temperature. Assuming that the magnetic form factor and the Debye-Waller term change little with temperature, the temperature dependence of the magnetic INS intensity is subject to that of $\chi^{''}(\mathbf{Q}, E)$. Neglecting magnon energy renormalization, the variation of $\chi^{''}(\mathbf{Q}, E)$ depends on sublattice magnetization and can be modelled by the variation of magnetic Bragg peak intensity I on heating. The magnetic intensity at 280 K can be represented using that at 50 K,

$$\frac{d\sigma^2}{d\Omega dE}(280K) = \frac{1 - e^{-E/50k_B}}{1 - e^{-E/280k_B}} \frac{I_{280K}}{I_{50K}} \frac{d\sigma^2}{d\Omega dE}(50K) \tag{4.2}$$

As shown in Figure. 4.2 (b), the measured intensity is non-trivial at $L < 6$ and is stronger than the calculated results for INS by magnons. The ratio between calculated and experiment magnetic INS intensity by integrating $4 < L < 8$ is 0.54, suggesting that nearly half of magnetic intensities at 280 K originate from paramagnons, similar to 450 K. The coexistence of magnons and paramagnons below T_N is seldom discussed, yet it is expected because only ~33% of long-range spin order is preserved at this temperature (see Section 4.6 Figure 4.4 (b)), and such paramagnons can arise from short-range spin order. Note that excluding the Debye-Waler effect overestimates the calculated scattering intensity and would not change the result.

Paramagnons are also observed in the measured magnon density of states (DOS) by polycrystalline INS at 280 K. The data were obtained by integrating $2.5 < |\mathbf{Q}| < 4$ Å^{-1} to avoid the no-data region limited by neutron scattering kinetic limit and with background subtractions using data from $4 < |\mathbf{Q}| < 4.5$ Å^{-1} to remove lattice scattering. The quasi-elastic diffuse scattering intensity was removed (see Section 4.6 Figure 4.5), and thermal occupation corrections were applied. Above T$_N$, the measured 350 and 450 K data show clear bumps spanning a broad energy range centered near 25 meV, showing the feature of paramagnons (see Figure. 4.3 (b)). These differ from 50 and 150 K data, where the intensities are much weaker due to steep slopes of magnon dispersions and small magnon DOS in this energy range. The bumps are not likely from INS by magnons because linear-like magnon dispersions lead to an E^2 dependence in DOS, as shown by the scattering intensities at 50 and 150 K below 35 meV in Figure. 4.3 (b). The paramagnon scattering is nearly constant in intensity and energy distribution at 350 and 450 K, similar to that observed in Li-doped MnTe [137]. Notably, a similar bump that does not follow the E^2 trend also shows up at 280 K, supporting the presence of paramagnons.

4.4 Temperature-dependent spin dynamics

In the AFM phase, the entire magnon dispersion along the [0,0,L] direction shows a 13% softening from 50 to 280 K, as shown in Figure. 4.1 (a,b). The softening of magnon energies is also observed in the data from polycrystalline measurements shown in Figure.

4.3 (b). To obtain pure magnon intensity at 280 K, the intensity of paramagnons was subtracted using 450 K data with a factor of 0.66, as shown in Figure. 4.3 (b,e). The ratio of the linear magnon intensity to the total intensity is 0.54, consistent with the ratio obtained from single crystal results. In Figure. 4.3 (d), the average magnon energies are represented by the center of mass of the measured data. The average magnon energy at 50 K is 45.7 meV, showing 5% and 14% softening from 50 to 150 K and 50 to 280 K, respectively.

To include the effects of temperature change on magnon energy, we consider the magnon system described by the Hamiltonian $\mathcal{H} = \mathcal{H}_{non-int} + \mathcal{H}_{int}$, where $\mathcal{H}_{non-int}$ contains the ground state energy E_0 and the total energy of non-interactive magnons $\sum_k \hbar\omega_k c_k^\dagger c_k$, and the $\mathcal{H}_{int}$ represents the interactions of magnons with themselves and other elementary excitations in the crystal, such as phonons.

4.4.1 Effect of thermal expansion on magnon energies

We first consider the effect of thermal expansion on $\mathcal{H}_{non-int}$. Thermal expansion modifies the overlaps of electron orbitals and consequently changes the exchange coupling and the anisotropy energy. The anisotropy term changes little with heating because the spin wave bandgap is ~0.68 meV [133]. The lattice deformation is known to result in a non-trivial change in the exchange coupling constants [16] and the temperature dependence of $\mathcal{H}_{non-int}$ is subject to that of the exchange coupling constants J_n.

Ab initio density functional theory (DFT) calculations were performed using the Vienna Ab initio Simulation Package (VASP) [69, 70] with a plane-wave basis set and

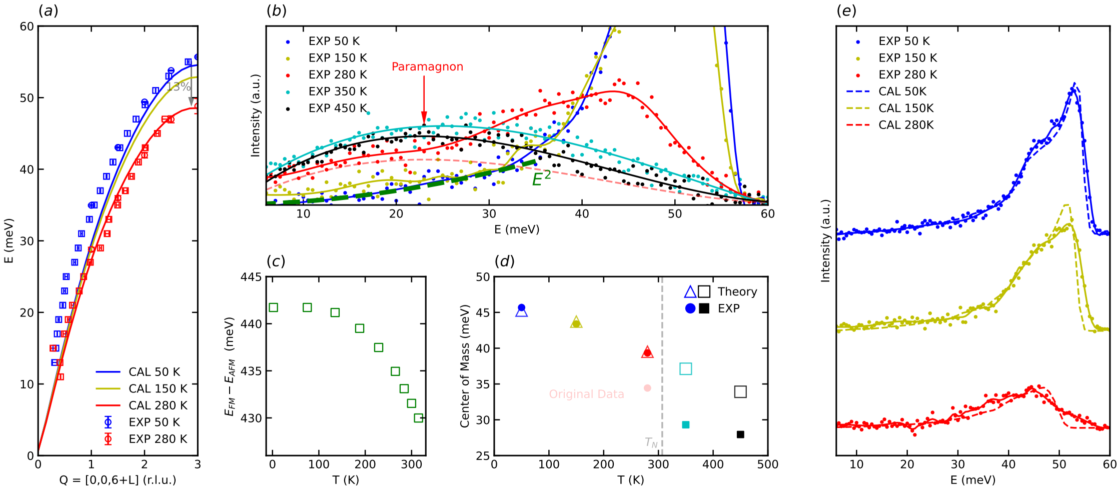

Figure 4.3: Temperature-dependent magnon energy shifts from experiments and theories. (a) The measured and the calculated magnon dispersions at 50 and 280 K in the [0,0,L] direction. The experimental magnon energies were extracted from Gaussian fittings of the constant-**Q** (circles) and constant-E (squares) of the measured $S(\mathbf{Q}, E)$ at 50 (blue) and 280 (red) K. The error bars represent fitting uncertainties. (b) Dots show measured scattering intensity from polycrystalline samples at 50, 150, 280, 350, and 450 K. Curves are guides for the eyes. The quasi-elastic diffuse scattering intensities were removed, and the data were corrected by thermal occupation. The red dashed line shows intensity from paramgnons at 280 K. (c) Green dots show the temperature-dependent total energy difference between the AFM and FM spin configurations (see text). (d) Solid (empty) markers show the center of mass of the measured (calculated) $S(\mathbf{Q}, E)$, which is indicative of magnon softening. (e) The measured polycrystalline data (dots, curves are eye guides.) are compared with magnon DOS calculations (see text) at 50, 150, and 280 K. The 280 K INS data were obtained by subtracting paramagnon intensities (see text). The calculated curves were convoluted with the instrument resolution function and normalized to the sublattice magnetization.

projector augmented wave (PAW) pseudopotentials [71, 72]. Generalized gradient approximation (GGA) exchange-correlation functionals [104] and the Hubbard-U model [74] with $U - J = 3.5$ eV were used. An energy cutoff of 550 eV was used for all calculations. The conventional unit cell containing 12 chromium and 18 oxygen atoms was used with a Gamma-centered k-point grid of $9 \times 9 \times 9$. The temperature-dependent electronic total energies of collinear AFM and FM spin order are calculated with the literature lattice constants [138], for which the ab axes expand and the c axis contracts with the increase in temperature, and both are nonlinear.

The energy difference $\Delta E = E_{FM} - E_{AFM}$ corresponds to two times of $\mathcal{H}_{non-int}$ for 12 Cr and 18 O atoms and agrees with $-12J_1 - 36J_2$ obtained from our INS data (424.8 meV). The obtained ΔE decrease little with temperature-induced thermal expansion (2% from 2 to 284 K), indicating a slight weakening of the exchange interaction strengths on thermal expansion. The magnon energies depend linearly on exchange parameters. Clearly, the observed softening of magnon energies ($13 \sim 14\%$) cannot be solely explained by thermal expansion with the noninteractive magnon picture.

4.4.2 Magnon softening by four-magnon scattering processes

Magnon interactions are related to the scattering processes, which cause both the renormalization of the magnon energy and the reduction of the magnon lifetime. In Cr_2O_3, the magnon-electron scattering process is mostly absent due to the large electron band gap (3.37 eV) [139]. Three-magnon scattering, four-magnon scattering, and magnon-phonon scattering contribute to the $\mathcal{H}_{int}$. Notably, the three-magnon interactions arise from the dipolar energy and do not contribute to the magnon energy renormalization [140, 141].

In this context, we considered the four-magnon scattering due to the exchange interaction [141, 142],

$$\begin{aligned}\mathcal{H}^4_{exc} = \quad & \sum_i \frac{z_i J_i}{4N} \sum_{\substack{\mathbf{k}_1,\mathbf{k}_2\\ \mathbf{k}_3,\mathbf{k}_4}} \Delta(k)[\gamma_i(\mathbf{k}_1) + \gamma_i(\mathbf{k}_2) + \gamma_i(\mathbf{k}_3) \\ & + \gamma_i(\mathbf{k}_4) - 4\gamma_i(\mathbf{k}_4 - \mathbf{k}_1)] c^\dagger_{k_1} c^\dagger_{k_2} c_{k_3} c_{k_4} \end{aligned} \tag{4.3}$$

where z_i is the number of ith nearest neighbors, N is the number of spins in the crystal, J_i is the exchange parameter for ith nearest neighbors, and γ_i (k) is the structure factor defined by

$$\gamma_i(\mathbf{k}) = \frac{1}{z_i} \sum_{\vec{\delta}} e^{i\mathbf{k}\cdot\delta_i} \tag{4.4}$$

where δ_i represents the vector connecting a spin to its z_i nearest neighbors. We approximate $\mathcal{H}^4_{exc}$ by considering two modes, the magnon of interest with wave vector $\mathbf{k}$ and another magnon $\mathbf{k'}$. The k and $\mathbf{k'}$ correspond to any of the four wave vectors in $\mathcal{H}^4_{exc}$. This approximation may underestimate the scattering phase space of the four-magnon process. Using the random-phase approximation, $c^\dagger_{k'} c_{k'} \rightarrow \langle c^\dagger_{k'} c_{k'} \rangle = \langle n_{k'} \rangle$, the magnon energy renormalization reads [141, 142, 143],

$$\hbar\Delta\omega_k = \sum_i \frac{2 z_i J_i}{N_k} \sum_{\mathbf{k'}} (1 + \gamma_i(\mathbf{k} - \mathbf{k'}) - \gamma_i(\mathbf{k}) - \gamma_i(\mathbf{k'})) \langle n_{k'} \rangle$$

where N_k is the number of **k**-points and $\langle n_{k'} \rangle$ is the Bose-Einstein distribution,

$$\langle n_{k'} \rangle = \frac{1}{e^{\hbar\omega_{k'}/k_B T} - 1} \tag{4.5}$$

The magnon energy renormalization was quantitatively evaluated based on the analytical magnon dispersion in Ref. [133] as ω_k(0K). We chose N_k=64000 with a 40×40×40 mesh in the reciprocal space. We considered exchange interactions up to the second nearest neighbors with $J_1 = -15$ meV and $J_2/J_1 = 0.5$. Each spin has one nearest neighbor and three second nearest neighbors ($z_1 = 1$ and $z_2 = 3$). In the first cycle, $\Delta\omega_k(T)$ was evaluated based on ω_k (0K), and the magnon energies were updated by $\omega_k(T) = \omega_k(0K) - \Delta\omega_k(T)$. In the following cycles, Bose-Einstein factors are evaluated based on the renormalized magnon energies and produce new $\Delta\omega_k(T)$. These were repeated until convergence when the change of $\Delta\omega_k(T)$ is less than 0.1% for all points. The magnon energies at $T = 50$, 150, and 280 K were obtained by subtracting the converged $\Delta\omega_k(T)$ from $\omega_k(0K)$

Figure. 4.3 (a) and (e) show the experiment-theory comparison of magnon dispersion along [0,0,L] and DOS, respectively. In Figure. 4.3 (e), the calculated magnon DOS were convoluted with instrumental resolution and normalized by sublattice magnetization (see Section 4.6 Figure 4.4) to compare directly with our polycrystalline data. The calculated temperature-dependent magnon dispersion and magnon DOS aligns well with our INS data. The calculation predicts 11.1% of energy softening from 50 to 280 K. This and the 2.0 % softening induced by thermal expansion reach an excellent agreement with the softening observed from INS data (~13%). Our results suggest that magnon-magnon scattering dominates magnon energy renormalization, whereas the effect of thermal expansion on exchange coupling plays a minor role. These also imply that magnon-phonon scattering does not play a significant role.

In Figure. 4.3 (d), the energies of the center of mass of the calculated magnon DOS are consistent with that obtained from INS data at 50 and 150 K and data with paramagnon intensity subtraction at 280 K. The inconsistency between the calculation and the original INS data at 280 K supports the hypothesis that the bump intensity does not come from linear magnons. While the calculated DOS is in good agreement with 50 and 150 K INS data in line shapes, the measured spectrum at 280 K is wider than the calculated DOS. The broadening is also seen in the single crystal data at 280 K, as shown in Figure. 4.1 (b) and Section 4.6 Figure 4.6. Such broadening may originate from the intrinsic shortening of magnon lifetimes, which indicates the magnon scattering as the primary source of energy softening.

In addition, we performed calculations at 350 and 450 K to predict the energy softening of linear magnons above T_N. The center of mass from calculated DOS shows a linear decrease from 280 to 450 K. The results disagree with INS data at 350 and 450 K, indicating that these low-energy paramagnons are not a result of the magnon softening. Theoretical quantifications of paramagnon energies through Monte Carlo simulations and cluster mean-field theory [136] are beyond the scope of the current study.

4.5 Summary

To conclude, our findings reveal that the magnetic excitations observed below the T_N are comprised of two distinct components: one emanating from damped magnons arising from magnon interactions and the other originating from paramagnons that emerge due to the coupling within or between short-range spin clusters. Our results indicate that the four-magnon process is the primary contributor to the softening of linear magnons, and thermal expansion plays a secondary role. These results illuminate the intricate behaviors of these magnetic excitations near T_N, providing valuable insights into characterizing and controlling the spin dynamics of Cr_2O_3 for functional spintronics and magnetoelectronic applications.

4.6 Supplementary information

4.6.1 Supplementary figures

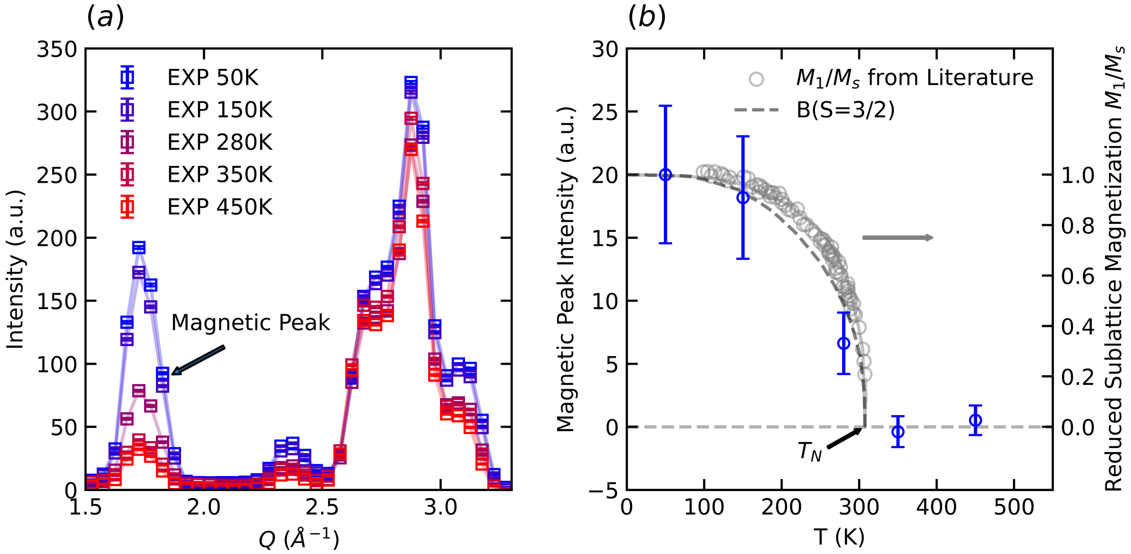

Figure 4.4: (a) Elastic scattering intensities obtained by integrating $-1 < E < 1$ meV are indicated by colored squares. Magnetic peaks near 1.7 Å^{-1} are shown. (b) Temperature-dependent intensities of the magnetic peaks obtained from Lorentzian fittings (blue circle) are compared with Brillouin function of $S = 3/2$ (grey dashed line) and sublattice magnetization from literature (grey circles) [5]. The error bars indicate fitting uncertainties.

One-dimensional slices $S(\mathbf{Q})$ representing elastic neutron scattering intensities were obtained using an E integration range of ±1 (meV). The peaks near 1.7 Å^{-1} show a dramatic intensity decrease with temperature and a clear magnetic scattering feature. These peaks are from a combination of lattice and magnetic scattering, while the peaks near 2.4 Å^{-1} are solely from lattice scattering. For lattice Bragg reflections, the intensity ratio ($I_{1.7}/I_{2.4}$) between the peak centering at 1.7 Å^{-1} vs. 2.4 Å^{-1} is 2.1. The pure magnetic intensities for the peak centering at 1.7 Å^{-1} were obtained by subtracting $I_{1.7}/I_{2.4}$ multiplying with intensities at 2.4 Å^{-1}. As shown in Figure 4.4 (b), the measured intensity below T_N shows good agreement with the Brillouin function of $S = 3/2$ and the prior literature results of sublattice magnetization [144]. Above T_N, trivial magnetic intensities illustrate nearly zero sublattice magnetization, indicating long-range spin order is lost.

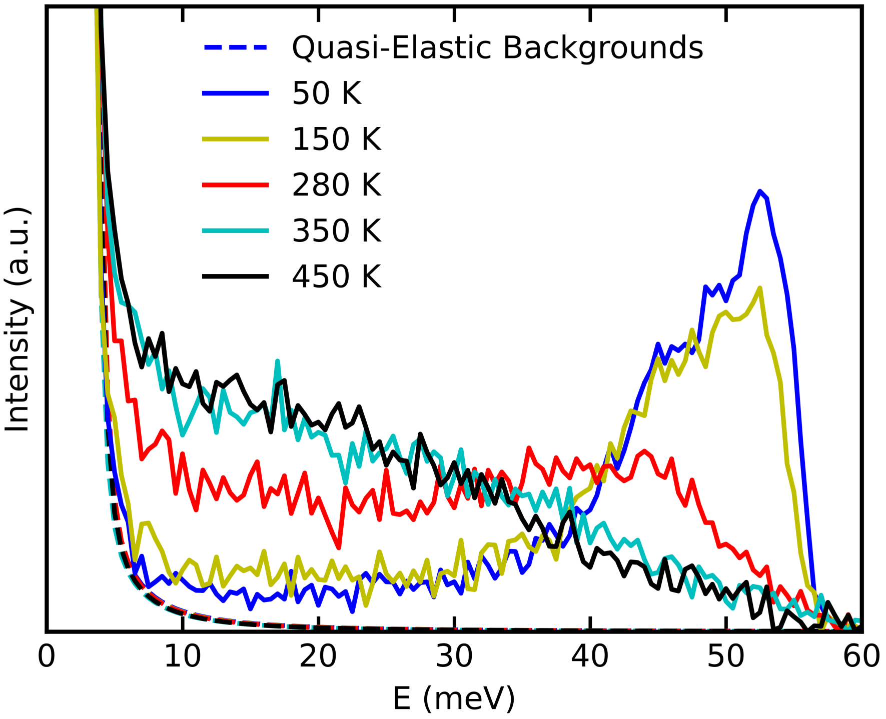

Figure 4.5: The measured intensity from polycrystalline sample at 50, 150, 280, 350, and 450 K are shown by colored lines. Quasi-elastic diffuse scattering intensities were fitted by Voigt functions and shown by dashed lines.

In Figure 4.5, polycrystal INS data obtained by integrating $2.5 < |\mathbf{Q}| < 4$ Å^{-1} are shown. One can observe strong quasi-elastic diffuse scattering intensities overwhelm magnetic scattering below 6 meV. These diffuse intensities were fitted to the Voigt function containing Gaussian and Lorentzian parts. In the fitting process, the Gaussian width parameter was set to freeze according to the instrument resolution, and other parts varied freely. The fitted diffused scattering intensities were subtracted from INS data. Intensities at $E > 6$ meV are shown in Fig. 3 (b)

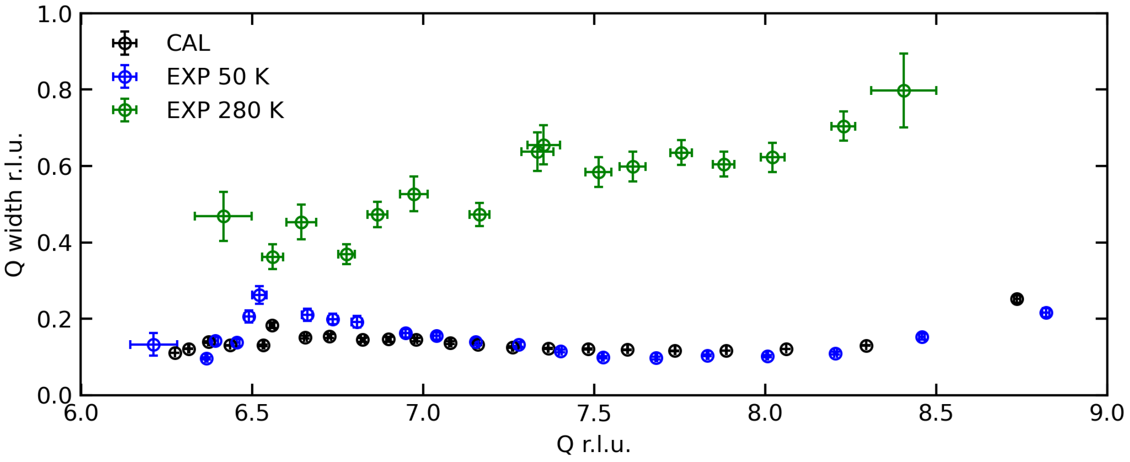

Figure 4.6: **Q**-dependent experimental and calculational **Q**-linewidths obtained from constant-E slices along the [0,0,L] direction. Horizontal and vertical error bars represent fitting errors.

Due to steep magnon dispersion, it is challenging to directly compare magnon energy linewidth from finite integration in the reciprocal space at temperatures. Instead, we obtain the **Q**-linewidth of magnon dispersion measured by INS. The larger the **Q**-linewidths, the larger the magnon energy linewidths. Constant-E slices were obtained both from INS data and simulated magnon intensities shown in Fig.1 (a,b,d). The **Q** positions and **Q**-linewidths were extracted from Gaussian fittings. In Figure 4.6, great agreement between structure factor calculation and experiment data at 50 K is shown, indicating at 50 K, the **Q**-linewidth majorly comes from instrument resolution. However, our data at 280 K show a significant broadening of **Q**-linewidth, indicating the shortening of magnon lifetimes. This suggests strong magnon interactions and supports the idea that magnon scattering causes magnon energy renormalizations.

Chapter 5

Magnetoelectric coupling induced selected phonon stiffening in Cr_2O_3

5.1 Abstract

Cr_2O_3, a prototypical magnetoelectric antiferromagnetic insulator, holds promise for innovative magnetoelectric spintronic devices. The lattice-mediated nature of magnetoelectric couplings underscores the importance of understanding lattice dynamics. Despite extensive studies on Cr_2O_3, the origin of non-linear thermal expansions below the Néel temperature and the unusual stiffening of optical phonon modes is still elusive. In this work, utilizing inelastic neutron scattering measurements and atomistic calculations, we address these questions. While most phonon modes exhibit expected softening from 50 to 450 K, we observe significant stiffening in the longitudinal optical modes, which involve changing the distances between the nearest Cr^{3+} pairs. Instead of effects from thermal expansion,

phonon anharmonicity, magnetostriction, or electron-phonon interactions, the anomalous stiffening can be attributed to the renormalization of electron states due to the change of spin order. Our calculations reveal a decrease in electron density between the nearest Cr^{3+} pairs during the magnetic transition. This leads to non-linear contractions along the c-axis and stiffened longitudinal modes. Importantly, our quantitative modeling suggests that the common belief that dynamic spin-phonon interactions are the origin of anomalous phonon energy stiffening in magnetic compounds does not work for Cr_2O_3. Our results point to a purely static magnetoelectric-coupling origin for the observed phonon stiffening, suggest the high-tunability of phonon energies in Cr_2O_3, and provide insights into controlling lattice dynamics in novel magnetoelectric spintronics.

5.2 Introduction

Magnetoelectric materials, characterized by a strong coupling between electric polarization and magnetization, hold significant importance owing to their diverse potential applications, such as magnetic field sensors, voltage-tunable inductors, and mechanical magnetoelectric antennas. The magnetoelectric effect is usually associated with significant electronic hybridization or orbital rearrangements induced by applied electric fields. However, the magnetoelectric coupling is never purely electronic. Instead, it can be driven by structural changes and based on lattice-mediated mechanisms [48, 145, 22], in which phonons may play pivotal roles. Understanding phonon properties in magnetoelectric materials and how phonons interact with spin and electron degrees of freedom aids in developing novel magnetoelectric spintronics with desired functionalities.

The generation of phonon angular momentum by electric field was theoretically proposed in magnetic systems without inversional symmetry [146], like Cr_2O_3. Lately, the formation of magnon-polaron when the magnon and phonon dispersions cross was found in Cr_2O_3 [50], suggesting the existence of sizable spin-phonon interactions. There is great potential in engineering spin and phonon transport through these interactions, but the lack of understanding of the lattice dynamics in the context of magnetoelectric coupling hinders such efforts. Below T_N, Cr_2O_3 displays non-linear contractions along the c-axis and expansions along the a-axis [138], whereas, above T_N, both the a and c axes show linear expansion [147]. Such anomalous thermal expansion is still poorly understood. Furthermore, the Raman peak associated with the phonon mode around 300 cm^{-1} exhibits significant broadening and stiffening as temperature increases [148]. This may be associated with dynamic spin-phonon interaction, where atomic vibrations modify exchange integral and subsequently renormalize phonon energy [17, 18]. Existing work [19, 20, 21, 22, 23, 24, 25, 26] usually fits the phonon stiffening to a phenomenological model, and quantitative analysis based on first-principles calculations is scarce. The exact origin of such phonon stiffening remains elusive.

In this work, we present inelastic neutron scattering (INS) characterizations and first-principles atomistic analysis of the temperature-dependent phonon dynamics, unveiling the strong interactions between spin, electron, and lattice degrees of freedom that cause significant stiffening in longitudinal optical (LO) modes. We attribute the anomalous stiffening of these LO modes to the renormalizations of electron states due to the change of spin order and propose a static instead of a dynamic origin of such stiffening. The result shows the potential of tuning phonon energy using magnetoelectric interactions for engineering novel magnetoelectric spintronics materials.

5.3 Methods

5.3.1 INS measurements

Time-of-flight INS measurements were performed on single crystal and polycrystalline Cr_2O_3 with the Wide Angular Range Chopper Spectrometer (ARCS) at the Spallation Neutron Source (SNS). The samples were placed on an Al holder and mounted in a low-background electrical resistance vacuum furnace. Four-dimensional dynamic structure factors $S(\mathbf{Q}, E)$ were obtained at T = 50, 280, and 450 K using incident energy of 75 meV, covering multiple Brillouin zones and simultaneously measuring magnon and phonon dispersions. Data reduction was done with MANTID [67]. The data was normalized by the proton current on target and corrected for detector efficiency. The temperature-dependent S($\mathbf{Q}$,E) is given by the product of $[n(E) + 1] = 1/(1 - e^{E/k_B T})$, which corresponds to the thermal occupation of phonon at the energy-gain side and enforces the detailed balance, and the imaginary part of dynamic susceptibility χ'' ($\mathbf{Q}$,E). The lattice scattering S($\mathbf{Q}$,E) for one-coherent phonon creation process is subject to 1/E. To remove the bias introduced by these factors, one-dimensional slices of χ'' ($\mathbf{Q}$,E)E were used to obtain phonon energy at different temperatures.

For polycrystalline samples, the two-dimensional $S(|\mathbf{Q}|, E)$ were obtained at T = 50, 150, 280, 350, and 450 K using an incident energy of 100 meV. INS measurements on an empty Al can were performed at the same temperatures, and the measured intensity, as the neutron scattering background induced by the sample holder, was subtracted from the polycrystalline data.

5.3.2 First-principles calculations

The ab initio density functional theory (DFT) calculations were performed with the VASP (Vienna Ab initio Simulation Package) [69, 70] on a plane-wave basis set, using the projector augmented wave (PAW) pseudopotentials [71, 72] with local spin density approximation (LSDA) exchange-correlation functionals [73] and the Hubbard-U model [74]. U = U-J = 3.5 eV was chosen to obtain the best match with experimental phonon dispersion, although it underestimates the electron band gap. An energy cutoff of 550 eV was used for all calculations. GGA+U ionic relaxation was done based on a primitive cell containing 4 chromium and 6 oxygen atoms with collinear antiferromagnetic (AFM) spin order. A Gamma-centered k-point grid of 11×11×11 was used in GGA+U ionic relaxation. The relaxed rhombohedral cell (space group 167) with a lattice constant of 5.46 Åand an angle of 55.25° was used in phonon dispersion calculations. This corresponds to a = 5.06 Åand c = 13.83 Åin a conventional hexagonal cell. The relaxed lattice parameters were slightly overestimated compared to the literature values, a = 4.95 Åand c = 13.57 Å, determined by diffraction experiments [149]. The static dielectric tensor and Born effective charges were obtained to calculate non-analytical terms in phonon calculations. The second-order interatomic force constants were obtained from a 2×2×2 supercell of 80 atoms with a Monkhorst-Pack k-point grid of 5×5×5 using the density functional perturbation theory (DFPT). Phonon eigenvalues and eigenvectors were obtained by diagonalizing the dynamical matrix as implemented in the Phonopy [52]. The calculated phonon energies were scaled by multiplying a factor of 1.06 to compensate for the overestimated lattice constants. Phonon density of states were calculated based on a 20×20×20 k-point mesh using Phonopy. The obtained phonon density of states were weighted by the coherent neutron scattering cross section and convoluted with INS energy resolution function to compare with experiment data directly. Atomic thermal displacements as a function of temperature were calculated from the number of phonon excitations using the same k-point mesh, as implemented in the Phonopy.

Phonon dispersion calculations based on quasi-harmonic approximation (QHA) were performed to estimate phonon energy change induced by lattice thermal expansions. The collinear AFM spin order was applied to all QHA calculations. The QHA calculations were based on the measured thermal expansion at 50, 150, 280, 350, and 450 K. Specifically, the LSDA+U relaxed lattice constant was used as the value at 0 K, and the lattice constants at other temperatures were determined by thermal expansion measurements from Ref. [138, 147], as illustrated in Section 5.8 Figure 5.6. The static dielectric tensor and Born effective charges were obtained separately for all cells. Phonon dispersions were calculated using the same procedures.

Static electron densities with FM and AFM spin arrangements were evaluated using the same cell from ionic relaxation with AFM spin order and a Gamma-centered k-point grid of 11×11×11. The electron density difference, $n(AFM) - n(FM)$, was visualized using VESTA [149].

Two sets of phonon dispersions with collinear ferromagnetic (FM) spin order were calculated based on the same relaxed cell mentioned forehead and another cell relaxed under

FM spin arrangements. The second-order force constants, static dielectric tensor, and Born effective charges were obtained using the same procedures. To calculate frozen phonon potential associated with LO2, LO3, and LO4 modes under different spin configurations, GGA+U calculations were performed with atoms in the supercell displaced according to the eigenvectors of these modes at the zone center. Atomic displacements were set to be smaller than 0.16 Å, which is sufficiently large compared to the calculated thermal displacement at 550 K (0.07 Åfor Cr^{3+} and 0.08 Åfor O^{2-}). Frozen phonon potentials with collinear ferromagnetic (FM) and antiferromagnetic (AFM) spin orders were calculated using a Gamma-centered k-point grid of 13×13×13.

5.4 Stiffening of ALO modes

The striking result of our investigation is the observation of significant energy stiffening of the LO phonon modes at 35~55 meV on heating. The stiffening is anomalous because phonons are commonly expected to soften with temperature due to thermal expansion and phonon anharmonicity [1]. For reference, we named these phonon modes anomalous longitudinal optical (ALO) modes, which refer to the LO2 + LO3 modes (see Figure 5.2 (a) for the mode assignments). In Figure 5.1 (b-d), the experimental scattering structure factor $S(\mathbf{Q}, E)$ shows clear phonon dispersions. At 50 K, the calculated scattering cross section of coherent one phonon creation $S_{coherent+1}(\mathbf{Q}, E)$ (see SI Note.1) is in excellent agreement of scattering intensity with the measured data (Figure 5.1 (a-b)). For phonon energy, our calculations match well with the measured data at 50 K, except for the ALO mode. This can be seen by comparing Figure 5.1 (a) to (d), where the "Λ" shaped

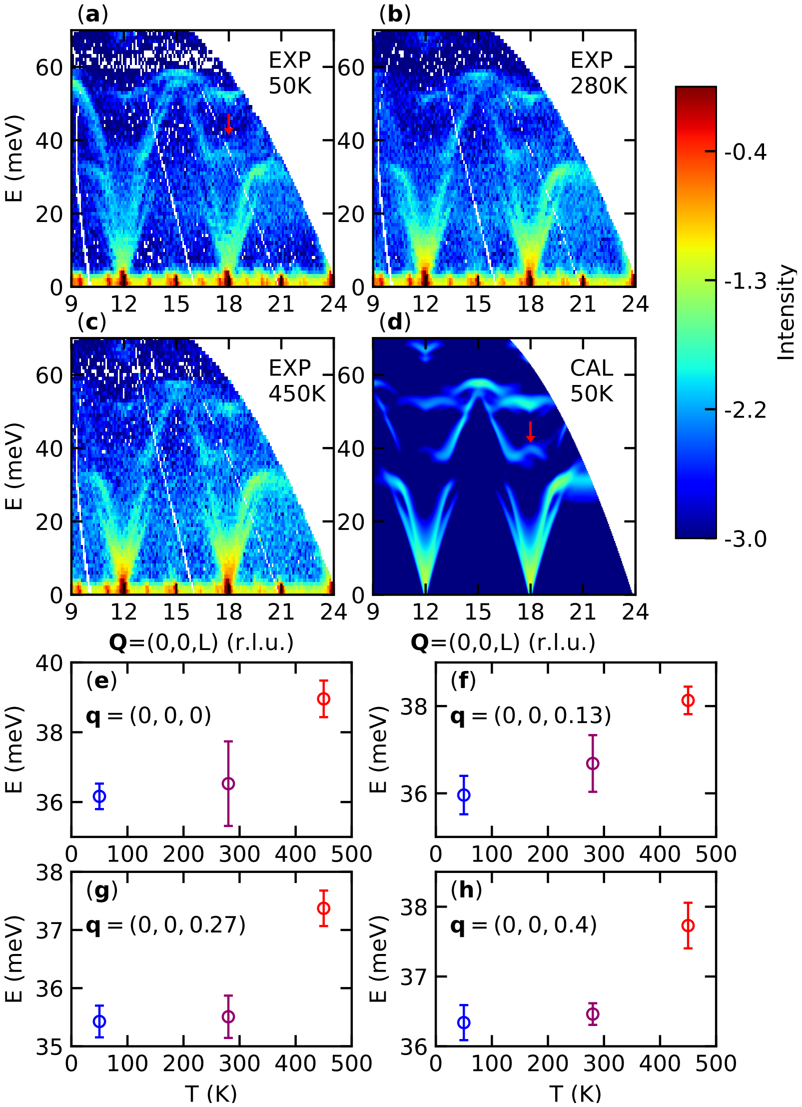

Figure 5.1: (a, b, c) The dynamic structure factor of Cr¬2O3 measured by INS on ARCS, SNS at 50, 280, and 450 K along the [0,0,L] direction in the reciprocal space. The intensity is integrated over ±0.2 (r.l.u) along perpendicular axes and scaled by multiplying E. (d) Simulation of lattice scattering S(**Q**,E) at 50 K with the same Q integration ranges and instrument resolution function. The calculated $S_{coherent+1}(\mathbf{Q}, E)$ is cropped by the neutron scattering kinetic limits. Both experimental data and theoretical calculations are plotted on a logarithmic scale. (e-h) Temperature-dependent energies of LO2 modes from Gaussian fittings of the measured constant-**Q** slices.

dispersion at L=15 r.l.u. with an energy range of 35-55 meV has much higher tails in the $S_{coherent+1}(\mathbf{Q}, E)$ than experimental $S(\mathbf{Q}, E)$ at 50 K (denoted by red arrows). In Figure 5.1 (c, d), the agreement becomes better between $S_{coherent+1}(\mathbf{Q}, E)$ and experimental $S(\mathbf{Q}, E)$ at 450 K, indicating the ALO modes significantly stiffen on heating.

To analyze temperature-dependent phonon dynamics of LO2 modes, constant-**Q** slices were taken at $\mathbf{Q}$ = (0,0,L) with L = 18, 17.6, 17.2, and 16.8 r.l.u., which correspond to phonon wave vectors **q** at 0.0, 0.13, 0.27 and 0.4 in reduced wave vector units along Γ-Z. For these points, the intensities near 36 meV corresponding to the LO2 modes have significant blueshifts on heating, as shown in Section 5.8 Figure 5.5 (b-e). Phonon energies were extracted from the Gaussian fittings of the constant-**Q** slices. In Figure 5.1 (e-h), the LO2 modes show 1.5 2.9 meV increases in energy from 50 to 450 K. Importantly, the increase of LO2 energies from 50 to 280 K is much less than that from 280 to 450 K, suggesting its relation with the change of spin order. As shown in Figure 5.1 (b), the LO3 modes are closely parallel with magnons at 50 K, which have sizable INS intensities at $13.5 < L < 15$ r.l.u.. The calculated magnon intensities (see SI note 2) show great agreement with the measured S(**Q**,E), as presented in Fig. S1 (a). The q-dependence of LO3 modes at fixed energies was extracted from constant-E slices, which were obtained by subtracting magnon intensity and folding with respect to L = 15 r.l.u. (shown in Section 5.8 Figure 5.5 (b1-b6)). In Figure 5.2 (a), clear left shifts indicate that LO3 modes stiffen on heating.

In the Raman work on single crystal Cr_2O_3 by Dwij et al. [148], the mode around 290 cm^{-1} (36 meV) changes dramatically on heating. The mode emerges at 290 cm^{-1} at 85 K, broadens and stiffens between 160 and 260 K, and finally narrows and stabilizes above

300 K at 302 cm^{-1}. The measured Raman frequencies and the trend of Raman linewidths are consistent with our results for the zone center LO2 mode. In their interpretation, the Raman modes below 160 K and above 300 K correspond to two separate phonon modes and are suggestive of lattice symmetry changes by the change of spin order. They assign the mode above 300 K to E1g, which are the doubly degenerate TO2 modes shown in Figure 5.2 (a). Their "two modes" explanation contradicts the Raman intensity calculations by T. Larbi et al. [150]. In both AFM phase (space group 161, R3C, when treating Cr^{3+} with different spin directions separately) and PM (FM) phase (space group 167, $R\overline{3}C$), the mode LO2 ($\mathrm{A}_1/\mathrm{A}_{1g}$) are Raman active. In the FM (PM) phase, the A_{1g} (LO2) mode has nearly ten times of Raman intensity than that of E_{1g} mode. This suggests the observed Raman mode by Dwij et al. should be LO2 above 300 K. More importantly, our INS data along [0,0,L] direction only show prominent intensity from LO2 mode, and nearby transverse modes have minimal intensity. This is because the phonon eigenvectors of LO2 (nearby transverse modes) are parallel (perpendicular) to the $\mathbf{Q}$, which makes $|\mathbf{Q} \cdot \mathbf{e}| \gg 0$ (=0), leading to prominent (zero) scattering cross sections (see Section 1.3.1). This is shown by the calculated $\chi''_{coherent+1}(\mathbf{Q}$,E)E in Section 5.8 Figure 5.4 (a), where the transverse modes near 35 meV show much lower intensity compared to the LO2 mode near 38 meV. In Section 5.8 Figure 5.4 (b-e), $\chi''_{coherent+1}(\mathbf{Q}$,E)E show good agreements with the experimental data at 450 K, proving their reliability. The non-zero intensity for these transverse modes is a result of the instrument resolution in the reciprocal space. In summary, the intensities around 38 meV originate from LO2 modes at all temperatures, contrary to the previously suggested local symmetry change.

Interestingly, only ALO modes stiffen, while other longitudinal optical phonon modes below 60 meV soften with temperature. From 50 to 450 K, the LO4 and LO5 modes show 2.5% and 1.1% softening on average, as shown in Figure 5.2 (a). The measured phonon density of states (DOS) were obtained by integrating intensities at $5 < |\mathbf{Q}| < 9$ Å^{-1} with multi-phonon and thermal occupation corrections using GETDOS [102]. Figure 5.2 (b) shows the calculated phonon DOS (see SI Note.1), which agrees well with the measured phonon DOS. By fitting all prominent DOS peaks to Lorentzian functions, the temperature dependencies of these peak positions are shown in Figure 5.2 (c). Clearly, most phonon modes soften from 50 to 450 K.

Phonon energies were evaluated with quasi-harmonic approximation (QHA) using the lattice structure obtained from ionic relaxation together with thermal expansion ratios from the literature [138, 147] shown in Section 5.8 Figure 5.6 (a) (see SI Note.1 for details). Experimental and calculational phonon isobaric Grüneisen parameters were evaluated at 50 and 450 K,

$$\gamma = -\frac{V}{\omega}(\frac{\partial \omega}{\partial V})|_P = -\frac{V(50K)(\omega(450K) - \omega(50K))}{\omega(50K)(V(450K) - V(50K))},$$

where V and ω are the volume of a unit cell and phonon energy. The temperature-dependent volumes $V(T)$ were obtained by segmentally fitting thermal expansion data from literature [138, 147], as shown in Section 5.8 Figure 5.6 (b).

Except for the ALO modes, most phonons soften at elevated temperatures as expected due to thermal expansion and phonon-phonon interactions. This behavior is illustrated in Figure 5.2 (e), where the calculated γ_{exp} are positive for all modes and reasonably match the average $\overline{\gamma}_{cal}$ values. For LO4 and LO5 modes, the average softening computed

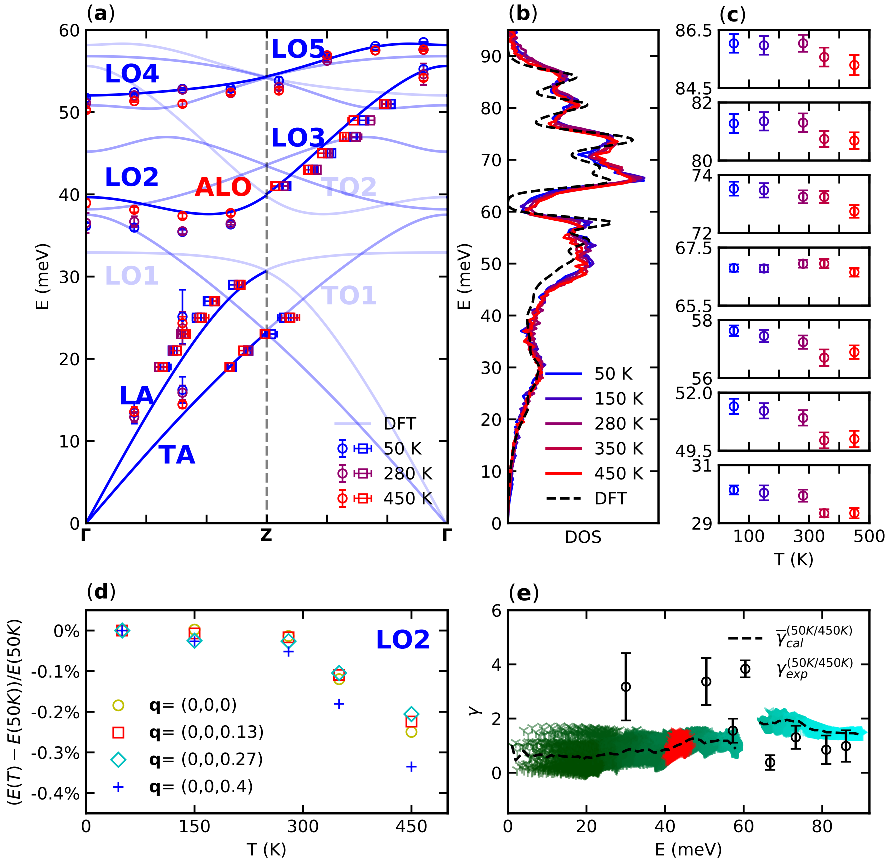

Figure 5.2: (a) Colored circles (squares) show phonon energies at 50, 280, and 450 K from Gaussian fittings of the measured constant-**Q** (constant-E) slices. Blue lines show the calculated phonon dispersions. Phonon modes are labeled according to their eigenvectors. Phonon branches that contribute to the scattering intensity are shown by deep blue lines. (b) Measured phonon DOS at 50, 150, 280, 350, and 450 K. The calculated neutron-weighted phonon DOS was shown by black dashed lines. (c) Temperature dependence of phonon energies extracted from Lorentzian fittings of the measured polycrystalline data. (d) Wave vector and temperature-dependent normalized LO2 energies predicted by quasi-harmonic phonon model. (e) Experimental (black circles) and Calculational (colored markers) phonon Grüneisen parameters γ. Experimental γ was obtained using phonon energies at 50 and 450 K with experimental thermal expansions. The colored markers denote γ for different phonon branches, and the red markers show the γ for LO2 and LO3 modes. The Black dashed line represents E-dependent averaged Grüneisen parameters $\overline{\gamma}$. Error bars represent or correlate to fitting uncertainties.

with QHA is around 0.8%~0.9% from 50 to 450 K (see Section 5.8 Figure 5.7 (b-c)) and shows a satisfactory agreement with the experimental values. Furthermore, the softening of an optical mode around 613 cm^{-1} shows an example of anharmonic behavior and can be accurately described using a model for three-phonon processes [148].

Evidently, the stiffening observed for ALO modes cannot be attributed to these effects. As shown in Figure 5.2 (e), the γ_{cal} for ALO modes are positive, indicating softening of these modes is expected with thermal expansion. The calculated LO2 and LO3 mode energies from QHA at various q-points show 0.2%~0.4% (Figure 5.2 (d)) and 0.7%~0.9% (Section 5.8 Figure 5.7 (a)) softening. These clearly contradict the observed stiffening. The stiffening of these modes is likely not the result of electron-phonon interactions due to the electron band gap of 3.37 eV [139]. Instead, the sudden changes of LO2 energies occur between 280 and 450 K, spanning the T_N, and suggest the correlation with the spin order in the system.

5.5 Effect of magnetoelectric coupling on lattice dynamics

The stiffening of the ALO modes and the non-linear anisotropic thermal expansion mainly originate from electron density redistributions by the change of spin order. Frozen phonon potential (FPP) curves were obtained with AFM and ferromagnetic (FM) spin configurations (see SI Note.1). Here, the collinear FM spin arrangement was used to illustrate the effects of the deviation of spin states from the AFM phase. FFP calculations reveal a prominent shift in the energy minimum for the LO2 mode upon transitioning from AFM to FM, indicating a preference for shorter interatomic distances between adjacent Cr^{3+} ions

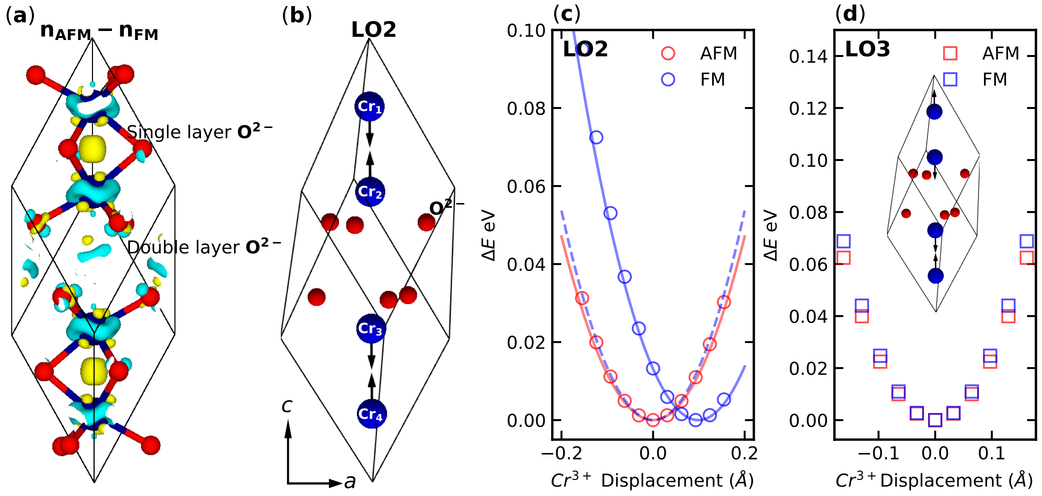

Figure 5.3: (a) Isosurfaces of electron density difference based between AFM and FM spin configurations. Blue and red spheres represent Cr^{3+} and O^{2-} atoms. The isosurfaces represent either positive (yellow) or negative (light blue) density difference enclosed. (b) Displacement patterns of LO2 phonon mode at zone center. (c-d) Frozen phonon potentials for LO2 (circles) and LO3 (squares) modes at zone center with AFM (red) and FM (blue) spin configurations. In panel (c), solid lines show quadratic fitting for AFM (red) and FM (blue) frozen phonon curves. The dashed line represents the fitting result for the FM frozen phonon curve with the same energy minimum as the AFM curve. The inset in (d) shows phonon displacement patterns corresponding to LO3 eigenvectors.

(Cr_1-Cr_2 and Cr_3-Cr_4) in the FM state (Figure 5.3 (c)). By mapping the electron density difference between AFM and FM (see SI Note.1), n_{AFM}-n_{FM}, one can infer that the shift originates from the sudden decreases of electron density between these adjacent Cr^{3+} atoms, as shown in Figure 5.3 (a). Such reductions in electron density change Cr-O bond lengths and angles, consequently decreasing the separation between neighboring Cr^{3+} atoms, thus shortening the lattice constant along the c-axis. Simultaneously, the electron density in the ab plane around Cr^{3+} atoms increases from AFM to FM, potentially leading to expansions of the ab-axes. These are consistent with non-linear contractions along c and expansions along a measured by diffraction below T_N [138]. The lattice deformation, induced by spin order change, should be subject to the sublattice magnetization, which can be well approximated by the Brillouin function B(T) for S=3/2 in the mean-field theory [144]. As shown in Section 5.8 Figure 5.6 (a), the temperature dependence of a and c lattice constants matches well with the B(T) below T_N, supporting the proposed magnetic origin. Above T_N, the observed linear thermal expansion along a and c directions [147] is anticipated: at sufficiently high temperatures, where the entropy of the spin system saturates and the magnetic moments become mostly disordered, one may expect non-linear lattice expansion to vanish and the a and c axes to expand linearly due to lattice anharmonicity.

The motions of ALO modes change the distances between the nearest Cr^{3+} pairs along c and are particularly sensitive to the aforementioned electron redistributions. As shown in Figure 5.3 (b), the zone center LO2 mode corresponds to identical motions along the c-axis for both atoms in all Cr^{3+} pairs. In contrast, for the LO3 mode at Γ point, Cr_1-Cr_2 and Cr_3-Cr_4 pairs are in opposite phases, and the FFPs are always symmetric with respect to u, the Cr^{3+} displacements, and independent of equilibrium Cr-Cr distances. In Figure 5.3 (c-d), the calculated FPPs of FM configuration are steeper than that from AFM for both LO2 and LO3 modes. The second-order force constants, $\partial^2 E_{LO2}/\partial u_{Cr}^2$ and $\partial^2 E_{LO3}/\partial u_{Cr}^2$, determined through quadratic fittings of the FPPs with $|u_{Cr}| < 0.07$ Å(corresponding to mean atomic displacement at 550 K) are larger for the FM phase than the AFM phase by a factor of 1.14 and 1.10 for LO2 and LO3 modes, respectively. This indicates that the phonon energies of ALO are stiffened by the redistributions of electron density. On the contrary, the FFPs for LO4 are softer in the FM phase than in the AFM phase (Section 5.8 Figure 5.8 (a)), consistent with our INS data. Although the LA modes also involve vibrations of Cr^{3+} along the c-axis, they show a normal softening with temperature (Figure

5.2 (a)). This is because they do not change the Cr-Cr distances much, and the electron density change between Cr-Cr shows little effect on their phonon energy. It is important to emphasize that the stiffening of ALO modes is purely magnetoelectric and is exclusively driven by the change of spin order. This is supported by the result that the QHA model does not reproduce the stiffening even when c-axis contraction is considered. Moreover, the result is also supported by the observed phonon broadening in our data and prior Raman work [148] near T_N, where the long-range spin order is mostly lost while the short-range spin order is preserved. The broadening of phonon peaks is likely due to the second-order nature of the magnetic transition and a non-homogeneous distribution of electron density.

Compared with the PM state in the real system, FPPs based on FM overestimate the shortening in the Cr-Cr distance along the c-axis. The calculated reduction in the Cr-Cr distance is ~ 0.1 Å, significantly larger than the reported literature value of ~ 0.03 Åspanning from 2 K to 315 K [138]. This leads to the higher calculated phonon energy in the FM state than our data for both LO2 and LO3 modes, as depicted in Section 5.8 Figure 5.8 (c). This is expected because, in the PM state, the changes in electron densities are more moderate. Nevertheless, we believe this comparison provides insights into electron density renormalizations induced by spin order change. Quantitative evaluations of phonon energy in the PM state may be done using the spin state averaged (SSA) model [151], self-consistent ab initio lattice dynamical (SCAILD) calculations [152], or thermodynamic formulations [153]. These are beyond the scope of the current work.

5.6 Dynamic spin-phonon interactions

The stiffening of ALO modes is not likely the result of other forms of spin-phonon interactions, such as magnetostriction or dynamic spin-phonon interaction (DSPI). In magnetostriction, as magnetic order switches, the spin exchange energy can modify the interatomic potential between bonded ions, subsequently leading to alterations in atomic distances and affecting phonon energies. However, the literature values of the Cr^{3+} position change are around 1.5 picometers from 284 to 315 K across T_N [138], and they are too small to result in the observed stiffening.

Another mechanism is the DSPI, for which the lattice vibrations impact the exchange integral, consequently influencing the orbital overlap between the ions and altering the phonon energies [17, 18]. This interaction is purely dynamic and different from our proposed origin. The phonon energy shifts due to DSPI are subject to the quadratic term of the Taylor expansion of exchange constants J_{ij} in a Heisenberg model, $H = -\sum_{i,j} J_{ij}\langle S_i \cdot S_j\rangle$, with respect to the lattice displacement vector $\hat{u}_k^{\alpha}$ for α^{th} phonon branch, where k denotes the atoms involved in the displacement. The phonon energy shift due to DSPI can be written as $\Delta\omega_{DSPI}(T) = \omega(T) - \omega_0(T_0) = -\dfrac{N}{2\mu_\alpha\omega_\alpha}\sum_{i,j}\langle S_i \cdot S_j\rangle[\hat{u}_k^{\alpha}(t)\cdot\nabla k]^2 J_{ij}$, where T_0 is a reference temperature above T_N, N is the number of Cr^{3+} atoms, μ_α is the reduced mass for atoms that participating in the vibration and ω_α is the phonon energy [18]. This method and a simplified version $\Delta\omega_{DSPI}(T) = \lambda_{sp}\langle S_i \cdot S_j\rangle$ (λ_{sp} is the spin-phonon coupling constant) are extensively used for modeling the phonon energy shifts due to DSPI in transition-metal compounds [19, 20, 21, 22, 23, 24, 25, 26]. By neglecting the change of S_i under atomic displacements and within the mean-field approximation, the spin correlation function $\langle S_i \cdot S_j\rangle$

can be expressed by $\langle S_i \cdot S_j \rangle = S^2(M_{Cr}(T)/3\mu_B)^2 \approx S^2B(T)^2$, where $M_{Cr}(T)/3\mu_B$ is the normalized Cr^{3+} sublattice magnetization. For simplicity, we consider only one pair of the nearest neighbor exchange coupling, J_{NN}, between the closest Cr^{3+} atoms. For the LO2 mode at zone center with only two Cr^{3+} displacements involved, the $\Delta\omega_{DSPI}$ may be written as $\Delta\omega_{DSPI}(T) \approx -\frac{2}{m_{Cr}\omega_{LO2}}\frac{\partial^2 J_{NN}}{\partial u^2_{Cr,LO2}}S^2B(T)^2$. The second-order derivatives $\partial^2 J_{NN}/\partial u^2_{Cr,LO2} = \partial^2(E(AFM) - E(FM))/4S^2\partial u^2_{Cr,LO2}$ were evaluated by quadratic fittings, and we obtained $\partial^2 J_{NN}/\partial u^2_{Cr,LO2} = -0.018$ eV/ Å^2 and $\partial^2 J_{NN}/\partial u^2_{Cr,LO3} = -0.027$ eV/ Å^2. These are much smaller than the value obtained from fitting experimental results for the Raman mode near 604 cm^{-1} in $LaMnO_3$, $\partial^2 J_{NN}/\partial u^2_{O,RM} = +0.218$ eV/ Å^2, which corresponds to ~1 meV energy stiffening from 0 K to the magnetic transition temperature [18]. For Cr_2O_3, the calculated $\Delta\omega_{DSPI}$ (50K) for the zone center LO2 mode is around + 0.04 meV, and is negligible comparing with the observed $\Delta\omega(50K)|_{T_0=450K} = -2.9$ meV. Notably, the LO2 and LO3 modes at the zone center are expected to soften by DSPI and are opposite to our observation.

5.7 Summary

In summary, the stiffening of ALO modes does not originate from DSPI. To our knowledge, the spin-phonon coupling constants $(\frac{\partial^2 J}{\partial u^2})$ are always obtained by fitting the experimental phonon energy shifts, and quantitative evaluations by first-principles calculations are scarce. We speculate that the proposed static origin may dominate phonon energy shifts in many magnetoelectric-coupled systems and suggest that such effects need revisiting using quantitative modeling. Moreover, this study illuminates the magnetoelectric origin of non-linear thermal expansion below T_N, challenges the previously proposed phonon symmetry change, highlights an unusual phonon energy stiffening driven by magnetoelectric coupling, and sheds light on controlling lattice dynamics in novel magnetoelectric spintronics.

5.8 Supplementary information

5.8.1 Supplementary figures

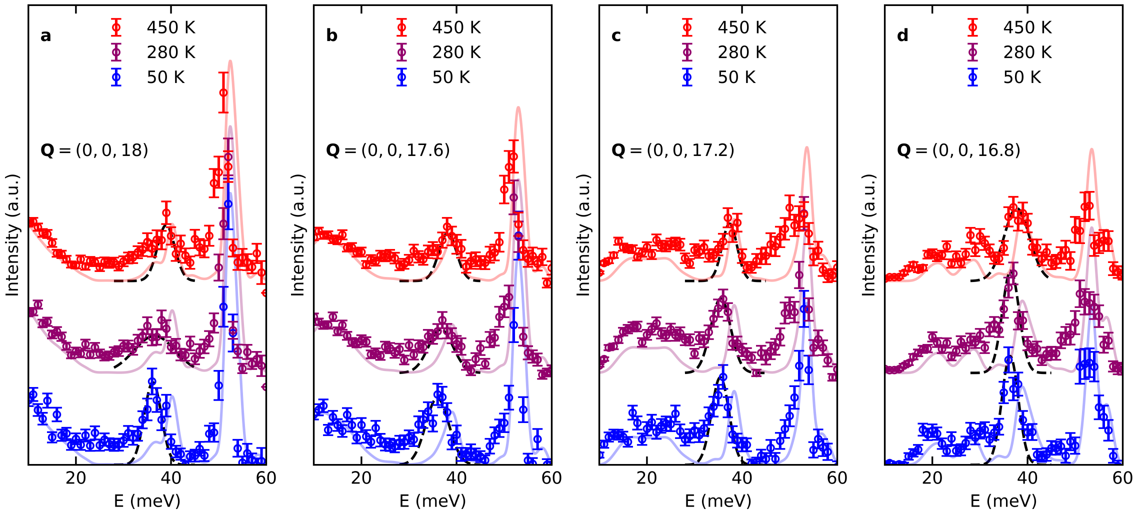

Figure 5.4: (a-d) Constant-Q slices of the measured imaginary part of dynamic susceptibility χ'' (Q,E)E at 50, 280, and 450 K were obtained by integrating ±0.2 (r.l.u) along perpendicular axes and are shown by the colored circles. Lighter colored lines represent calculated phonon $\chi''_{coherent+1}$(Q,E)E with the same integration range and temperature. Error bars indicate data uncertainties. The Black dashed line shows the results of the fittings.

To analyze temperature-dependent phonon dynamics of LO2 modes, constant-Q slices were taken at Q = (0,0,L) with L = 18, 17.6, 17.2, and 16.8 r.l.u., which correspond to phonon wave vectors q at 0.0, 0.13, 0.27 and 0.4 in reduced wave vector units along Γ-Z. For these points, the intensities near 36 meV corresponding to the LO2 modes have significant blueshifts on heating, as shown in Figure 5.4 (a-d). Temperature-dependent energies of LO2 modes from Gaussian fittings of the measured constant-Q slices are shown in Figure 5.1 (e-h).

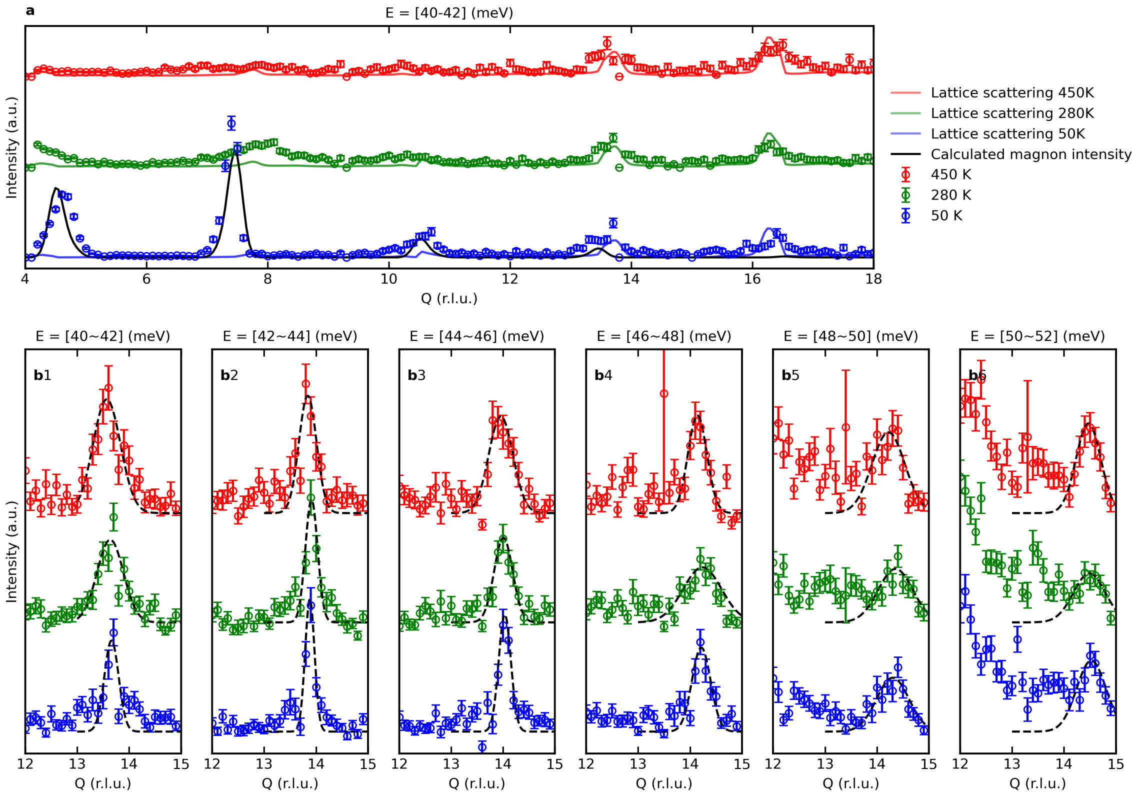

Figure 5.5: (a) Comparison of experimental and calculational scattering intensities. The dots represent constant E slice S(Q) obtained from integrating 40 to 42 meV at 50 K (blue), 280 K (green), and 450 K (red). Colored (black) lines show calculated lattice (magnetic) scattering S(Q) obtained in the same way. (b1-b6) Colored dots show the S(Q) at 50, 280, and 450 K with different energy integration ranges. The S(Q) is obtained by folding $12 < Q < 18$ (r.l.u.) with respect to Q = 15 (r.l.u.). Magnetic scattering intensity has been removed from the S(Q) at 50 K. The black dashed lines show the Lorentzian fitting.

As shown in Figure 5.1 (b), the LO3 modes are closely parallel with magnons at 50 K, which have sizable INS intensities at $13.5 < L < 15$ r.l.u.. The calculated magnon intensities (see Section 1.3.2) show great agreement with the measured S(Q,E), as presented in Figure 5.5 (a). To remove the magnetic scattering intensities from one-dimensional S(Q), atomistic simulations were performed to estimate the intensity from both lattice (S_{lat}(Q)) and magnetic (S_{mag}(Q)) scattering (see Section 1.3.2 and 1.3.1). In Figure 5.5

(a), great consistencies can be seen when comparing the calculated and measured S(Q) for both magnetic and lattice scattering at 41 meV. The measured S(Q) at $12 < L < 18$ (r.l.u.) is symmetric with respect to L = 15 (r.l.u.). The S(Q) shown in Figure 5.5 (b1-b6) were folded to improve statistics, and the magnetic scattering intensities were subtracted based on the calculated S_{mag}(Q). Clearly, as the temperature increases, the peak centers shift to lower Q, indicating stiffening of phonon energies.

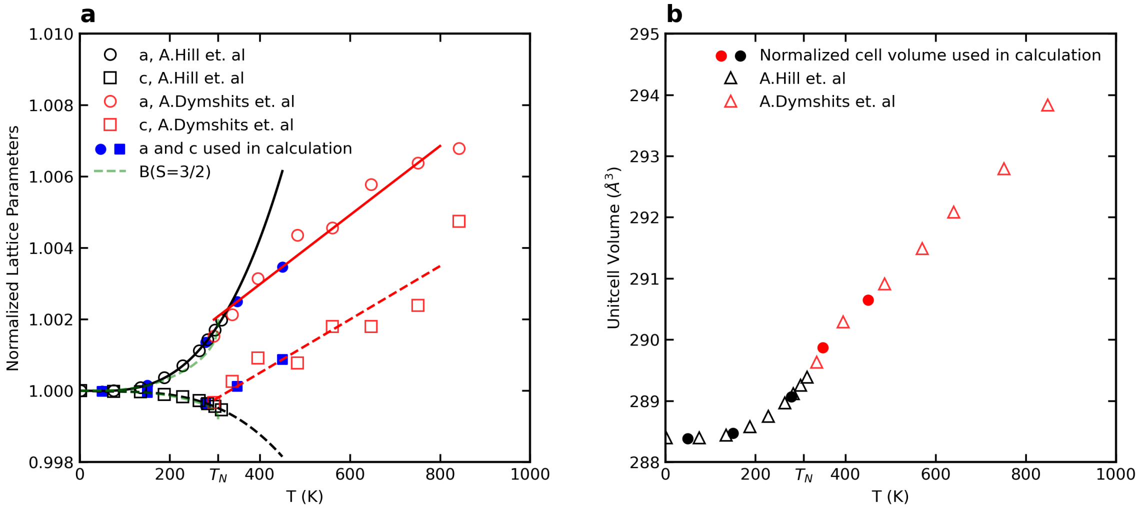

Figure 5.6: (a) Temperature-dependent normalized lattice parameters from 2 to 842 K from diffraction experiments [138, 147]. Empty circles and squares respectively represent lattice constants a and c in the conventional hexagonal cell below (black) and above (red) T_N. Blue solid dots and squares show the lattice constants that are used in the QHA calculations. The green dashed lines show the rescaled Brillouin function for S=3/2. (b) Temperature-dependent volumes from 2 to 842 K are shown in empty triangles below (black) and above (red) T_N. Solid dots represent normalized unit cell volumes used in the QHA calculation.

The temperature-dependent normalized lattice parameter ratios $a(T)/a(2K)$ and $c(T)/c(2K)$ are shown in Figure 5.6 (a), and temperature-dependent volumes are shown in Figure 5.6 (b). The temperature dependences of both lattice constants and cell volumes are nonlinear below T_N and linear above T_N. The data below T_N were fitted using a third-order polynomial, and above T_N were fitted using a linear relation. The unit cells used in the QHA calculations were obtained segmentally based on the fitting results (see Methods). The Brillouin functions of S=3/2 are rescaled with -0.002 and 0.0008, showing great agreement with the nonlinearity of the experimental lattice constants a and c below T_N, respectively. This suggests that the variations in the lattice constants are subject to the change of spin order.

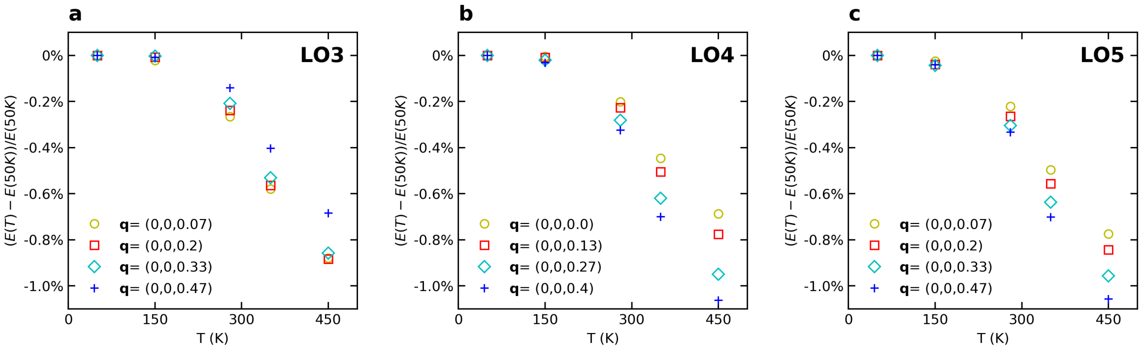

Figure 5.7: (a-c) Wave vector and temperature-dependent normalized LO3, LO4, and LO5 energies predicted by the QHA model.

As shown in Figure 5.7 (a), the LO3 phonon modes show a 0.7% 0.9% softening at elevated temperatures, contradicting our measured data. This indicates that thermal expansion cannot explain the stiffening of LO3 modes. On the other hand, the LO4 and LO5 modes show softening around 0.9%. These present a reasonable agreement with the measured temperature dependence and suggest that the softening of these modes can be partially attributed to thermal expansion.

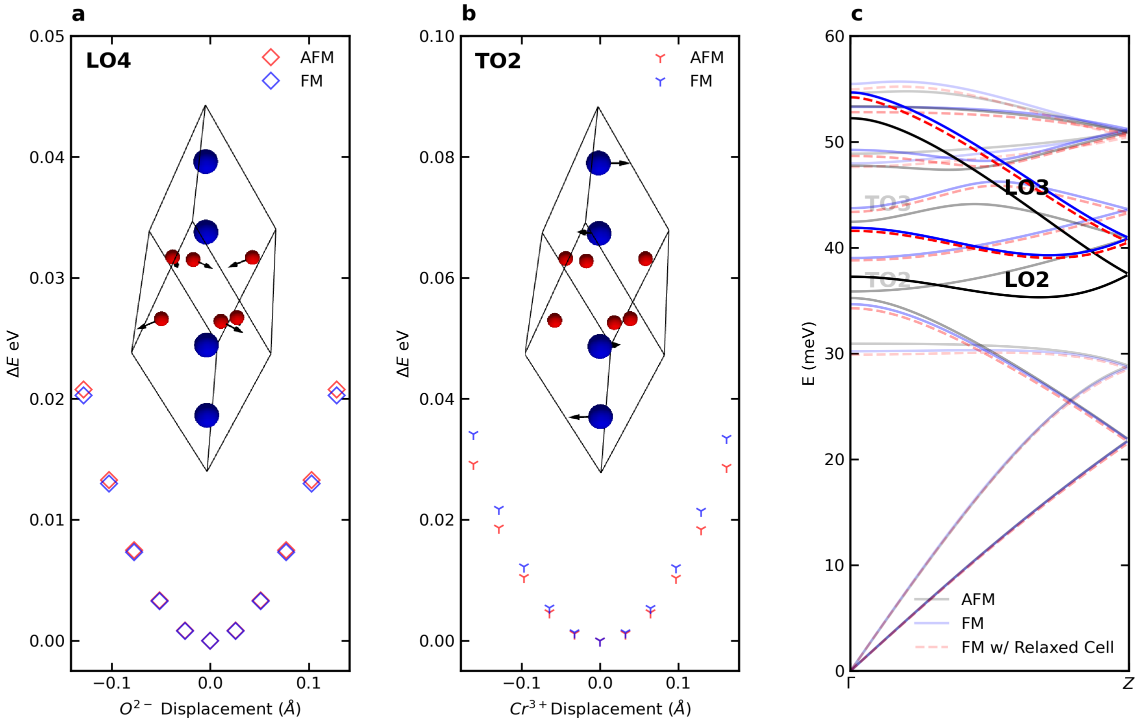

Figure 5.8: (a,b) Frozen phonon potentials for LO4 modes (diamonds) and TO2 modes (y-markers) at zone center with AFM (red) and FM (blue) spin configurations. The inset shows the mode displacement pattern. (c) Phonon dispersions based on AFM (black lines) and FM spin configurations. The phonon dispersions with FM spin order were calculated based on the unit cell obtained from AFM (blue lines) and FM (red dashed lines) ionic relaxation.

In Figure 5.8 (a), LO4 modes mainly involve motions of O atoms, and the displacements of Cr^{3+} atoms are small. The FFPs for FM are softer than those for the AFM spin arrangement, explaining the absence of stiffening of LO4 modes in our data. This is because the Cr^{3+} atoms are nearly fixed. The electron density change between the nearest Cr^{3+} pairs shows little effect on the force constants. On the other hand, the TO2 modes involve shearing motions of Cr^{3+} atoms that alternate the nearest Cr^{3+} bond lengths (Figure 5.8 (b)). Two sets of phonon dispersions with FM spin order were calculated based on the unit cell obtained from AFM and FM ionic relaxation (see Method) and showed little difference. In Figure 5.8 (c), other than the LO2 and LO3 modes, the TO2 and TO3 modes also show significant stiffening when changing to the FM spin order. The LO2, LO3, and doubly degenerate TO2 and TO3 change the distance between the nearest Cr-Cr distances, thereby stiffening due to the magnetoelectric coupling discussed in the main text.

Chapter 6

Conclusions

The thesis explored four key aspects of the research field focused on the spin and lattice dynamics, and spin-phonon interactions. Inelastic neutron scattering experiments provide direct measurements of temperature-dependent acoustic phonon dynamics, including the phonon energy and the phonon polarization, which has not been extensively studied in the presence of spin-phonon coupling. In chapter 2, we present neutron scattering signatures of mutual driving interactions through strong spin-lattice coupling and acoustic phonon eigenvector renormalization in NiO. Specifically, we performed inelastic neutron scattering experiments and atomistic simulations, revealing the spin-phonon mutual driving effect and acoustic phonon eigenvector renormalization in NiO. The spin-phonon driving effect is suggested by a modified magneto-vibrational scattering cross-section, which successfully explains the anomalous scattering intensity of acoustic phonon observed in low-order Brillouin zones. Moreover, the phonon eigenvector renormalization, suggested by strong "forbidden" intensity in high-order Brillouin zones, is also observed and attributed to the spin-driven modulation of phonon polarizations. To our knowledge, the results presented in the thesis unveil the existence of acoustic phonon eigenvector renormalization induced by spin-phonon coupling for the first time and will encourage further theoretical investigations into this important phenomenon. Our observations and analysis also provide a new approach to identifying strong spin-phonon interactions and illumining engineering functional antiferromagnetic spintronic materials through these interactions.

Thermal transport in magnetic insulators is one of the fundamental questions in developing novel spintronics and spin-caloritronic devices. Although extensive studies have been conducted on NiO, the roles of magnon and spin-phonon interactions on thermal transport are still poorly understood. This is mainly due to the inconsistency of previous thermal conductivity measurements and the negligible response of thermal conductivity under an external magnetic field. In chapter 3, we reported inelastic neutron scattering characterization of magnon and phonon dynamics, time-domain thermal reflectance measurements on temperature-dependent thermal conductivity, and atomistic simulations of the phonon and magnon transport in NiO. We found that the thermal conductivity is dominated by phonon transport and is subject to spin-phonon interactions above 100 K. Contrary to previous steady-state measurements, our measured thermal conductivity shows a stronger temperature dependence below the Néel transition and a weaker temperature dependence in the paramagnetic phase. We attributed the effects to magnon-phonon scattering and spin-induced dynamic symmetry breaking in the phonon system in the antiferromagnetic phase. We provide a detailed experimental-theoretical study of thermal transport in this important material and highlight the crucial role of spin-phonon interactions in lattice thermal transport in magnetic materials.

Chromia (Cr_2O_3), the inaugural magnetoelectric material and an emerging candidate for spintronics and magnetoelectric applications, is an interesting model material for understanding temperature-dependent spin dynamics. Despite extensive research into the spin dynamics in this system, the experimental characterization and theoretical prediction of the temperature-dependent dynamics of magnons, as well as paramagnons, remain lacking. In chapter 4, our study delves into these issues through a comprehensive experimental-theoretical analysis of the spin dynamics of Cr_2O_3. Our results present direct observations of paramagnons not only above T_N, but also closely below T_N in Cr_2O_3 for the first time. The observation of paramagnons below the ordering temperature is particularly notable, as it challenges the traditional view that paramagnons should only exist in the paramagnetic state above the transition temperature. This suggests that the transition to long-range magnetic order is not a sharp, abrupt transition but a more gradual process where short-range order coexists with long-range order near the critical point. Furthermore, our results provide detailed experimental characterizations and theoretical quantifications of temperature-dependent magnon energy. We found that magnon energy softening primarily originated from four-magnon interactions, while thermal expansion played a minor role. Our results unveil the interplay between short-range and long-range magnetic correlations in strongly correlated electron systems and provide insights into controlling the spin dynamics of Cr_2O_3 for functional spintronics and magnetoelectronic applications.

Despite extensive exploration of lattice dynamics in Cr_2O_3, the origins of nonlinear thermal expansions in its antiferromagnetic phase and stiffening of optical phonons are still elusive. In chapter 5, our study investigates these issues through a comprehensive experimental-theoretical analysis of lattice dynamics of Cr_2O_3. Our results reveal a common static magnetoelectric origin for both phenomena: the alteration of spin order prompts the renormalization of electrons between the nearest Cr-Cr pairs, inducing non-linear thermal expansion below the T_N and energy shifts of certain phonon branches. This proposed static origin challenges the prevailing theory. For a long time, the assumed mechanism for the increase of phonon energy in magnetic compounds through magnetic transition has been the dynamic spin-phonon interaction. This interaction typically arises from spatial modulation of the exchange parameter due to phonon vibrations and is purely dynamic. Notably, existing work primarily offered empirical interpretation and the quantitative evaluations by first principles remain scarce. On the contrary, our atomistic calculations dismiss the dynamic spin-phonon interaction as the cause of the observed phonon energy stiffening in Cr_2O_3. We speculate that the proposed static origin may dominate phonon stiffening in many other systems. Furthermore, our results question the previously suggested change in phonon symmetry, reveal the tunability of selected phonons in Cr_2O_3 through external stimuli, and shed light on controlling lattice dynamics in novel magnetoelectric spintronics.

Overall, this thesis advanced the fundamental understanding of spin-phonon interactions and their implications for spintronic and spin-caloritronic applications. The experimental and theoretical approaches presented in this thesis may provide a valuable toolset for further research on many other systems in this area.

Bibliography

[1] Bin Wei, Qiyang Sun, Chen Li, and Jiawang Hong. Phonon anharmonicity: a pertinent review of recent progress and perspective. *Science China Physics, Mechanics & Astronomy*, 64(11):117001, 2021.

[2] K. Uchida, H. Adachi, T. An, T. Ota, M. Toda, B. Hillebrands, S. Maekawa, and E. Saitoh. Long-range spin seebeck effect and acoustic spin pumping. *Nat Mater*, 10(10):737–41, 2011.

[3] M. Weiler, H. Huebl, F. S. Goerg, F. D. Czeschka, R. Gross, and S. T. Goennenwein. Spin pumping with coherent elastic waves. *Phys Rev Lett*, 108(17):176601, 2012.

[4] A. V. Azovtsev and N. A. Pertsev. Magnetization dynamics and spin pumping induced by standing elastic waves. *Physical Review B*, 94(18), 2016.

[5] H. Hayashi and K. Ando. Spin pumping driven by magnon polarons. *Phys Rev Lett*, 121(23):237202, 2018.

[6] Jorge Puebla, Mingran Xu, Bivas Rana, Kei Yamamoto, Sadamichi Maekawa, and Yoshichika Otani. Acoustic ferromagnetic resonance and spin pumping induced by surface acoustic waves. *Journal of Physics D: Applied Physics*, 53(26), 2020.

[7] X. Zhang, G. E. W. Bauer, and T. Yu. Unidirectional pumping of phonons by magnetization dynamics. *Phys Rev Lett*, 125(7):077203, 2020.

[8] S. M. Rezende, D. S. Maior, O. Alves Santos, and J. Holanda. Theory for phonon pumping by magnonic spin currents. *Physical Review B*, 103(14), 2021.

[9] R. L. Douglass. Heat transport by spin waves in yttrium iron garnet. *Physical Review*, 129(3):1132–1135, 1963.

[10] C. Hess, B. Buchner, U. Ammerahl, L. Colonescu, F. Heidrich-Meisner, W. Brenig, and A. Revcolevschi. Magnon heat transport in doped la2cuo4. *Phys Rev Lett*, 90(19):197002, 2003.

[11] J. P. Feser and D. G. Cahill. Probing anisotropic heat transport using time-domain thermoreflectance with offset laser spots. *Rev Sci Instrum*, 83(10):104901, 2012.

[12] Marc Foëx. A type of transformation common to manganous, ferrous, cobaltous, and nickelous oxides. *Compt. rend*, 227:193–194, 1948.

[13] N. Prasai, B. A. Trump, G. G. Marcus, A. Akopyan, S. X. Huang, T. M. McQueen, and J. L. Cohn. Ballistic magnon heat conduction and possible poiseuille flow in the helimagnetic insulator cu2oseo3. *Physical Review B*, 95(22):224407, 2017.

[14] G. S. Dixon. Lattice thermal conductivity of antiferromagnetic insulators. *Physical Review B*, 21(7):2851–2864, 1980.

[15] G. Laurence and D. Petitgrand. Thermal conductivity and magnon-phonon resonant interaction in antiferromagnetic fecl2. *Physical Review B*, 8(5):2130–2138, 1973.

[16] Yohei Kota, Hiroshi Imamura, and Munetaka Sasaki. Effect of lattice deformation on exchange coupling constants in cr2o3. *Journal of Applied Physics*, 115(17), 2014.

[17] W. Baltensperger. Influence of magnetic order on conduction electrons and phonons in magnetic semiconductors. *Journal of Applied Physics*, 41(3):1052–1054, 1970.

[18] E. Granado, A. García, J. A. Sanjurjo, C. Rettori, I. Torriani, F. Prado, R. D. Sánchez, A. Caneiro, and S. B. Oseroff. Magnetic ordering effects in the raman spectra of $\mathrm{la}_{1-x}\mathrm{mn}_{1-x}\mathrm{o}_3$. *Physical Review B*, 60(17):11879–11882, 1999.

[19] M. G. Cottam and D. J. Lockwood. Spin-phonon interaction in transition-metal difluoride antiferromagnets: Theory and experiment. *Low Temperature Physics*, 45(1):78–91, 2019.

[20] B. S. Araújo, A. M. Arévalo-López, C. C. Santos, J. P. Attfield, C. W. A. Paschoal, and A. P. Ayala. Spin–phonon coupling in monoclinic bicro3. *Journal of Applied Physics*, 127(11), 2020.

[21] P. J. Graham, P. Rovillain, M. Bartkowiak, E. Pomjakushina, K. Conder, M. Kenzelmann, and C. Ulrich. Spin-phonon and magnetoelectric coupling in oxygen-isotope substituted tbmno3 investigated by raman scattering. *Physical Review B*, 105(17), 2022.

[22] K. Park, J. Kim, S. Choi, S. Fan, C. Kim, D. G. Oh, N. Lee, S. W. Cheong, V. Kiryukhin, Y. J. Choi, D. Vanderbilt, J. H. Lee, and J. L. Musfeldt. Spin–phonon interactions and magnetoelectric coupling in co4b2o9 (b = nb, ta). *Applied Physics Letters*, 122(18), 2023.

[23] P. Pal, Shalini Badola, P. K. Biswas, Ranjana R. Das, Surajit Saha, S. D. Kaushik, Parasmani Rajput, P. N. Vishwakarma, and A. K. Singh. Investigation of spin-phonon coupling and local magnetic properties in magnetoelectric fe2teo6. *Journal of Magnetism and Magnetic Materials*, 540, 2021.

[24] E. Aytan, B. Debnath, F. Kargar, Y. Barlas, M. M. Lacerda, J. X. Li, R. K. Lake, J. Shi, and A. A. Balandin. Spin-phonon coupling in antiferromagnetic nickel oxide. *Applied Physics Letters*, 111(25):252402, 2017.

[25] D. J. Lockwood and M. G. Cottam. The spin-phonon interaction in fef2and mnf2studied by raman spectroscopy. *Journal of Applied Physics*, 64(10):5876–5878, 1988.

[26] C. H. Sohn, C. H. Kim, L. J. Sandilands, N. T. Hien, S. Y. Kim, H. J. Park, K. W. Kim, S. J. Moon, J. Yamaura, Z. Hiroi, and T. W. Noh. Strong spin-phonon coupling mediated by single ion anisotropy in the all-in-all-out pyrochlore magnet $\mathrm{cd_2os_2o_7}$. *Phys Rev Lett*, 118(11):117201, 2017.

[27] O. Gomonay, T. Jungwirth, and J. Sinova. High antiferromagnetic domain wall velocity induced by neel spin-orbit torques. *Phys Rev Lett*, 117(1):017202, 2016.

[28] Christian Tzschaschel, Kensuke Otani, Ryugo Iida, Tsutomu Shimura, Hiroaki Ueda, Stefan Günther, Manfred Fiebig, and Takuya Satoh. Ultrafast optical excitation of coherent magnons in antiferromagnetic nio. *Physical Review B*, 95(17):174407, 2017.

[29] M. Fechner, A. Sukhov, L. Chotorlishvili, C. Kenel, J. Berakdar, and N. A. Spaldin. Magnetophononics: Ultrafast spin control through the lattice. *Physical Review Materials*, 2(6):064401, 2018.

[30] Y. W. Windsor, D. Zahn, R. Kamrla, J. Feldl, H. Seiler, C. T. Chiang, M. Ramsteiner, W. Widdra, R. Ernstorfer, and L. Rettig. Exchange-striction driven ultrafast nonthermal lattice dynamics in nio. *Phys Rev Lett*, 126(14):147202, 2021.

[31] T. Jungwirth, X. Marti, P. Wadley, and J. Wunderlich. Antiferromagnetic spintronics. *Nat Nanotechnol*, 11(3):231–41, 2016.

[32] G. E. Bauer, E. Saitoh, and B. J. van Wees. Spin caloritronics. *Nat Mater*, 11(5):391–9, 2012.

[33] Stephen R. Boona, Roberto C. Myers, and Joseph P. Heremans. Spin caloritronics. *Energy & Environmental Science*, 7(3):885, 2014.

[34] Christian Hahn, Grégoire de Loubens, Vladimir V. Naletov, Jamal Ben Youssef, Olivier Klein, and Michel Viret. Conduction of spin currents through insulating antiferromagnetic oxides. *EPL (Europhysics Letters)*, 108(5):57005, 2014.

[35] T. Shang, Q. F. Zhan, H. L. Yang, Z. H. Zuo, Y. L. Xie, L. P. Liu, S. L. Zhang, Y. Zhang, H. H. Li, B. M. Wang, Y. H. Wu, S. Zhang, and Run-Wei Li. Effect of nio inserted layer on spin-hall magnetoresistance in pt/nio/yig heterostructures. *Applied Physics Letters*, 109(3):032410, 2016.

[36] Hailong Wang, Chunhui Du, P. Chris Hammel, and Fengyuan Yang. Spin transport in antiferromagnetic insulators mediated by magnetic correlations. *Physical Review B*, 91(22):220410, 2015.

[37] H. Wang, C. Du, P. C. Hammel, and F. Yang. Antiferromagnonic spin transport from y3fe5o12 into nio. *Phys Rev Lett*, 113(9):097202, 2014.

[38] A. M. Balagurov, I. A. Bobrikov, S. V. Sumnikov, V. Yu Yushankhai, and N. Mironova-Ulmane. Magnetostructural phase transitions in nio and mno: Neutron diffraction data. *JETP Letters*, 104(2):88–93, 2016.

[39] H. Uchiyama, S. Tsutsui, and A. Q. R. Baron. Effects of anisotropic charge on transverse optical phonons in nio: Inelastic x-ray scattering spectroscopy study. *Physical Review B*, 81(24), 2010.

[40] Yi Wang, James E. Saal, Jian-Jun Wang, Arkapol Saengdeejing, Shun-Li Shang, Long-Qing Chen, and Zi-Kui Liu. Broken symmetry, strong correlation, and splitting between longitudinal and transverse optical phonons of mno and nio from first principles. *Physical Review B*, 82(8), 2010.

[41] F. B. Lewis and N. H. Saunders. The thermal conductivity of nio and coo at the neel temperature. *Journal of Physics C: Solid State Physics*, 6(15):2525–2532, 1973.

[42] Larry W. Finger and Robert M. Hazen. Crystal structure and isothermal compression of fe2o3, cr2o3, and v2o3 to 50 kbars. *Journal of Applied Physics*, 51(10):5362–5367, 1980.

[43] V. J. Folen, G. T. Rado, and E. W. Stalder. Anisotropy of the magnetoelectric effect incr2o3. *Physical Review Letters*, 6(11):607–608, 1961.

[44] G. T. Rado and V. J. Folen. Observation of the magnetically induced magnetoelectric effect and evidence for antiferromagnetic domains. *Physical Review Letters*, 7(8):310–311, 1961.

[45] George T. Rado. Statistical theory of magnetoelectric effects in antiferromagnetics. *Physical Review*, 128(6):2546–2556, 1962.

[46] Takeo Izuyama and G. W. Pratt. Theory of the magnetoelectric effect in cr2o3. *Journal of Applied Physics*, 34(4):1226–1228, 1963.

[47] R. Hornreich and S. Shtrikman. Statistical mechanics and origin of the magnetoelectric effect incr2o3. *Physical Review*, 161(2):506–512, 1967.

[48] Manfred Fiebig. Revival of the magnetoelectric effect. *Journal of Physics D: Applied Physics*, 38(8):R123–R152, 2005.

[49] Changjiang Liu, Yongming Luo, Deshun Hong, Steven S.-L. Zhang, Hilal Saglam, Yi Li, Yulin Lin, Brandon Fisher, John E. Pearson, J. Samuel Jiang, Hua Zhou, Jianguo Wen, Axel Hoffmann, and Anand Bhattacharya. Electric field control of magnon spin currents in an antiferromagnetic insulator. *Science Advances*, 7(40):eabg1669, 2021.

[50] Junxue Li, HaakonT Simensen, Derek Reitz, Qiyang Sun, Wei Yuan, Chen Li, Yaroslav Tserkovnyak, Arne Brataas, and Jing Shi. Observation of magnon polarons in a uniaxial antiferromagnetic insulator. *Physical Review Letters*, 125(21):217201, 2020.

[51] Andrew T Boothroyd. *Principles of Neutron Scattering from Condensed Matter*. Oxford University Press, 2020.

[52] Atsushi Togo and Isao Tanaka. First principles phonon calculations in materials science. *Scripta Materialia*, 108:1–5, 2015.

[53] S. Toth and B. Lake. Linear spin wave theory for single-q incommensurate magnetic structures. *J Phys Condens Matter*, 27(16):166002, 2015.

[54] J. Oh, M. D. Le, H. H. Nahm, H. Sim, J. Jeong, T. G. Perring, H. Woo, K. Nakajima, S. Ohira-Kawamura, Z. Yamani, Y. Yoshida, H. Eisaki, S. W. Cheong, A. L. Chernyshev, and J. G. Park. Spontaneous decays of magneto-elastic excitations in non-collinear antiferromagnet (y,lu)mno3. *Nat Commun*, 7:13146, 2016.

[55] Kisoo Park, Joosung Oh, Jonathan C. Leiner, Jaehong Jeong, Kirrily C. Rule, Manh Duc Le, and Je-Geun Park. Magnon-phonon coupling and two-magnon continuum in the two-dimensional triangular antiferromagnetcucro2. *Physical Review B*, 94(10), 2016.

[56] C. Kittel. Interaction of spin waves and ultrasonic waves in ferromagnetic crystals. *Physical Review*, 110(4):836–841, 1958.

[57] T. Kikkawa, K. Shen, B. Flebus, R. A. Duine, K. I. Uchida, Z. Qiu, G. E. Bauer, and E. Saitoh. Magnon polarons in the spin seebeck effect. *Phys Rev Lett*, 117(20):207203, 2016.

[58] Haoran Man, Zhong Shi, Guangyong Xu, Yadong Xu, Xi Chen, Sean Sullivan, Jianshi Zhou, Ke Xia, Jing Shi, and Pengcheng Dai. Direct observation of magnon-phonon coupling in yttrium iron garnet. *Physical Review B*, 96(10), 2017.

[59] F. Godejohann, A. V. Scherbakov, S. M. Kukhtaruk, A. N. Poddubny, D. D. Yaremkevich, M. Wang, A. Nadzeyka, D. R. Yakovlev, A. W. Rushforth, A. V. Akimov, and M. Bayer. Magnon polaron formed by selectively coupled coherent magnon and phonon modes of a surface patterned ferromagnet. *Physical Review B*, 102(14), 2020.

[60] J. Li, H. T. Simensen, D. Reitz, Q. Sun, W. Yuan, C. Li, Y. Tserkovnyak, A. Brataas, and J. Shi. Observation of magnon polarons in a uniaxial antiferromagnetic insulator. *Phys Rev Lett*, 125(21):217201, 2020.

[61] Yi Li, Chenbo Zhao, Wei Zhang, Axel Hoffmann, and Valentyn Novosad. Advances in coherent coupling between magnons and acoustic phonons. *APL Materials*, 9(6), 2021.

[62] J. Holanda, D. S. Maior, A. Azevedo, and S. M. Rezende. Detecting the phonon spin in magnon–phonon conversion experiments. *Nature Physics*, 14(5):500–506, 2018.

[63] P. J. Brown, I. K. Jassim, K. U. Neumann, and K. R. A. Ziebeck. Neutron scattering from invar alloys. *Physica B: Condensed Matter*, 161(1):9–16, 1990.

[64] P. J. Brown, B. Roessli, J. G. Smith, K. U. Neumann, and K. R. A. Ziebeck. Determination of the wavevector and temperature dependence of the ‘forbidden’ mode in invar using inelastic neutron scattering. *Journal of Physics: Condensed Matter*, 8(10):1527–1538, 1996.

[65] P. A. Alekseev, J. M. Mignot, K. S. Nemkovski, A. V. Rybina, V. N. Lazukov, A. S. Ivanov, F. Iga, and T. Takabatake. Interplay of low-energy phonons and magnetic excitations in the kondo insulator ybb12. *J Phys Condens Matter*, 24(20):205601, 2012.

[66] David M. Fobes, Igor A. Zaliznyak, John M. Tranquada, Zhijun Xu, Genda Gu, Xu-Gang He, Wei Ku, Yang Zhao, Masaaki Matsuda, V. Ovidiu Garlea, and Barry Winn. Forbidden phonon: Dynamical signature of bond symmetry breaking in the iron chalcogenides. *Physical Review B*, 94(12), 2016.

[67] O. Arnold, J. C. Bilheux, J. M. Borreguero, A. Buts, S. I. Campbell, L. Chapon, M. Doucet, N. Draper, R. Ferraz Leal, M. A. Gigg, V. E. Lynch, A. Markvardsen, D. J. Mikkelson, R. L. Mikkelson, R. Miller, K. Palmen, P. Parker, G. Passos, T. G. Perring, P. F. Peterson, S. Ren, M. A. Reuter, A. T. Savici, J. W. Taylor, R. J. Taylor, R. Tolchenov, W. Zhou, and J. Zikovsky. Mantid—data analysis and visualization package for neutron scattering and μ sr experiments. *Nuclear Instruments and Methods in Physics Research Section A: Accelerators, Spectrometers, Detectors and Associated Equipment*, 764:156–166, 2014.

[68] D. S. Kim, O. Hellman, J. Herriman, H. L. Smith, J. Y. Y. Lin, N. Shulumba, J. L. Niedziela, C. W. Li, D. L. Abernathy, and B. Fultz. Nuclear quantum effect with pure anharmonicity and the anomalous thermal expansion of silicon. *Proc Natl Acad Sci U S A*, 115(9):1992–1997, 2018.

[69] G. Kresse and J. Furthmüller. Efficient iterative schemes for ab initio total-energy calculations using a plane-wave basis set. *Physical Review B*, 54(16):11169–11186, 1996.

[70] G. Kresse and J. Furthmüller. Efficiency of ab-initio total energy calculations for metals and semiconductors using a plane-wave basis set. *Computational Materials Science*, 6(1):15–50, 1996.

[71] P. E. Blochl. Projector augmented-wave method. *Phys Rev B Condens Matter*, 50(24):17953–17979, 1994.

[72] G. Kresse and D. Joubert. From ultrasoft pseudopotentials to the projector augmented-wave method. *Physical Review B*, 59(3):1758–1775, 1999.

[73] J. P. Perdew and Alex Zunger. Self-interaction correction to density-functional approximations for many-electron systems. *Physical Review B*, 23(10):5048–5079, 1981.

[74] Vi Vi Anisimov, J. Zaanen, and O. K. Andersen. Band theory and mott insulators: Hubbard u instead of stoner i. *Phys Rev B Condens Matter*, 44(3):943–954, 1991.

[75] S. L. Dudarev, G. A. Botton, S. Y. Savrasov, C. J. Humphreys, and A. P. Sutton. Electron-energy-loss spectra and the structural stability of nickel oxide: An lsda+u study. *Physical Review B*, 57(3):1505–1509, 1998.

[76] S. P. Srivastava, R. C. Srivastava, I. D. Singh, S. D. Pandey, and P. L. Gupta. Temperature dependence of thermal expansion and infrared lattice vibrational mode of nickel oxide. *Journal of the Physical Society of Japan*, 43(3):885–890, 1977.

[77] J. Baruchel, M. Schlenker, K. Kurosawa, and S. Saito. Antiferromagnetic s-domains in nio. *Philosophical Magazine B*, 43(5):853–860, 2006.

[78] M. T. Hutchings and E. J. Samuelsen. Measurement of spin-wave dispersion in nio by inelastic neutron scattering and its relation to magnetic properties. *Physical Review B*, 6(9):3447–3461, 1972.

[79] V. Fernandez, C. Vettier, F. de Bergevin, C. Giles, and W. Neubeck. Observation of orbital moment in nio. *Physical Review B*, 57(13):7870–7876, 1998.

[80] L. P. Bouckaert, R. Smoluchowski, and E. Wigner. Theory of brillouin zones and symmetry properties of wave functions in crystals. *Physical Review*, 50(1):58–67, 1936.

[81] A. P. Cracknell and S. J. Joshua. The space group corepresentations of antiferromagnetic nio. *Mathematical Proceedings of the Cambridge Philosophical Society*, 66(2):493–504, 2008.

[82] S. Park and B. J. Yang. Phonon angular momentum hall effect. *Nano Lett*, 20(10):7694–7699, 2020.

[83] Dominik M. Juraschek and Nicola A. Spaldin. Orbital magnetic moments of phonons. *Physical Review Materials*, 3(6), 2019.

[84] M. Hamada, E. Minamitani, M. Hirayama, and S. Murakami. Phonon angular momentum induced by the temperature gradient. *Phys Rev Lett*, 121(17):175301, 2018.

[85] Pablo Maldonado and Yaroslav O. Kvashnin. Microscopic theory of ultrafast out-of-equilibrium magnon-phonon dynamics in insulators. *Physical Review B*, 100(1), 2019.

[86] S. Lipinski, K. U. Neumann, and K. R. A. Ziebeck. The forbidden phonon mode in fe-ni invar. *Journal of Physics: Condensed Matter*, 6(45):9773–9780, 1994.

[87] S. K. Kwon and B. I. Min. Unquenched large orbital magnetic moment in nio. *Physical Review B*, 62(1):73–75, 2000.

[88] X. He, D. Bansal, B. Winn, S. Chi, L. Boatner, and O. Delaire. Anharmonic eigenvectors and acoustic phonon disappearance in quantum paraelectric srtio$_3$. *Phys Rev Lett*, 124(14):145901, 2020.

[89] H. Matthews and R. C. LeCraw. Acoustic wave rotation by magnon-phonon interaction. *Physical Review Letters*, 8(10):397–399, 1962.

[90] A. V. Rybina, P. A. Alekseev, J. M. Mignot, E. V. Nefeodova, K. S. Nemkovski, R. I. Bewley, N. Yu Shitsevalova, Yu B. Paderno, F. Iga, and T. Takabatake. Lattice dynamics and magneto-elastic coupling in kondo-insulator ybb12. *Journal of Physics: Conference Series*, 92, 2007.

[91] W. L. Roth. Neutron and optical studies of domains in nio. *Journal of Applied Physics*, 31(11):2000–2011, 1960.

[92] Glen A. Slack. Crystallography and domain walls in antiferromagnetic nio crystals. *Journal of Applied Physics*, 31(9):1571–1582, 1960.

[93] Song Bao, Zhengwei Cai, Wenda Si, Wei Wang, Xiaomeng Wang, Yanyan Shangguan, Zhen Ma, Zhao-Yang Dong, Ryoichi Kajimoto, Kazuhiko Ikeuchi, Shun-Li Yu, Jian Sun, Jian-Xin Li, and Jinsheng Wen. Evidence for magnon-phonon coupling in the topological magnet cu3teo6. *Physical Review B*, 101(21):214419, 2020.

[94] Christopher A. Pocs, Ian A. Leahy, Hao Zheng, Gang Cao, Eun-Sang Choi, S. H. Do, Kwang-Yong Choi, B. Normand, and Minhyea Lee. Giant thermal magnetoconductivity in crcl3 and a general model for spin-phonon scattering. *Physical Review Research*, 2(1):013059, 2020.

[95] D. R. Ratkovski, L. Balicas, A. Bangura, F. L. A. Machado, and S. M. Rezende. Thermal transport in yttrium iron garnet at very high magnetic fields. *Physical Review B*, 101(17):174442, 2020.

[96] P. A. Sharma, J. S. Ahn, N. Hur, S. Park, S. B. Kim, S. Lee, J. G. Park, S. Guha, and S. W. Cheong. Thermal conductivity of geometrically frustrated, ferroelectric ymno3: extraordinary spin-phonon interactions. *Phys Rev Lett*, 93(17):177202, 2004.

[97] G. A. Slack and R. Newman. Thermal conductivity of mno and nio. *Physical Review Letters*, 1(10):359–360, 1958.

[98] VP Zhuze, NOVRUZOV. ON, and AI Shelykh. Thermal conductivity near a continuous phase transition. *SOVIET PHYSICS SOLID STATE, USSR*, 11(5):1044–+, 1969.

[99] JE Keem and JM Honig. Selected electrical and thermal properties of undoped nickel oxide. *Cindas Report*, 52, 1978.

[100] M. Massot, A. Oleaga, A. Salazar, D. Prabhakaran, M. Martin, P. Berthet, and G. Dhalenne. Critical behavior of coo and nio from specific heat, thermal conductivity, and thermal diffusivity measurements. *Physical Review B*, 77(13), 2008.

[101] Jarno Linnera and Antti J. Karttunen. Lattice dynamical properties of antiferromagnetic mno, coo, and nio, and the lattice thermal conductivity of nio. *Physical Review B*, 100(14):144307, 2019.

[102] M. Kresch, O. Delaire, R. Stevens, J. Y. Y. Lin, and B. Fultz. Neutron scattering measurements of phonons in nickel at elevated temperatures. *Physical Review B*, 75(10), 2007.

[103] David G Cahill. Analysis of heat flow in layered structures for time-domain thermoreflectance. *Review of scientific instruments*, 75(12):5119–5122, 2004.

[104] John P. Perdew, Kieron Burke, and Matthias Ernzerhof. Generalized gradient approximation made simple. *Physical Review Letters*, 77(18):3865–3868, 1996.

[105] C. Thomsen, H. J. Maris, and J. Tauc. Picosecond acoustics as a non-destructive tool for the characterization of very thin films. *Thin Solid Films*, 154(1):217–223, 1987.

[106] D. A. Ditmars, C. A. Plint, and R. C. Shukla. Aluminum. i. measurement of the relative enthalpy from 273 to 929 k and derivation of thermodynamic functions for al(s) from 0 k to its melting point. *International Journal of Thermophysics*, 6(5):499–515, 1985.

[107] Harry Seltz, Bernard J. DeWitt, and Hugh J. McDonald. The heat capacity of nickel oxide from 68-298°k. and the thermodynamic properties of the oxide. *Journal of the American Chemical Society*, 62(1):88–89, 1940.

[108] Atsushi Togo, Laurent Chaput, and Isao Tanaka. Distributions of phonon lifetimes in brillouin zones. *Physical Review B*, 91(9):094306, 2015.

[109] Gyaneshwar P Srivastava. *The physics of phonons*. Routledge, 2019.

[110] W. Reichardt, V. Wagner, and W. Kress. Lattice dynamics of nio. *Journal of Physics C: Solid State Physics*, 8(23):3955–3962, 1975.

[111] Z. Yamani, W. J. L. Buyers, R. A. Cowley, and D. Prabhakaran. Magnetic excitations of spin and orbital moments in cobalt oxidespecial issue on neutron scattering in canada. *Canadian Journal of Physics*, 88(10):729–733, 2010.

[112] Xufei Wu, Zeyu Liu, and Tengfei Luo. Magnon and phonon dispersion, lifetime, and thermal conductivity of iron from spin-lattice dynamics simulations. *Journal of Applied Physics*, 123(8):085109, 2018.

[113] H. J. Qin, K. Zakeri, A. Ernst, and J. Kirschner. Temperature dependence of magnetic excitations: Terahertz magnons above the curie temperature. *Phys Rev Lett*, 118(12):127203, 2017.

[114] M. Grimsditch, L. E. McNeil, and D. J. Lockwood. Unexpected behavior of the antiferromagnetic mode of nio. *Physical Review B*, 58(21):14462–14466, 1998.

[115] Tobias Kampfrath, Alexander Sell, Gregor Klatt, Alexej Pashkin, Sebastian Mährlein, Thomas Dekorsy, Martin Wolf, Manfred Fiebig, Alfred Leitenstorfer, and Rupert Huber. Coherent terahertz control of antiferromagnetic spin waves. *Nature Photonics*, 5(1):31–34, 2010.

[116] Charles Kittel, Paul McEuen, and Paul McEuen. *Introduction to solid state physics*, volume 8. Wiley New York, 1996.

[117] D. G. Cahill and R. O. Pohl. Thermal conductivity of amorphous solids above the plateau. *Phys Rev B Condens Matter*, 35(8):4067–4073, 1987.

[118] John W. Schwartz and Charles T. Walker. Thermal conductivity of some alkali halides containing divalent impurities. ii. precipitate scattering. *Physical Review*, 155(3):969–979, 1967.

[119] Qiyang Sun, Bin Wei, Yaokun Su, Hillary Smith, Jiao Y. Y. Lin, Douglas L. Abernathy, and Chen Li. Mutual spin-phonon driving effects and phonon eigenvector renormalization in nickel (ii) oxide. *Proceedings of the National Academy of Sciences*, 119(29):e2120553119, 2022.

[120] Runqing Yang, Shengying Yue, Yujie Quan, and Bolin Liao. Crystal symmetry based selection rules for anharmonic phonon-phonon scattering from a group theory formalism. *Physical Review B*, 103(18):184302, 2021.

[121] H. Stern. Thermal conductivity at the magnetic transition. *Journal of Physics and Chemistry of Solids*, 26(1):153–161, 1965.

[122] R. Orbach P. V. E. McClintock, I. P. Morton and H. M. Rosenberg. The effect of a magnetic field on the thermal conductivity of paramagnetic crystals: holmium ethylsulphate. *Proceddings of the Royal Society A*, 298(1454):359–378, 1967.

[123] L. Mauger, M. S. Lucas, J. A. Muñoz, S. J. Tracy, M. Kresch, Yuming Xiao, Paul Chow, and B. Fultz. Nonharmonic phonons inα-iron at high temperatures. *Physical Review B*, 90(6), 2014.

[124] D. G. Cahill. Mgo thermal conductivity, 2022.

[125] AA Men, AZ Chechel'nitskij, VA Sokolov, and EN Simun. Thermoconductivity of lithium fluoride in temperature interval 300-1100 0 k. *Fizika Tverdogo Tela*, 15(9):2773–2775, 1973.

[126] AV Petrov, NS Tsypkina, and Yu A Logachev. Temperature dependencies of the thermal conductivity of alkali halide salts at elevated temperatures. *Fizika Tverdogo Tela*, 16(1):65–70, 1974.

[127] BM Mogilevskii, VF Tumpurova, and AF Chudnovskii. Thermal conductivity and structural properties of naf-and yf3-doped caf2 crystals. *Inzh.-Fiz. Zh.*, 27(2):287–295, 1974.

[128] R. F. Caldwell and Miles V. Klein. Experimental and theoretical study of phonon scattering from simple point defects in sodium chloride. *Physical Review*, 158(3):851–875, 1967.

[129] ED Devyatkova and IA Smirnov. The temperature dependence of the thermal resistance of certain crystals near the debye temperature. *SOVIET PHYSICS-SOLID STATE*, 4(9):1836–1841, 1963.

[130] Staffan Andersson and Gunnar Backstrom. Thermal conductivity and heat capacity of single-crystal lif and caf2 under hydrostatic pressure. *Journal of Physics C: Solid State Physics*, 20(35):5951, 1987.

[131] L. C. Bartel and B. Morosin. Exchange striction in nio. *Physical Review B*, 3(3):1039–1043, 1971.

[132] P. G. Klemens. Thermal resistance due to point defects at high temperatures. *Physical Review*, 119(2):507–509, 1960.

[133] E. J. Samuelsen, M. T. Hutchings, and G. Shirane. Inelastic neutron scattering investigation of spin waves and magnetic interactions in cr2o3. *Physica*, 48(1):13–42, 1970.

[134] LF Mollenauer and AL Schawlow. Piezospectroscopic studies of exchange-coupled cr 3+ ion pairs in ruby. *Physical Review*, 168(2):309, 1968.

[135] Siqi Shi, A. L. Wysocki, and K. D. Belashchenko. Magnetism of chromia from first-principles calculations. *Physical Review B*, 79(10), 2009.

[136] Fatemeh Heydarinasab, Morteza Jazandari, Md Mobarak Hossain Polash, Jahanfar Abouie, and Daryoosh Vashaee. Paramagnon heat capacity and anomalous thermopower in anisotropic magnetic systems: Understanding interlayer spin correlations in a magnetically disordered phase. *Physical Review B*, 109(5), 2024.

[137] Y. Zheng, T. Lu, Md M. H. Polash, M. Rasoulianboroujeni, N. Liu, M. E. Manley, Y. Deng, P. J. Sun, X. L. Chen, R. P. Hermann, D. Vashaee, J. P. Heremans, and H. Zhao. Paramagnon drag in high thermoelectric figure of merit li-doped mnte. *Science Advances*, 5(9):eaat9461, 2019.

[138] Adrian H. Hill, Andrew Harrison, Calum Dickinson, Wuzong Zhou, and Winfried Kockelmann. Crystallographic and magnetic studies of mesoporous eskolaite. *Microporous and Mesoporous Materials*, 130(1-3):280–286, 2010.

[139] R. Zimmermann, P. Steiner, and S. Hüfner. *Electron spectroscopies and partial excitation spectra in Cr2O3*, pages 49–52. Elsevier, Amsterdam, 1996.

[140] Robert M White, Robert M White, and Bradford Bayne. *Quantum theory of magnetism*, volume 1. Springer, 1983.

[141] Sergio M Rezende. *Fundamentals of magnonics*, volume 969. Springer, 2020.

[142] D. S. Maior, E. C. Souza, and S. M. Rezende. Magnon energy renormalization in yttrium iron garnet. *Physical Review B*, 108(5), 2023.

[143] Sergio M. Rezende, Antonio Azevedo, and Roberto L. Rodríguez-Suárez. Introduction to antiferromagnetic magnons. *Journal of Applied Physics*, 126(15), 2019.

[144] H. Shaked and S. Shtrikman. Susceptibility derived sublattice magnetization in cr2o3. *Solid State Communications*, 6(6):425–426, 1968.

[145] J. Iniguez. First-principles approach to lattice-mediated magnetoelectric effects. *Phys Rev Lett*, 101(11):117201, 2008.

[146] Masato Hamada and Shuichi Murakami. Phonon rotoelectric effect. *Physical Review B*, 101(14), 2020.

[147] Anna M. Dymshits, Peter I. Dorogokupets, Igor S. Sharygin, Konstantin D. Litasov, Anton Shatskiy, Sergey V. Rashchenko, Eiji Ohtani, Akio Suzuki, and Yuji Higo. Thermoelastic properties of chromium oxide cr2o3 (eskolaite) at high pressures and temperatures. *Physics and Chemistry of Minerals*, 43(6):447–458, 2016.

[148] Vivek Dwij, Gaurav Sharma, Shekhar Tyagi, Binoy Krishna De, and V. G. Sathe. Phonon anomalies in magnetoelectric cr2o3, 2019.

[149] Koichi Momma and Fujio Izumi. Vesta 3 for three-dimensional visualization of crystal, volumetric and morphology data. *Journal of applied crystallography*, 44(6):1272–1276, 2011.

[150] T. Larbi, B. Ouni, A. Gantassi, K. Doll, M. Amlouk, and T. Manoubi. Structural, optical and vibrational properties of cr2o3 with ferromagnetic and antiferromagnetic order: A combined experimental and density functional theory study. *Journal of Magnetism and Magnetic Materials*, 444:16–22, 2017.

[151] F. Körmann, A. Dick, B. Grabowski, T. Hickel, and J. Neugebauer. Atomic forces at finite magnetic temperatures: Phonons in paramagnetic iron. *Physical Review B*, 85(12), 2012.

[152] Chao-Sheng Lian, Jian-Tao Wang, and Changfeng Chen. Ab initiostudy of the anharmonic lattice dynamics of iron at the $\gamma - \delta$ phase transition. *Physical Review B*, 92(18), 2015.

[153] Tomonori Tanaka and Yoshihiro Gohda. Prediction of the curie temperature considering the dependence of the phonon free energy on magnetic states. *npj Computational Materials*, 6(1), 2020.

[154] N. P. Duong, T. Satoh, and M. Fiebig. Ultrafast manipulation of antiferromagnetism of nio. *Phys Rev Lett*, 93(11):117402, 2004.

[155] R. Jin, Y. Onose, Y. Tokura, D. Mandrus, P. Dai, and B. C. Sales. In-plane thermal conductivity of nd2cuo4: evidence for magnon heat transport. *Phys Rev Lett*, 91(14):146601, 2003.

[156] Hisamoto Kondoh, Enji Uchida, Yoshihide Nakazumi, and Takeo Nagamiya. Magnetic anisotropy measurements of nio single crystal. *Journal of the Physical Society of Japan*, 13(6):579–586, 1958.

[157] Florian Meier, Jeremy Levy, and Daniel Loss. Quantum computing with antiferromagnetic spin clusters. *Physical Review B*, 68(13):134417, 2003.

[158] B. Y. Pan, T. Y. Guan, X. C. Hong, S. Y. Zhou, X. Qiu, H. Zhang, and S. Y. Li. Specific heat and thermal conductivity of ferromagnetic magnons in yttrium iron garnet. *EPL (Europhysics Letters)*, 103(3):37005, 2013.

[159] J. R. Tomlinson, L. Domash, R. G. Hay, and C. W. Montgomery. The high temperature heat content of nickel oxide. *Journal of the American Chemical Society*, 77(4):909–910, 1955.